Durham E-Theses

Gravitational lensing and galaxy clusters

Wilson, Gillian

How to cite:

Wilson, Gillian (1995) *Gravitational lensing and galaxy clusters*, Durham theses, Durham University. Available at Durham E-Theses Online: http://etheses.dur.ac.uk/5310/

Gravitational Lensing
and
Galaxy Clusters

by
Gillian Wilson

A Thesis
Submitted to the University of Durham
for the Degree of
Doctor of Philosophy.

September 1995

Abstract

Kaiser & Squires have proposed a technique for mapping the dark matter in galaxy clusters using the coherent weak distortion of background galaxy images caused by gravitational lensing. We investigate the effectiveness of this technique under controlled conditions by creating simulated CCD frames containing galaxies lensed by a model cluster, measuring the resulting galaxy shapes, and comparing the reconstructed mass distribution with the original. Typically, the reconstructed surface density is diminished in magnitude when compared to the original. The main cause of this reduced signal is the blurring of galaxy images by atmospheric seeing, but the overall factor by which the reconstructed surface density is reduced depends also on the signal-to-noise ratio in the CCD frame and on both the sizes of galaxy images and the magnitude limit of the sample that is analysed. We propose a method for estimating a multiplicative compensation factor, f, directly from a CCD frame which can then be used to correct the surface density estimates given by the Kaiser & Squires formalism. We test our technique using a lensing cluster drawn from a cosmological N-body simulation with a variety of realistic background galaxy populations and observing conditions. We conclude that weak lensing observations when calibrated using this method yield not only accurate maps of the cluster morphology but also quantitative estimates of the cluster mass distribution.

We then show that weak lensing simulations by rich clusters can be used to constrain the likely range of values of the cosmological constant Ω_0. Again employing the Kaiser & Squires mass density estimator, we model the lensing induced by a number of simulated clusters from three different cosmologies. We introduce new statistics which are independent of any uncertainties in the surface density mentioned above. We conclude that lensing observations of a small number of clusters should be sufficient to place broad constraints on Ω_0 and certainly distinguish between the extreme values of 0.2 and 1.

We also present deep two-colour photometry of two rich clusters at $z = 0.18$; A1689 and A665. We use the data to construct number counts as a function of magnitude. To the magnitude depth we were able to probe, we conclude that there is no strong evidence for a steep faint end slope to the galaxy luminosity function in moderate-redshift clusters.

Preface

The work presented in this thesis was carried out between 1991 and 1995 while the author was a research student under the supervision of Prof. C.S. Frenk, in the Department of Physics at the University of Durham.

Some of the work here was undertaken in collaboration with the following research staff: Prof. C.S. Frenk (Chapters 2, 3 & 4); Dr S. Cole (Chapters 2 & 3) and Dr. I. Smail (Chapter 4). However, the major part of the research presented here is the author's own work. This work has not been submitted for any degree, diploma or other qualification at any other university.

Certain results have appeared in the following papers:

Wilson, G., Cole S. & Frenk, C.S., in Proc. 5th Annual Maryland conference, Dark Matter in the Universe, 1994, eds S.S. Holt and C.L. Bennett, AIP Press, p351

Wilson, G., Cole S. & Frenk, C.S., M.N.R.A.S., 1995, accepted

Acknowledgements

Firstly, I would like to thank my supervisor, Professor Carlos Frenk for giving me the opportunity to fulfil a longtime ambition to study cosmology. In the time that I have known him his enthusiasm for his subject has always been intense and very infectious. I would also like to thank my mentors, Doctors Shaun Cole and Ian Smail for their help with the theoretical and observational aspects of this thesis respectively. They were both very clear-sighted with their suggestions and patient with my questions.

Durham was an excellent department in which to do my Ph.D. Not only was it very stimulating intellectually, but it was also very pleasant socially. Thank you to all my friends at Durham for making my time here so enjoyable.

My final and biggest thank you, however, must be reserved for my Mother and my Father, for all their support, both emotional and financial.

To my Father,
who inspired me to become
a scientist

FIRE AND ICE

Some say the world will end in fire
Some in ice.
From what I've tasted of desire,
I hold with those who favour fire.
But if it were to perish twice,
I think I know enough of hate
To say that for destruction ice
Is also great
And would suffice.

Robert Frost

Contents

Chapter 1

Introduction

In the standard picture of hierarchical structure formation, clusters are the most recently formed bound structures and, of all objects in the Universe, they are expected to retain most traces of the initial conditions which determined their formation. It has become apparent in recent years that the dynamical state of clusters can be probed effectively by analysing the distortions in the images of background galaxies gravitationally lensed by the cluster potential. When suitably analysed, these distortions provide a direct measure of the cluster mass as well as a map of the distribution of dark matter within the cluster.

Traditionally, estimates of cluster masses have been based either on the virial theorem, or on the properties of the hot X-ray emitting intracluster gas or on a combination of both e.g. Hughes (1989). In all cases, a number of assumptions are required which introduce unavoidable uncertainties.

For example, the virial theorem states that, for a system whose properties are constant with time,

$$2T + V = 0, \tag{1.1}$$

where T is the total kinetic energy of the system and V, the potential energy. Thus

$$M <v^2> -\frac{\alpha G M^2}{r} = 0 \tag{1.2}$$

$$\Rightarrow M = \frac{r <v^2>}{\alpha G} \tag{1.3}$$

where v is the velocity of each galaxy, M the total mass out to some radius r, and the value of α depends on the mass distribution of the cluster but is usually ≈ 1. Therefore, in principle, it is possible to measure a cluster mass from its galaxies' velocity dispersions. However, only the radial component of the velocity of cluster galaxies is measurable, so assumptions need to be made concerning the missing

information about the galaxies' orbits in three dimensions. In addition, all optical observations are confused by chance alignments of field or group galaxies physically unrelated to the cluster (Frenk et al. 1990).

X-ray observations are less influenced by projection effects. The radiation is due to bremsstrahlung mainly from H and He ions in the intra-cluster gas, and is proportional to the square of the gas density e.g. Fabian (1988). The shape of the spectrum is very sensitive to temperature for energies greater than kT, but rather insensitive below. X-ray analyses of the hot gas usually assume that it is in hydrostatic equilibrium with a spherically-symmetric potential,

$$\frac{dP_{gas}}{dr} = -\rho_{gas}\frac{d\Phi}{dr} \tag{1.4}$$

It then follows that the total mass contained within radius r, is

$$M(r) = -\frac{krT}{G\mu m_p}\left[\frac{d(ln\rho_{gas})}{d(lnr)} + \frac{d(lnT)}{d(lnr)}\right] \tag{1.5}$$

As can be seen from the formula, the inferred mass depends on the temperature profile of the gas and this is still poorly constrained by existing X-ray data e.g. Arnaud (1994). To facilitate the calculation, it is usually assumed that the gas is isothermal and follows a King profile. All these assumptions introduce uncertainties into the calculation of total mass in the cluster. Furthermore, since gas density falls off rapidly with distance from the centre, other techniques are required to measure mass at large distances from the cluster centre.

The use of clusters as cosmological tools is not restricted to the information provided by their total mass. If small systems of galaxies have recently merged to produce a rich cluster, evidence of vestigial substructure should be apparent. The distribution of mass within clusters is therefore as important a diagnostic of the cluster formation process as is their total mass. For example, Evrard et al. (1994) and Mohr et al. (1995) have used simulations of cluster gas and dark matter to suggest that an X-ray morphology-cosmology relationship exists. They find that clusters formed in low Ω_0 models are more regular and spherically symmetric than clusters formed in the $\Omega_0 = 1$ case. This is a reflection of the fact that clusters form earlier in low Ω_0 universes (Lacey & Cole 1993).

Uniquely amongst all techniques for studying galaxy clusters, gravitational lensing is *directly* sensitive to the dark matter within the cluster. Thus, lensing studies bypass the uncertain connection between the luminous material in clusters and the dynamically dominant dark matter component. In principle, gravitational lensing provides the most powerful tool available to extract cosmological information from clusters.

The first detections of gravitational lensing by clusters were made in the late 1980s. Lynds & Petrosian (1986) reported the discovery of giant arcs in the clusters

A370, A2218 and Cl2244-02 and, independently, Soucail et al. (1987) discovered arcs in A370. Giant arcs are spectacular but rare occurrences. Their existence depends upon the serendipitous alignment along the line-of-sight of a background galaxy with a dense cluster core. Perfect alignment behind a spherically symmetric core region would lead to a perfectly circular image – a so-called Einstein ring. In practice only portions of the ring are produced, causing the images to be called arcs. A comprehensive review of giant arcs and their properties may be found in Fort & Mellier (1994).

It is far more common for a galaxy lying behind and to the side of a cluster to be stretched or sheared tangentially only slightly. Galaxies which have undergone only weak distortion are generally referred to as arclets. These galaxies are too faint for spectroscopy so individually they are impractical as indicators of lensing. However, the cluster mass distribution can be recovered statistically by analysing collectively these weakly, but coherently lensed arclets. Tyson et al. (1990) were the first to study weakly lensed images in the clusters A1689 and Cl1409+52. In their pioneering study, they observed an excess of tangentially aligned galaxies and set constraints on the cluster potential from this data. Subsequently, a number of authors (e.g. Kochanek 1990; Miralda-Escude 1991) have attempted to determine cluster parameters, such as velocity dispersion and core radii, from observations of weakly lensed galaxies by model fitting. They assume *a priori* some form for the distribution of mass in the lens and then determine the most likely values of the model parameters.

Kaiser & Squires (1993), hereafter KS, proposed an elegant, model-independent mass reconstruction method. This technique, described in detail in Section 2.2, produces a "map" of the surface density at each point in the cluster. Since the initial idea was proposed, progress on the theoretical front has been extremely rapid. Seitz & Schneider (1995a) and Kaiser (1995) have developed extensions of the method capable of simultaneously reconstructing the cluster mass in the weak and strong lensing regimes. The KS technique assumes that lensing information is available over an infinite field of view. In practice, the limited size of CCD frames introduces spurious boundary effects. Schneider (1995), Kaiser et al. (1994a) and Seitz & Schneider (1995b) have all addressed this problem. Some attempts have been made to investigate the KS method using clusters grown in N-body simulations as lenses. Bartelmann (1995) used a sample of 60 clusters from the simulations of Bartelmann & Weiss (1994), synthetically lensed them, and investigated a variety of reconstruction algorithms based on the KS method.

It has long been realised that the original KS technique does not furnish the *absolute* value of the mass surface density because a uniform screen of mass located between the observer and the background galaxies produces no gravitational distortion. Bartelmann & Narayan (1995) and Broadhurst et al. (1995) have suggested methods to break this degeneracy by utilising the magnification of the lensed background field galaxies rather than the distortion of their images to try to constrain the absolute value of surface density. Whether these theoretical ideas can be applied effectively in practice still remains to be seen.

With the widespread availability of large CCDs, observational studies of weak lensing have proliferated in the past couple of years. Bonnet et al. (1994) detected a lensing signal in Cl0024+1654; Fahlman et al. (1994), Kaiser et al. (1994a), Kaiser et al. (1994b), Squires et al. (1996) in ms1224+007, A2218 and A1689; Smail et al. (1994) in Cl1455+22 and Cl0016+16; and Tyson & Fischer (1995) again in A1689. These detections have generated a great deal of interest in lensing studies as well as some controversy. For example, the dark matter mass inferred for ms1224+007 from lensing data by Fahlman et al. (1994) is three times larger than the virial mass inferred from optical data. (See also Carlberg et al. 1994) . A2163 is another paradox: it is the most X-ray luminous cluster known but no lensing signal has been detected (Squires 1994).

It is clear that weak gravitational lensing is a powerful and useful technique but that there is still much work to be done in order to understand the problems and systematic effects implicit in its use. The values of the cluster mass surface density inferred from distorted images of background galaxies are complicated by the influence of inherent observational effects such as noise, seeing, crowding and pixelation (i.e. the discrete sampling of the average intensity in the detector pixels). The quality of the signal depends additionally on intrinsic properties of the lensed galaxies – their magnitudes, sizes, ellipticities and redshifts. The relative importance of all these factors is investigated in Chapter 2.

In Chapter 3 we pursue the idea that the morphology of clusters is determined by the cosmological parameters Ω_0 and λ_0 and that, given a sample of clusters, we can discriminate amongst cosmological scenarios. We extend upon the cluster simulation and X-ray work mentioned previously (Evrard et al. 1994; Mohr et al. 1995). Using their eight clusters from each of three cosmologies we simulate observations of gravitational lensing and analyse them as in Chapter 2. We develop new statistics for analysing the shapes of the clusters. Using these statistics we find, analogously to Evrard et al. and Mohr et al., that the morphologies are distinguishable.

In Chapter 4 we present some deep two-colour photometry of the two rich clusters A1689 and A665. Initially we had hoped to study weak gravitational lensing using these clusters but the seeing proved too poor. Instead we use the data to construct number counts as a function of magnitude. To the magnitude depth we were able to probe, we conclude that there is no strong evidence for a steep faint end slope to the galaxy luminosity function in our moderate-redshift clusters.

Chapter 2

Weak Lensing

2.1 Introduction

Our aim in this chapter is to confirm that the Kaiser & Squires (1993) technique does indeed recover accurately a complex lensing mass distribution under controlled conditions. We do this by simulating CCD frames of artificially lensed galaxies and analysing these frames with the same techniques of faint galaxy data reduction that are commonly applied to real data. We construct a variety of artificial clusters to investigate the relative importance of observational effects by varying them individually. Since the mass distribution of the artificial clusters is, of course, known, the accuracy of the mass reconstruction obtained under differing observing conditions can be assessed. In general, we find that the recovered mass surface density is less than the true surface density by some factor. It is impossible to tabulate a compensation factor for all possible combinations of variables but by means of an example we illustrate a *method* for estimating this factor for any given data set. Our intention is not to model conditions with any one particular telescope or observational set-up in mind, but rather to produce results which can be applied generally.

In Section 2.2 we summarise the lensing concepts and equations which we will require. In Section 2.3 we describe some preliminary simulations for testing the KS method under the simplest possible conditions and without generating CCD frames. We create simple spherically symmetric lenses of varying mass and calculate the lensing they produce, using a formula derived in Appendix A. This ensures that the KS technique has been thoroughly tested before we introduce all the complications due to seeing, noise and mis-measurement that accompany real-life data. We then proceed to simulate CCD frames, describing the details of the source galaxies, cluster lens and analysis software which we use in Section 2.4. In Section 2.5 we again generate and utilise simple spherically symmetric lenses of varying mass in order to illustrate the effect on the reconstructed surface density of atmospheric seeing and of non-linear terms ignored in the KS method. We then proceed to show how the reduction in the lensing signal caused by atmospheric seeing can be compensated for by performing a calibration exercise in which a known shear is applied to a CCD

image. Here we use a cluster drawn from a cosmological N-body simulation as a lens and perform the complete analysis using realistic distributions of ellipticity, size and redshift for the background galaxies. In Section 2.6 we repeat the analysis varying each of these distributions, demonstrating the versatility and accuracy of our calibration technique and the general power of the KS reconstruction method. We conclude in Section 2.7 with a summary of our main results.

2.2 Weak Lensing

2.2.1 Basic Concepts of Lensing

The basic lensing geometry is shown in Figure 2.1. The primed letters are points in the source plane. Their unprimed counterparts are corresponding points in the image plane. Light from the source galaxy S' follows the path $S'IO$ to the observer. The galaxy's apparent position in the source plane is I'. As can be seen from the figure, for a circularly symmetric potential, galaxies are displaced radially outward from the centre of the cluster i.e. from S' to I'. Implicit in this scheme is the assumption that all deflection takes place at one point (the lens) in a light ray's journey to the observer. We use the subscript s to refer to the true, unlensed position of the source and the subscript i to refer to the apparent position of the image. The letter D denotes angular diameter distances. Its subscripts denote observer, lens and source galaxy. $\vec{\alpha}$ is the angle through which light rays are deflected at the lens and $\vec{\beta}$ is the apparent angle of deflection at the observer's position.

In the small angle approximation these angles are related by

$$D_{ls}\vec{\alpha} = \vec{S'I'} = D_{os}\vec{\beta} \tag{2.1}$$

Hence, the lens equation, relating the true position of a source galaxy θ_s to its apparent position θ_i by means of the bending angle β, is given by

$$\vec{\theta_i} - \vec{\theta_s} = \vec{\beta}(\vec{\theta_i}) = \frac{D_{ls}}{D_{os}}\vec{\alpha} \tag{2.2}$$

The angle, $\vec{\alpha}$, through which rays are deflected can be calculated from the gradient of the lens' projected gravitational potential (see e.g. Schneider et al. 1992, Chapter 5). Thus, if we define a dimensionless 2-D potential by

$$\Phi_{2D}(\vec{\theta_i}) = \frac{2}{c^2}\frac{D_{ls}}{D_{os}D_{ol}}\int \Phi_{3D}(\vec{\theta_i}, z)\, dz \tag{2.3}$$

then

$$\vec{\beta}(\vec{\theta_i}) = \nabla\Phi_{2D} \tag{2.4}$$

where $\nabla \equiv (\frac{\partial}{\partial\theta_x}, \frac{\partial}{\partial\theta_y})$ is the gradient operator in angular coordinates on the sky. Just as the three-dimensional potential is related to the density via Poisson's equation, so the two-dimensional potential is related to the projected surface density, S,
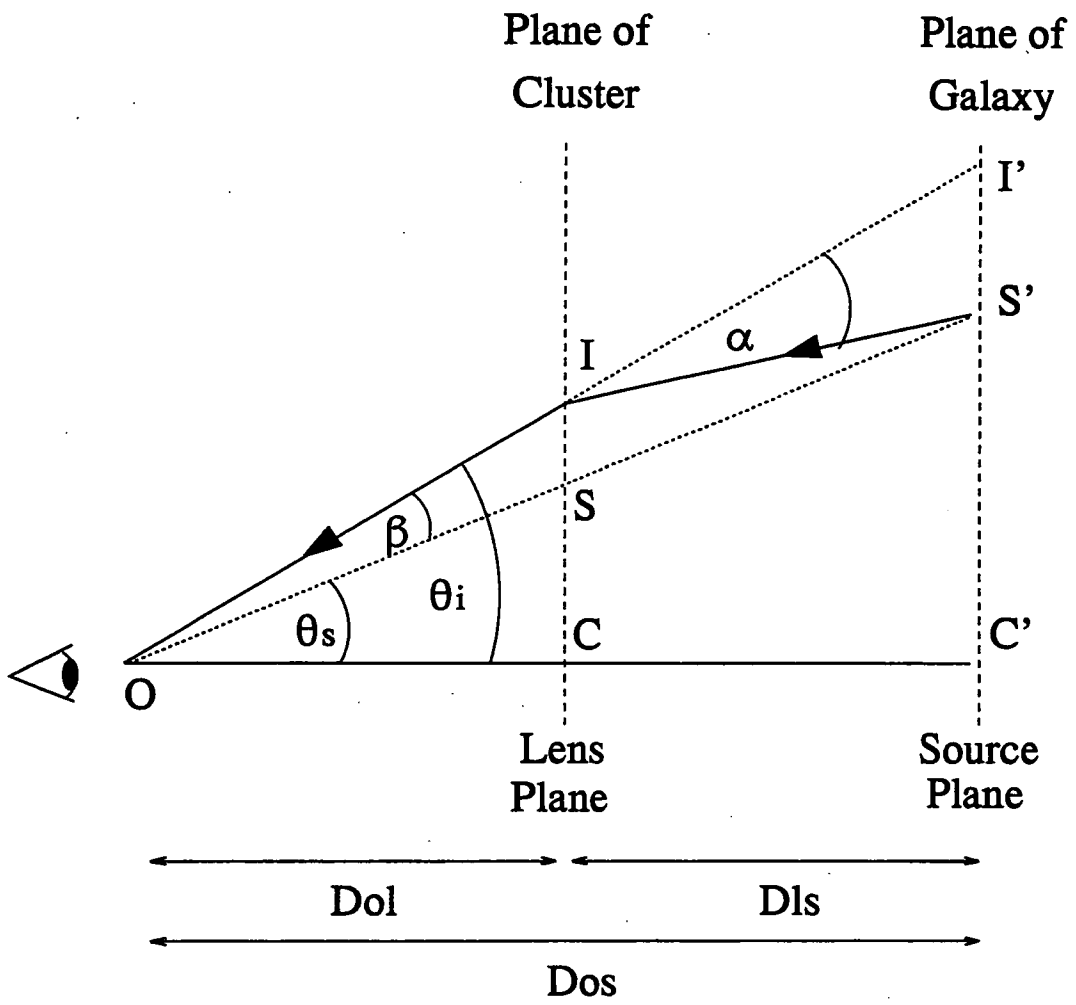
Figure 2.1: Schematic lensing diagram

via the two-dimensional Poisson equation:

$$\nabla^2 \Phi_{2D} = \frac{2S}{S_{\text{crit}}} \tag{2.5}$$

where S_{crit}, the critical surface density, is defined as

$$S_{\text{crit}} = \frac{c^2}{4\pi G} \frac{D_{\text{os}}}{D_{\text{ol}} D_{\text{ls}}} \tag{2.6}$$

This critical surface density is that required to form multiple images of a source object. It is also the mean surface density within the Einstein ring.

2.2.2 The KS Inversion Technique

A point mass produces a distinctive distortion signal. Surrounding galaxies are elongated in the direction of tangents to concentric circles centred on the point. For a complex lens, if one chooses a point $\vec{\theta}$ in the lens plane, then the correlation of the actual pattern of galaxy orientations with the tangential pattern which would be produced by a point mass at $\vec{\theta}$ is a measure of the surface density of the lens at that point. Remarkably, as shown by Kaiser & Squires (1993), in the weak lensing regime, where $S \ll S_{\text{crit}}$, the lens surface density is simply proportional to this degree of correlation. Define

$$\hat{\sigma}(\vec{\theta}) = \frac{\hat{S} - \bar{S}}{S_{\text{crit}}} \tag{2.7}$$

where $\hat{\sigma}(\vec{\theta})$ is the estimated deviation of the lens surface density at position $\vec{\theta}$ from the mean surface density $\bar{S}$ within the area being considered ("overdensity" or "underdensity"), measured in units of the critical surface density S_{crit}. Kaiser & Squires (1993) were able to express the lens surface overdensity, $\hat{\sigma}$, at any position $\vec{\theta}$ in terms of a direct sum over the galaxies. They showed that

$$\hat{\sigma}(\vec{\theta}) = -\frac{1}{\bar{n}} \sum_g W(\vec{\theta_g} - \vec{\theta}) \, \chi_i(\vec{\theta_g} - \vec{\theta}) \, e_i(\vec{\theta_g}) \tag{2.8}$$

The sum in equation (2.8) is performed over all the galaxies in the image, where θ_g is the position of each galaxy. $\bar{n}$ is the mean number density of galaxies per unit area. The three remaining factors on the right hand side of equation (2.8) are the ellipticities of the galaxies, e_i, the kernel, χ_i, which is the distortion pattern produced by a point mass, and a weighting function, $W(\vec{\theta})$, which produces a smoothed estimate of the lens surface overdensity. Both the ellipticities, e_i, and kernel, χ_i are two component quantities and summation over i is implicit. We now define these quantities more precisely.

The components, e_i, of the galaxy ellipticity are the following combinations of the intensity-weighted second moments of the image:

$$e_1 = \frac{I_{\text{xx}} - I_{\text{yy}}}{I_{\text{xx}} + I_{\text{yy}}} \tag{2.9}$$

8

and

$$e_2 = \frac{2I_{xy}}{I_{xx} + I_{yy}} \qquad (2.10)$$

For example, the intensity moment I_{xy} is

$$I_{xy} = \frac{\int F(\vec{\theta})(\theta_x - \theta_x^c)(\theta_y - \theta_y^c)d^2\underline{\theta}}{\int F(\vec{\theta})d^2\underline{\theta}} \qquad (2.11)$$

where $F(\vec{\theta})$ is the intensity at $\vec{\theta}$ and $\vec{\theta}^c$ is the centroid of the galaxy image. For a galaxy whose isophotes are concentric aligned ellipses with axial ratio b/a, the size of the ellipticity, $e = \sqrt{e_1^2 + e_2^2}$, is simply $e = (1 - (b/a)^2)/(1 + (b/a)^2)$. The components e_1 and e_2 are given by $e_1 = e\cos(2\phi)$ and $e_2 = e\sin(2\phi)$, where ϕ is the angle between the x-axis and the major axis of the ellipse. Note that for circular galaxies $(b/a = 1)$ $e = 0$, while for highly elliptical galaxies $(b/a \ll 1)$ $e \rightarrow 1$.

The components of the kernel $\chi_i(\vec{\theta_g} - \vec{\theta})$, are given by the expressions

$$\chi_1(\vec{\theta_g} - \vec{\theta}) = \frac{(\theta_{gx} - \theta_x)^2 - (\theta_{gy} - \theta_y)^2}{|\vec{\theta_g} - \vec{\theta}|^2} \qquad (2.12)$$

and

$$\chi_2(\vec{\theta_g} - \vec{\theta}) = \frac{2(\theta_{gx} - \theta_x)(\theta_{gy} - \theta_y)}{|\vec{\theta_g} - \vec{\theta}|^2} \qquad (2.13)$$

Note that both the ellipticities, e_i, and the kernel, χ_i, are polars, i.e. a rotation of the coordinate system through 180 degrees leaves their components unchanged. This is perhaps most easily understood by visualizing each galaxy as an ellipse which has 180 degree symmetry.

The weighting function, $W(\vec{\theta})$, is introduced to produce a smoothed estimate of the lens mass distribution. If no smoothing is assumed then the variance in the KS estimator is formally infinite. The smoothing function is required to be a low-pass filter but is otherwise arbitrary. The choice of window function will, in general, depend on the specific property of the lens mass distribution one is interested in. Here we wish to make maps of the mass distribution and so we have adopted a simple Gaussian window function with Fourier transform

$$T(\vec{k}) = \exp\frac{-k^2\theta_{sm}^2}{2} \qquad (2.14)$$

The smaller the smoothing angle, θ_{sm}, the larger the typical error in $\hat{\sigma}$ due to the intrinsic ellipticities of the background galaxies. For this choice of smoothing window, Kaiser & Squires compute the variance in the estimator, $\hat{\sigma}$,

$$\langle(\hat{\sigma} - \langle\hat{\sigma}\rangle)^2\rangle = \frac{e^2}{8\pi\bar{n}\theta_{sm}^2} \qquad (2.15)$$

9

where e is the mean value of the intrinsic ellipticities of the galaxies used in the reconstruction. The uncertainty in $\hat{\sigma}$ is proportional to the *rms* galaxy ellipticity and inversely proportional to the smoothing angle and the root number of galaxies per unit area. In practice, however, uncertainties also arise due to errors in measurement, pixelation, noise etc.

We have chosen the smoothing angle θ_{sm} to be 0.25 arcminutes as a compromise between producing a high resolution but noisy map and a featureless low resolution map. The weighting function is then related to the transform of this window function by

$$W(\vec{\theta_g} - \vec{\theta}) = \frac{1}{(2\pi)^2} \int T(\vec{k}) \, J_2(\vec{k}.\vec{\theta}) \, d^2\vec{k} \qquad (2.16)$$

where J_2 denotes the second order Bessel function.

Finally, it is worth remembering that the quantity σ estimated by equation (2.8) is the surface overdensity in units of the critical surface density as defined by equation (2.6). Since S_{crit} depends on the geometry of the lensing configuration through the angular diameter–distance relationship, the mean redshift distribution of source galaxies is required before the *absolute* surface density can be obtained. In addition, the KS technique is sensitive only to variations in surface density. This is because a uniform slab of material across the whole lens plane does not distort the images of galaxies lying behind. Thus, the mean surface density, $\bar{S}$, is also unknown unless the region analysed is sufficiently large that it encompasses the whole of the lensing cluster so that the surface density near the edge of the region can be taken as the zero-point.

2.3 Preliminary Simulations

In this section we test the KS technique under the simplest possible conditions. We use a spherically symmetric lens with a Gaussian mass distribution. Instead of creating a CCD image and analysing the galaxy shapes from it, with all the complications due to seeing, noise and mis-measurement, we calculate the shapes of the lensed galaxies analytically.

2.3.1 The Method

As discussed in Appendix A, the expression for the intensity-weighted second moments of the lensed galaxies is

$$\begin{pmatrix} I_{xx} & I_{xy} \\ I_{yx} & I_{yy} \end{pmatrix} \propto \begin{pmatrix} 1 + 2\frac{\partial \beta_x}{\partial \theta_{ix}} & 2\frac{\partial \beta_x}{\partial \theta_{iy}} \\ 2\frac{\partial \beta_y}{\partial \theta_{ix}} & 1 + 2\frac{\partial \beta_y}{\partial \theta_{iy}} \end{pmatrix} \qquad (2.17)$$

10

where the symbols have the meanings defined in Section 2.2.1.

For simplicity we place all our unlensed, source galaxies at one redshift, in this case $z = 0.5$. Their x-y coordinates are assigned randomly. We generate 5000 such galaxies which corresponds to a surface density of ~ 50 arcminute^{-2}. We then calculate the moments from equation (2.17) and substitute in equations (2.9) and (2.10) to find their new lensed shapes e_1 and e_2. Finally, we use e_1 and e_2 in the KS reconstruction formula (2.8) to obtain the surface overdensity.

Note that for each galaxy we have to calculate the change in bending angle with respect to a small change in position about the centre of the galaxy. There is one complication, which is that we know each galaxy's source position θ_s but not its image position θ_i. However, we require to calculate the change in bending angle at the image position, $\frac{\partial \beta_x}{\partial \theta_{ix}}$ etc. Using the source position as a first approximation to the image position, and knowing the bending angle at each point we solve for θ_i iteratively using equation (2.2).

Our reconstructions matched very closely the shape of the mass distributions for low values of peak surface density but they failed to return true values of surface density near the peak of the Gaussian for higher surface densities. This effect is illustrated in Figures 2.2 and 2.3 which show the mean of five simulations in each case, with maximum surface overdensity values $\hat{\sigma}$ of $\simeq 0.02$ and $\simeq 0.2$ respectively.

These examples illustrate the breakdown of the KS technique as we leave the weak lensing regime. The KS analysis assumes that second order terms in $\partial \vec{\beta}/\partial \vec{\theta}$ can be neglected. When the bending angle changes rapidly this assumption is no longer valid. We will discuss and illustrate further the effects of non-linearity in Section 2.5.

2.4 Creating and Analysing Simulated CCD Images

Our aim now is to simulate B-band CCD images of lensed field galaxies. We assume that stars and the typically redder cluster galaxies have been identified and removed from the image. The CCD specification that we adopt is 1984 by 1984 pixels each of size ~ 0.3 arcseconds on a side. These numbers were chosen to correspond to some observational data that we had obtained (Wilson et al. 1996). The magnitude limit we adopt is intended to correspond to what is currently achievable in one night on a 4-metre telescope.
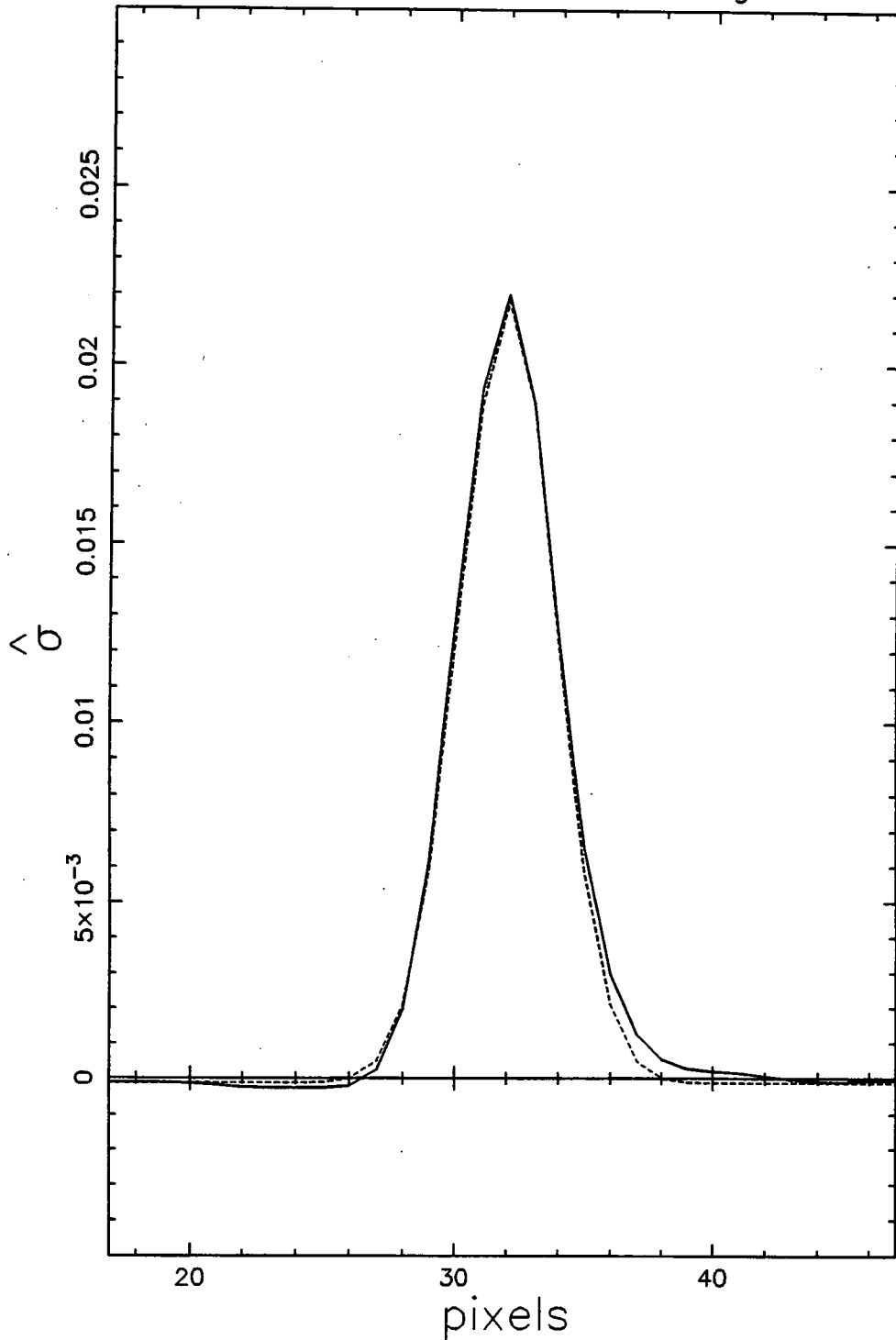
Figure 2.2: A comparison of the mean of five reconstructions (solid line) and the original mass surface overdensity (dashed line). The figure shows a cross-section through the centre of a Gaussian mass distribution and the agreement is excellent.
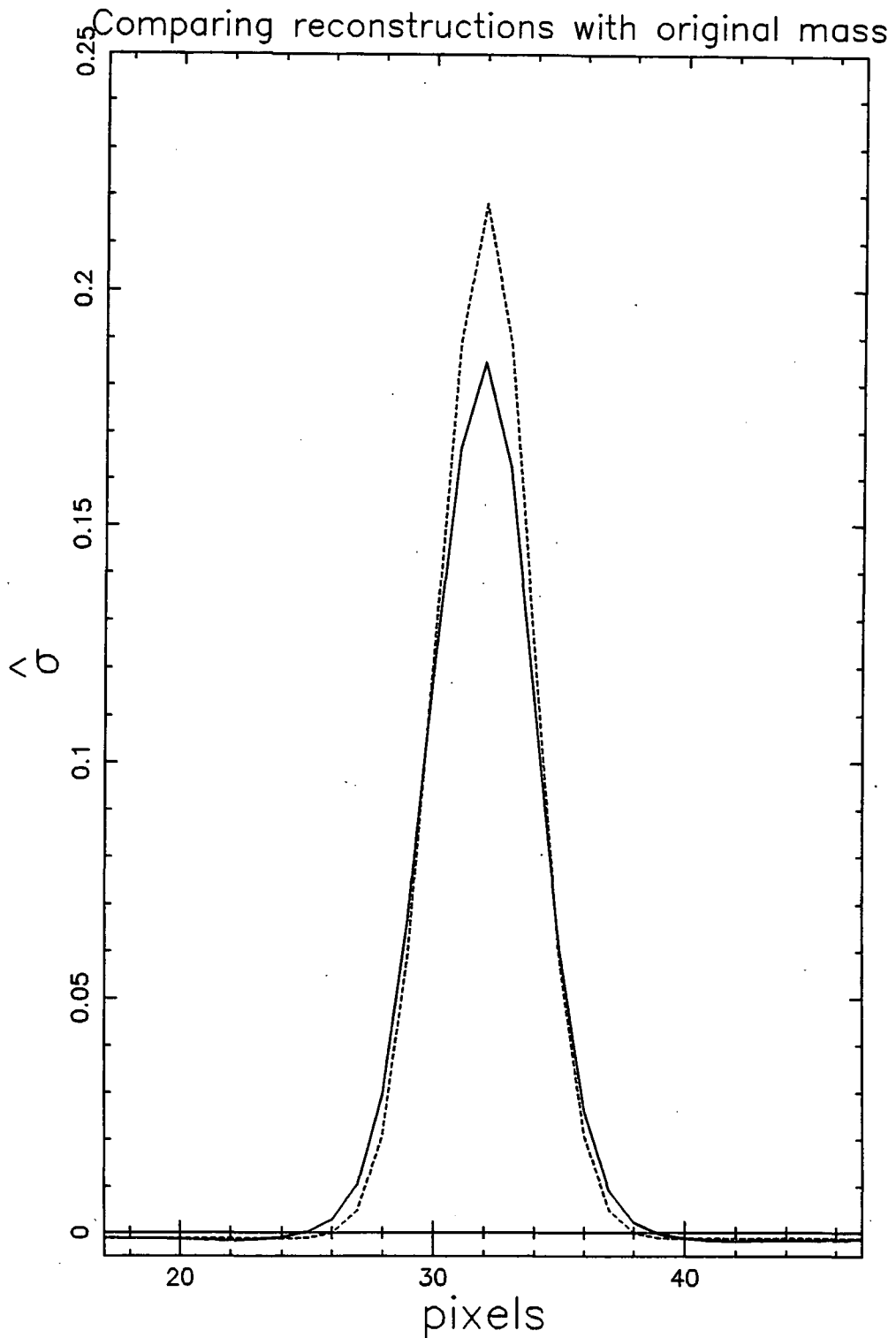
Figure 2.3: A comparison of the mean of five reconstructions (solid line) and the original mass surface overdensity (dashed line) as in figure 2.2. Note how, in this case, the reconstruction underestimates the surface overdensity near the peak.

Magnitude	Number deg^{-2} (0.5mag)$^{-1}$
23.0	3500
23.5	7000
24.0	10000
24.5	18000
25.0	25000
25.5	40000
26.0	60000
26.5	90000
27.0	100000
27.5	120000

Table 2.1: Metcalfe's counts

2.4.1 The Source Planes

The distributions of galaxy size, ellipticity and redshift that we adopt are detailed below. These are intended to provide a realistic description of the mean distributions applicable to the majority of the galaxies which enter into the reconstruction analysis. We simulate background galaxies with apparent magnitudes spanning the range $23.25 < m_B < 27.75$, but the majority of the galaxies which enter our analysis have magnitudes close to the limit, $m_{cut} = 25\text{--}26$, which we impose in order to select a sample with well defined shapes and orientations (see Section 2.5.1). The inclusion of galaxies substantially fainter than m_{cut} is required because the small proportion which happen to lie directly behind the cluster centre will undergo sufficient lensing amplification to subsequently fall within the detection limit. We adopt size, ellipticity and redshift distributions typical of those for galaxies with apparent magnitude $\sim m_{cut}$ and, for simplicity, we ignore variations in these distributions with apparent magnitude. We are less concerned here with modelling the genuine galaxy population which will, in all probability, be extremely complex, than with modelling a sensible but simple population whose effects on the signal can more easily be followed.

- Redshift and magnitude distributions

  As a reasonable redshift distribution for the simulated galaxies, we have adopted the $m_B = 25$ distribution predicted by the analytic model of galaxy formation of Cole et al. (1994). As seen in Figure 20 of that paper, the model has a median redshift of about $z = 1$, with a tail extending to $z = 2.5$. This model is broadly consistent with the redshift distributions of both bright and faint B- and K- selected samples observed at somewhat brighter magnitudes. Since the critical density, S_{crit}, and therefore the bending angle, $\vec{\beta}$, depend on the source redshift through equation (2.6), we discretely sample the redshift distribution and produce a set of source planes spanning a range of redshifts. The net effect on the reconstruction is that S_{crit} is replaced by the mean value

  $$\bar{S}_{crit}^{-1} = \int \frac{1}{S_{crit}(z)} p(z)\, dz \qquad (2.18)$$

  where $p(z)$ is the probability that a galaxy lies at redshift z. The distribution of apparent magnitudes we generate directly from the B-band source counts of Metcalfe et al. (1995). The values we use are shown in table 2.1.

- Scale length distribution

  We assume that all the background galaxies are disks with exponential profiles,

  $$I(r) = I_0 \exp\left(\frac{-r}{\lambda}\right) \qquad (2.19)$$

This is a reasonable approximation since field galaxies are predominately disks. The scale length, λ, we choose from a uniform distribution spanning the range 0.25 arcseconds to 0.65 arcseconds, as suggested by observations (Tyson 1996).

- Ellipticity distribution

  We take an empirical ellipticity distribution derived from a single 9.6 x 9.6 arcminute frame in 0.7 − 0.9 arcseconds seeing on the 200 inch Hale telescope at Palomar (Brainerd et al. 1996). There are about 6000 galaxies catalogued in this frame and we sample their ellipticities at random. Figure 2.4 shows the frequency of axial ratio $\frac{b}{a}$ for the sample. For a given magnitude and scale length, more elliptical galaxies have higher surface brightness. This is because we assume conservation of intensity (i.e. no dimming by dust) and, since elliptical galaxies present a smaller cross-sectional area than face-on circular galaxies, they have a higher flux per unit area. Note that including a distribution of intrinsic ellipticity is equivalent to adding a noise term in the KS reconstruction procedure and this adds noise to the final surface overdensity map. This is because intrinsic ellipticity introduces scatter into the measured values of $\langle e_i \rangle$. Any uncertainty in the $\langle e_i \rangle$ will translate into a corresponding uncertainty in the estimate of surface overdensity via equation (2.8).

We discuss the effects of varying these distributions in Section 2.6.

2.4.2 The Lens

In order to illustrate the effects of seeing and of non-linearities, we initially construct a simple spherically symmetric lens with a Gaussian mass distribution. Later on, and for the main part of this investigation, we use a dark matter cluster grown in a cosmological N-body simulation as a realistic complex lens. In each case we place the cluster at a redshift $z = 0.18$, which again corresponds to the observations of Wilson et al. (1996). The N-body cluster, described in detail in Frenk et al. (1996), comes from a high resolution simulation of a cluster which was initially identified in a simulation of a box 360 Mpc on a side of an $\Omega_0 = 1$, $H_0 = 50$ km s^{-1}Mpc^{-1}, cold dark matter universe (Davis et al. 1985). The initial conditions for the cluster were extracted from this large simulation and, after adding appropriate additional high frequency noise, the cluster was simulated again with a P^{3}M code using 262144 particles, this time in a box of size 45 Mpc. The spatial resolution in the simulation was 35 kpc and the mass per particle $2.5 \times 10^{10} M_\odot$. The cluster has a one-dimensional velocity dispersion of ~ 800 km s^{-1}.

Our aim is now to calculate the bending angle on a grid of points corresponding to the centres of pixels in the lens plane (Section 2.4.3). Using equations (2.4) and (2.5) we obtain the following relationship between the bending angle and the surface density

$$\nabla . \vec{\beta} = \frac{2S}{S_{\text{crit}}} \qquad (2.20)$$

It turns out that this equation is most easily solved in k-space, using Fast Fourier Transforms. In practice, we calculate the bending angle at a few points on a coarse grid and then use cubic splines to interpolate onto a finer grid.
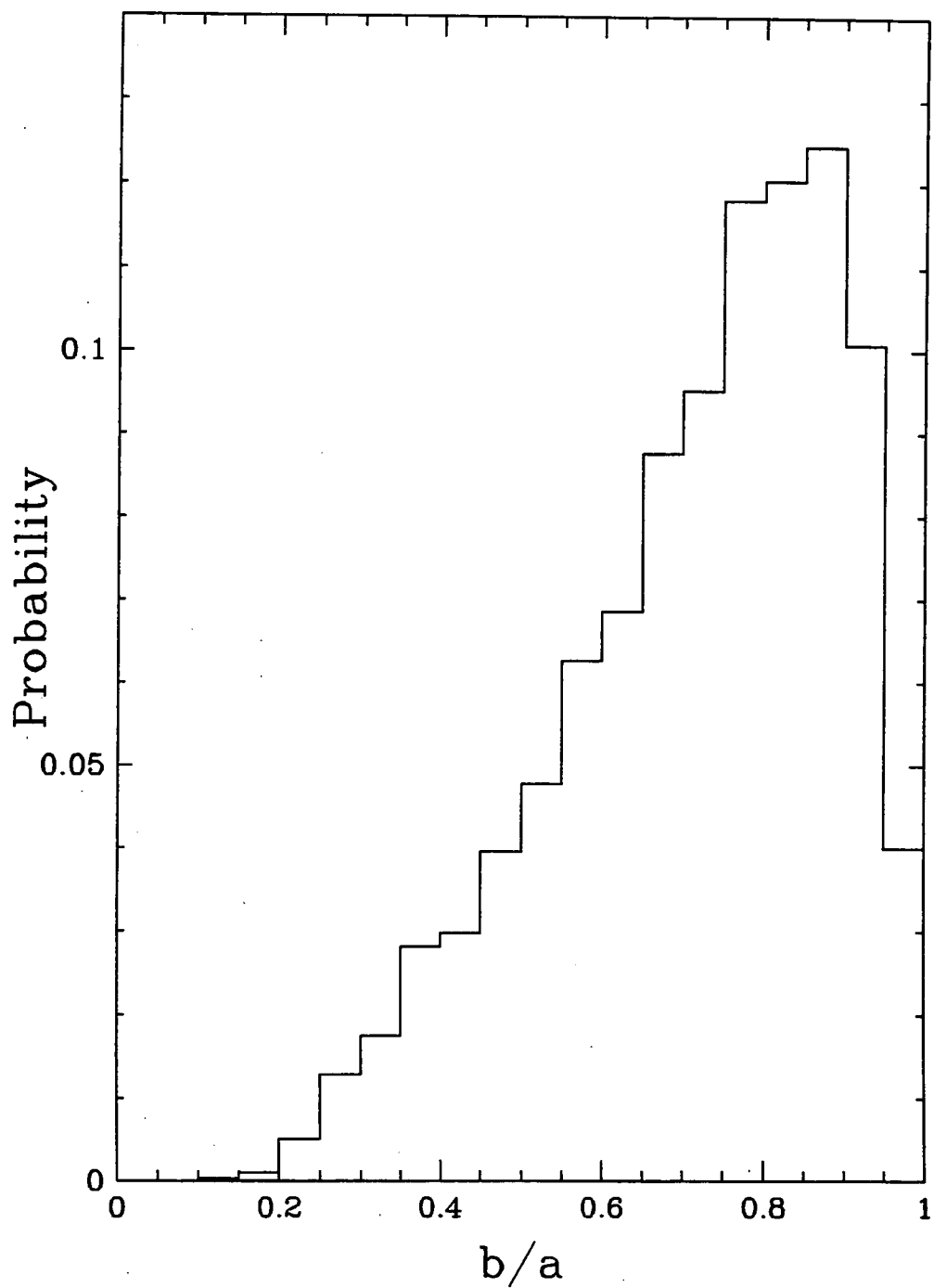
Figure 2.4: The frequency of occurrence of each b/a value, where b/a is the ratio of
the semi-minor to semi-major axis of the galaxy.

2.4.3 The Image Plane

Next, we simulate the corresponding image plane. In the weak-lensing regime the bending angle varies continuously and smoothly across the lens plane. Thus, to a good approximation, we can construct the image plane by mapping pixel by pixel the image plane onto the source plane. The formula linking the positions of source points and corresponding image points is equation (2.2). This formula allows $\vec{\theta}_s$ to be expressed uniquely in terms of $\vec{\theta}_i$, but not $\vec{\theta}_i$ in terms of $\vec{\theta}_s$. For each image pixel we apply this formula and obtain the corresponding point in the source plane. We then assign an intensity to the image pixel by simple bilinear interpolation of the intensities in the nearest four source pixels. This procedure results in a near perfect CCD image of the lensed galaxies. Finally, we add noise to the frame and then convolve it with a Gaussian of width θ_{see} to simulate sky noise and atmospheric seeing.

2.4.4 The Inversion

We analyse the image built up in this way using FOCAS. FOCAS (Faint Object Classification and Analysis System) is a software reduction package developed by Jarvis & Tyson (1981) specifically for measuring properties of faint galaxies. Galaxies have to satisfy certain criteria in order to be "detected". The user specifies an acceptable level of intensity and a minimum area. After detection FOCAS grows an isophote around each galaxy until it extends as far as the sky noise. The shape of the galaxy is then evaluated within this isophote. The values of intensity-weighted second moments from FOCAS are used to define the ellipticity components e_1 and e_2 that feed into equation (2.8) to yield the estimated surface overdensity.

The upper panel in Figure 2.5 shows the surface overdensity distribution of the N-body cluster evolved to redshift $z = 0.18$, placed at the corresponding distance and smoothed with a Gaussian of $\theta_{sm} = 0.25$ arcminutes. The lower panel shows, at the same resolution, the reconstructed surface overdensity map obtained from our simulated CCD image in 1 arcsecond seeing. Although noise features are clearly visible in the reconstruction, the overall morphology is remarkably accurate, reproducing all the major features of the original cluster. We show these plots here as an illustration of the power of the method. In the next section we will investigate the accuracy of the reconstruction in more detail.

2.5 The Reconstruction Method In Practice

In practice observations of gravitational lensing will not conform to the ideals assumed by the KS reconstruction method. The two most important limitations of real observational data are seeing and noise.
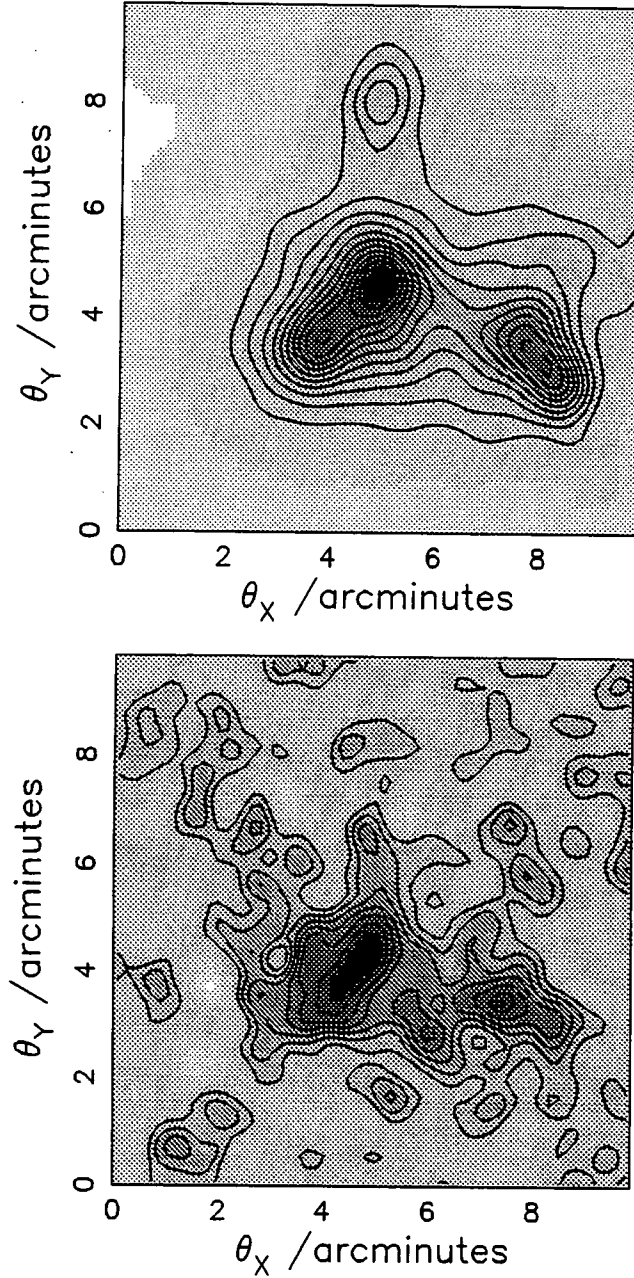
Figure 2.5: The upper panel shows the projected surface overdensity of the N-body cluster which we use as the gravitational lens. The cluster is at a redshift of $z = 0.18$ and the surface overdensity has been smoothed with a Gaussian of $\theta_{sm} = 0.25$ arcminutes. At this redshift 1 arcminute corresponds to approximately 0.24 Mpc. The lower panel shows the corresponding reconstruction produced from a deep image in 1 arcsec seeing. In each panel the lowest contour corresponds to $\sigma = 0$ and the contour spacing is $\Delta\sigma = 0.025$. Note that σ is the surface density in excess of the mean measured in units of the critical surface density for lensing (see equation 2.6). For the redshift distribution assumed in this case $S_{crit} = 3.3 \times 10^{15} M_\odot/\mathrm{Mpc}^2$

19

- Seeing

  Seeing is the distortion of images produced by scattering of light as it propagates through the Earth's atmosphere. Point sources become finite in extent and extended sources like galaxies undergo a corresponding blurring. The resulting effect is to make the galaxies appear more circular. This masks the true elongation of lensed galaxies, making the lens appear less strong and hence reducing the lensing surface overdensity recovered by the KS method.

- Noise

  Noise is any spurious signal introduced during the detection process. There are various categories of noise e.g. photon noise, background noise or detector noise. When observing faint galaxies the most important source of noise is the sky background. The shapes of faint galaxies can be grossly distorted by noise. This can confuse the lensing analysis, so very faint galaxies need to be excluded (see Section 4.1).

In addition the KS technique will also break down if the surface density of the lens is too high.

- Non-linearity

  The KS technique is applicable only to weak lensing situations, when second order shear terms are negligibly small i.e. the bending angle varies only slowly, $\partial\vec{\beta}/\partial\vec{\theta} \ll 1$. If the cluster surface overdensity is large and varies rapidly this assumption is no longer valid and strong lensing techniques must be employed.

We illustrate the effect of seeing and non-linearity in Figure 2.6. Here we use a simple spherically symmetric lens with a Gaussian mass profile. We vary both the seeing and the mass of the lens, but in each case we keep the noise added to the image frame at a very low level. The factor, f, plotted in both panels of Figure 2.6 is the ratio of the true surface overdensity, σ, at the centre of the lens, to the corresponding value recovered by the KS technique. The upper panel shows f as a function of the central surface overdensity of the Gaussian lens, for a fixed seeing of $\theta_{see} = 1$ arcsecond. We can see that f is constant up to about $\sigma = 0.1$ and then increases with increasing surface overdensity, implying that non-linear effects are becoming important for surface over-densities greater than this value and the weak lensing approximation is beginning to fail. The lower panel shows f as a function of seeing. Here the central surface overdensity of the Gaussian is kept fixed at $\sigma = 0.1$ which, from the upper panel, is still in the regime where the weak lensing approximation appears valid. We can see that f increases rapidly as the seeing worsens.

It is not easy to correct for the systematic error caused by non-linearity. Thus, if the surface overdensity at the centre of massive clusters is to be accurately estimated, alternative methods must be employed which take account of non-linearity (Seitz & Schneider 1995a; Kaiser 1995). Note, however, that the systematic error is only of
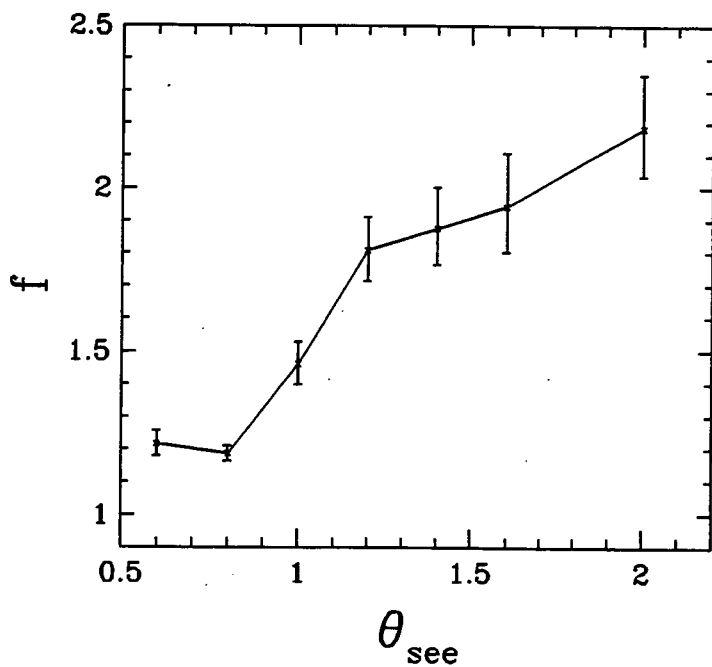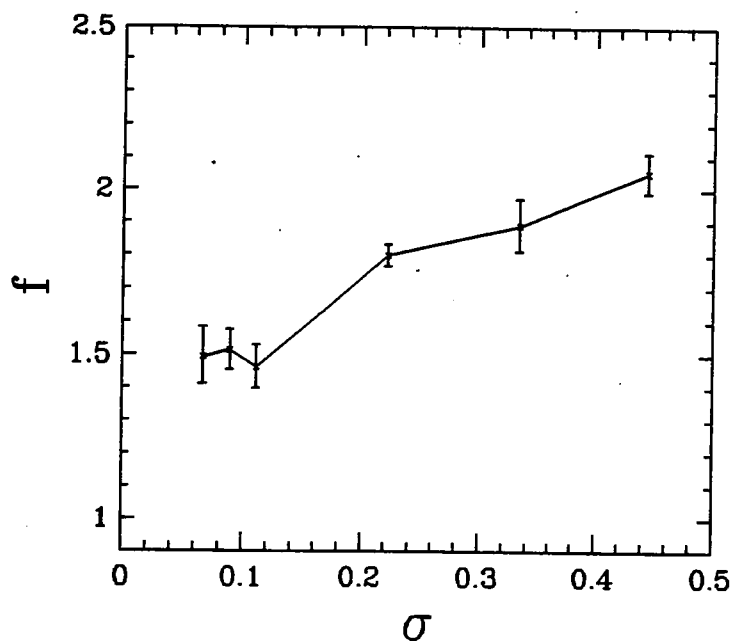
Figure 2.6: The ratio, f, of the true central surface overdensity of the lens to the central surface overdensity recovered by the KS technique. The upper panel shows the dependence of f on the central surface overdensity of the lens for fixed seeing conditions of $\theta_{\text{see}} = 1$ arcsecond. The lower panel shows the variation of f with θ_{see} for $\sigma = 0.1$.

that the reason why f does not tend to unity at low values of σ, in the upper panel of Figure 2.6, is the 1 arcsecond seeing, not residual non-linearity.) Elsewhere in the cluster the systematic error will be smaller.

The systematic error due to the blurring effect of seeing is potentially much larger. If we were able to tabulate the ratio f for all observing conditions, then this table could be used as a compensation factor to correct the surface overdensity estimates returned by the KS technique. However, this is not practical since the effect of seeing depends not only on the value of θ_{see}, but also on intrinsic properties of the galaxy images used in the reconstruction. For example, the degradation due to seeing increases as the angular size of the galaxy images used decreases. To circumvent this problem we outline a calibration procedure in Section 2.5.2 which can be used to estimate the required compensation factor, f, for any given observational dataset.

2.5.1   Defining the Galaxy Sample

In our simulations we have assumed that stars and cluster galaxies have been removed from the CCD image. In practice, since cluster galaxies are mostly E/S0's and are all at approximately the same redshift, they have very similar colours and, provided two colour information is available, they are relatively easy to identify. On a colour-magnitude diagram of all objects within the frame, the cluster galaxies will fall on a (nearly) horizontal line (see e.g. Smail 1993 or Chapter 4) and can be excluded from any subsequent lensing analysis.

The value of the signal-to-noise ratio in our simulations has been chosen to mimic detections of galaxies down to $m_B = 26.5$. The signal-to-noise ratio is found empirically, by generating small artificial CCD frames , populating them with $\simeq 50$ circular galaxies, gradually reducing the noise level, and then running FOCAS on the resulting frames until all the galaxies are detected from one frame.

Although all galaxies down to this magnitude limit of $m_B = 26.5$ are detected in the simulated CCD frame, the faint galaxy shapes are badly contaminated by noise. Thus, it is necessary to make a cut at a brighter magnitude in order to exclude these faint galaxies from the analysis. We find that a useful guide to selecting this magnitude cut comes from looking at the ellipticity distribution of the galaxy images as a function of apparent magnitude. It is to be expected that the intrinsic distribution of $e = \sqrt{e_1^2 + e_2^2}$ will be a slowly varying function of apparent magnitude. It is, in fact, assumed to be constant in our simulations. Thus, a sudden change in the shape of this distribution at faint magnitudes can most likely be attributed to the onset of noise in the image corrupting the shapes of the faint galaxies. As a quantitative comparison, we divide the data into half magnitude bins and compare the ellipticity distribution in each bin in turn with a representative bright sample using the Kolmogorov-Smirnoff comparison test. The Kolmogorov-Smirnoff test is the most common test used for deciding whether two unbinned distributions which are functions of a single independent variable (in this case, e) are drawn from the
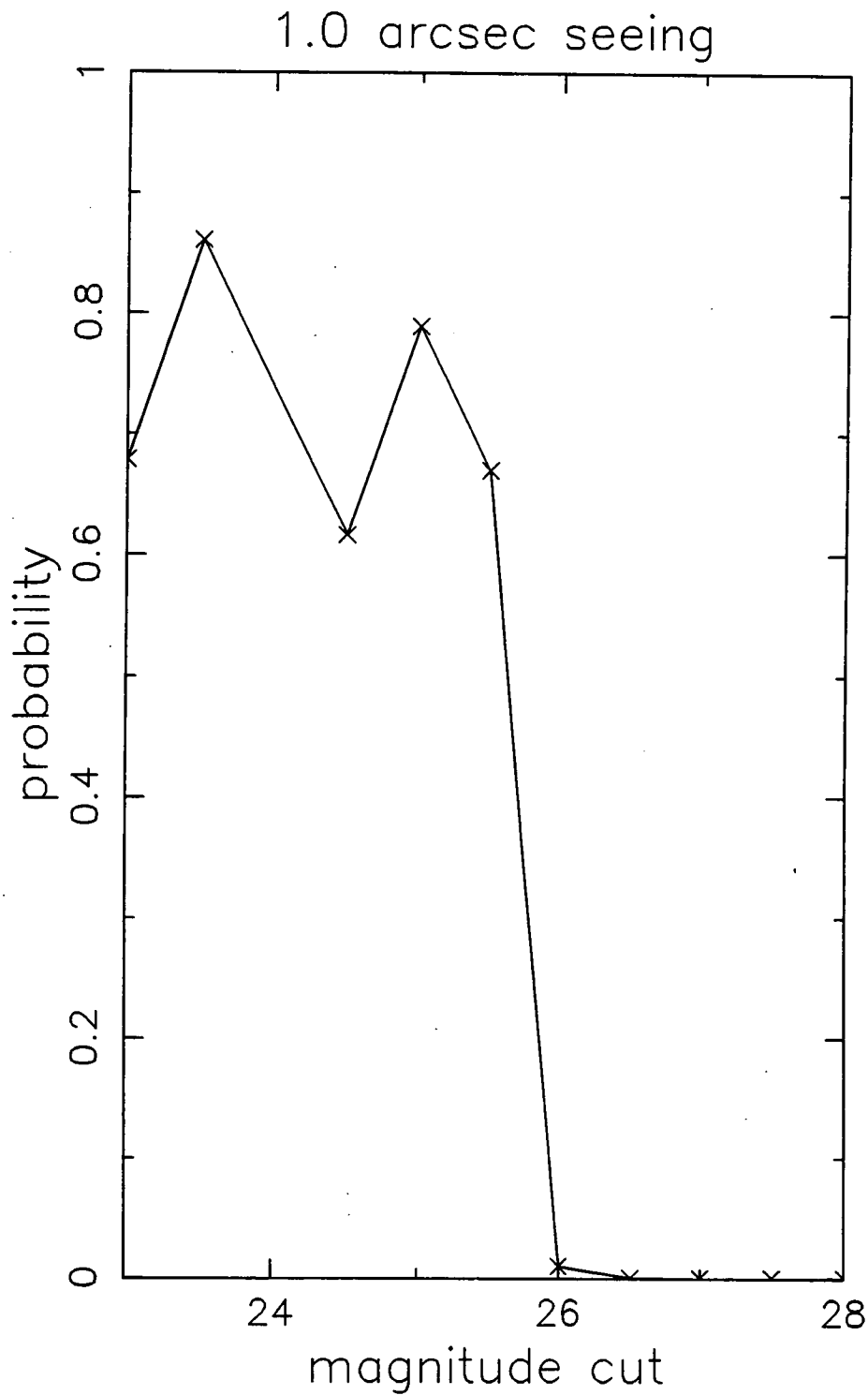
Figure 2.7: The probability that galaxies in any given half-magnitude subsample are drawn from the same distribution of ellipticities as that of the 23.75 to 24.25 subsample. The probabilities are calculated by means of a Kolmogorov-Smirnoff comparison test. Populations fainter than m=25.5 are inconsistent with the brighter populations.

same population. The Kolmogorov-Smirnoff test compares two such distributions (here the ellipticity distribution for a bright magnitude, [23.75,24.25], and a fainter counterpart) using the maximum value of the absolute difference between the two cumulative probability distributions. This maximum value can be translated into a probability that the two distributions are drawn from the same population. As can be seen from Figure 2.7, the probability that the two distributions are drawn from the same population plummets to virtually zero at magnitudes fainter than m=25.5. We have found this transition to be a good indication of where to place the magnitude cut used to define the sample of galaxy images to be fed through the KS reconstruction technique. The appropriate value of the cut will depend, of course, on the specific observational setup.

2.5.2 Calibration of Mass Estimator

In this section we describe how to calibrate a CCD frame for use in the KS reconstruction method. Specifically, we show how to compute a compensation factor, f, that corrects for the bias in the surface overdensity estimates returned by the KS method. Briefly, the procedure involves shearing the galaxy images by a known amount, adding seeing and measuring the resultant shear. The compensation factor, f, is then the ratio of the input shear to the measured shear.

If one takes the image frame, multiplies the x-coordinate of each pixel by a factor $1 + \epsilon$, and rebins, then all the galaxy images will be sheared in the x-direction. If ϵ is small and the initial distribution of ellipticities is not too broad then it is easy to show from the definitions (2.9) and (2.10) that the ellipticity component e_2 of each galaxy is unchanged while the e_1 component is on average increased by ϵ (see Appendix B). If the galaxy images are then blurred by seeing one will find that the measured change in the shear will be somewhat less than ϵ. Since, according to equation (2.8), the surface overdensity at any given point is proportional to the measured ellipticities, the ratio of ϵ to the mean change in e_1, $\langle \Delta e_1 \rangle$, is in fact the factor f required to correct the surface over-densities, i.e. ,

$$f \equiv \frac{\sigma}{\hat{\sigma}} = \frac{\epsilon}{\langle \Delta e_1 \rangle} \qquad (2.21)$$

This procedure is complicated by two factors. Firstly, the appropriate value of f depends on the sizes of the galaxy images and so one would underestimate it if the shearing process were applied directly to the enlarged blurred observed images. This point is discussed further at the end of this section and illustrated in Figure 2.10. Secondly, the initial distribution of e_1 can be quite broad with some galaxies having values of e_1 approaching unity prior to addition of any further shear. Since e_1 is constrained to be less than unity, these high values of e_1 cannot be increased further. This effect can be seen in Figure 2.8. It is therefore necessary both to deconvolve the image prior to applying the shear and to limit the analysis to galaxies whose original ellipticity is less than some value, e_{cut}.

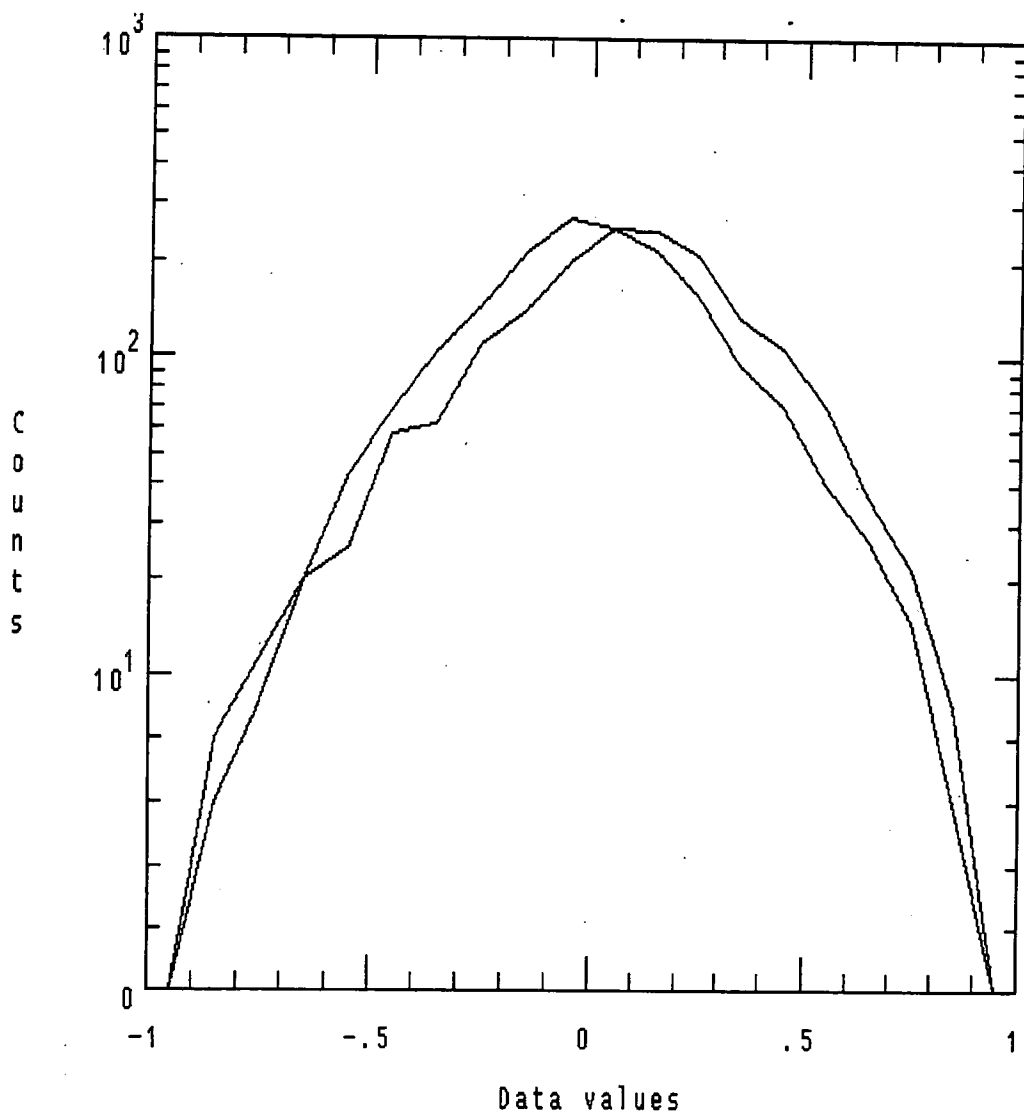In summary, our calibration procedure consists of the following steps:

24

Figure 2.8: Number of galaxies plotted against e_1 for the unsheared (left line) and sheared (right line) frames. Note that the unsheared case is centred on zero and that in the central regions the corresponding sheared galaxies have values of e_1 offset by ~ 0.1. Note in particular the convergence of the lines at ± 1 where already highly elliptical galaxies cannot reflect further stretching.

25

1. Deconvolve the CCD image using the Point Spread Function measured from one or more stars on the frame. Note that since no analysis is to be made using the deconvolved images, it is not necessary to use sophisticated noise suppressing deconvolution algorithms. Neither is it required to model the PSF in great detail. A Gaussian fitted to the measured PSF is probably adequate.

2. Stretch the galaxy images along the x-axis by a known factor, $1 + \epsilon$, and rebin. A value of $\epsilon \sim 0.1$ is appropriate as this is typical of the values produced by weak lensing.

3. Reconvolve the stretched image with the same PSF.

4. Run reduction software on both the original image and this new stretched image and compute the ellipticity components e_1 and e_2 for each galaxy.

5. Select the galaxies with measured values of $e < e_{cut}$ in the original frame and, for these, compute the mean change in e_1, $\langle \Delta e_1 \rangle$, between the original and stretched frames. Define the compensation factor $f = \epsilon / \langle \Delta e_1 \rangle$.

6. Estimate the lens surface overdensity using the KS method, equation (2.8), with the galaxies selected using the same cut in e as above. Finally, multiply the resulting surface over-densities, $\hat{\sigma}$, by the factor f to yield corrected estimates.

Figure 2.9 shows estimates of f obtained by this procedure from simulated CCD frames constructed with realistic signal-to-noise ratios and galaxy populations. Each point is the average obtained from 10 simulated CCD images. The curve shows the compensation factor f for the choice $e_{cut} = 0.5$. As expected, we see that f increases rapidly as seeing worsens and that even for good seeing conditions it is significantly different from unity.

Figure 2.10 is similar to Figure 2.9. The upper line is the compensation factor f for the choice $e_{cut} = 0.5$ from Figure 2.9. The figure illustrates that step (i) of the calibration is vital. The lower line shows values obtained for the same cut but omitting step (i), the deconvolution. The value of f for the seeing-enlarged galaxies (lower line) is underestimated.

We use values of f calculated using the calibration procedure outlined above in the next section and show that they give remarkably good estimates of the true surface overdensity.

2.6   Examples and Discussion of Results

We now examine a series of test cases where we explore the success and reliability of the calibrated reconstruction technique for a range of observational conditions and sample selections.
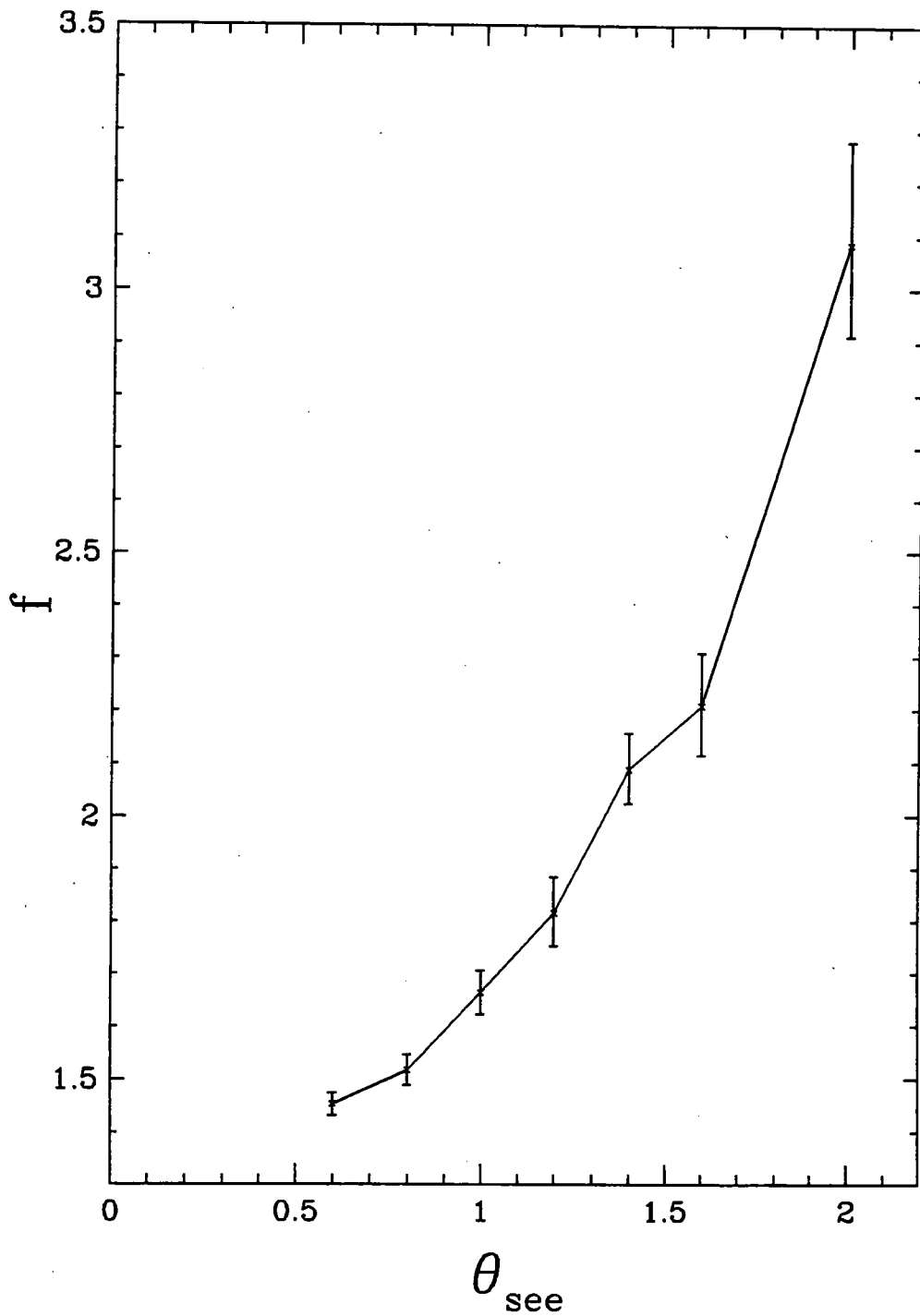
Figure 2.9: The compensation factor, f, versus seeing in realistic signal-to-noise conditions. The line shows the values obtained for $e_{\mathrm{cut}} = 0.5$.
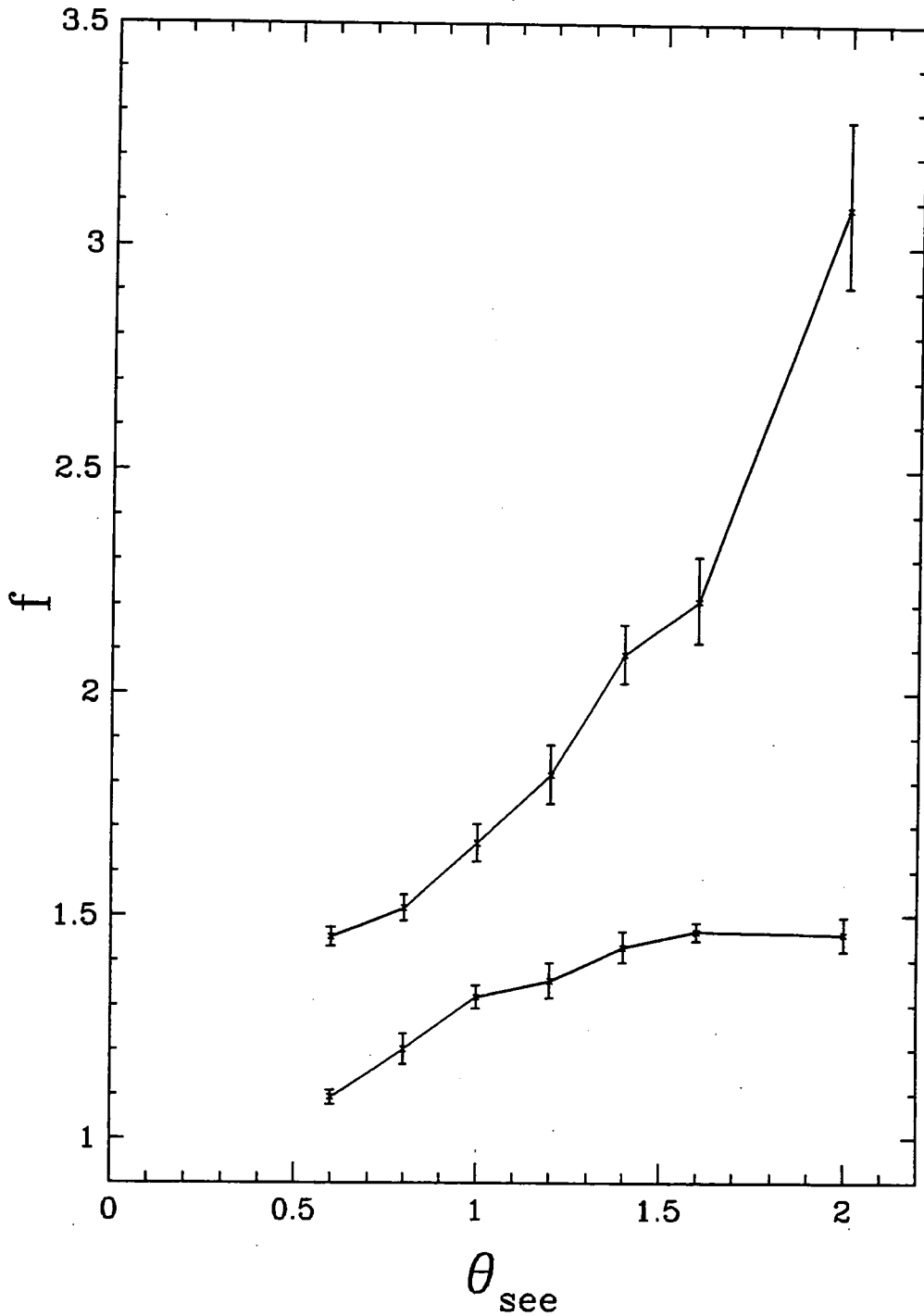
Figure 2.10: The compensation factor, f, versus seeing in realistic signal-to-noise conditions. The upper line shows the values obtained for $e_{cut} = 0.5$ as in figure 2.9 and the lower line shows values obtained for the same cut but omitting step (i), the deconvolution. Clearly it is necessary to include deconvolution or f is underestimated.

2.6.1 The Effect of Seeing

Figures 2.11, 2.12 and 2.13 show the results of the calibrated reconstruction technique for three different values of the seeing, $\theta_{see} = 0.6$, 1.0 and 1.6 arcseconds. The upper panel in each figure shows the reconstruction of the cluster surface overdensity map. This should be compared to the true lens surface overdensity displayed in Figure 2.5. The central panel is a scatter plot of the compensated estimated surface overdensity versus the true surface overdensity sampled in a 62×62 grid covering the region shown in the upper panel. The compensation factor f estimated as described in Section 2.5.2 is shown in the upper left of the panel. The lower panel depicts the mean shear of the galaxies in 10×10 bins, again covering the same area as the map in the upper panel. The length of each line is proportional to the mean ellipticity, $e = \sqrt{\langle e_1 \rangle^2 + \langle e_2 \rangle^2}$, in each cell and the orientations of the lines indicate the direction of the shear.

The first point of note is that the complex morphology of the cluster mass distribution is recovered quite well in all three cases, with only a gradual degradation of the reconstruction as the seeing becomes progressively worse. Second, the value of the compensation factor, f, is a strong function of the seeing, varying from $f = 1.45$ for $\theta_{see} = 0.6$ to $f = 2.21$ for $\theta_{see} = 1.6$. In spite of this, the compensated surface overdensity estimates, $f\hat{\sigma}$, are in good agreement with the true values, σ, i.e. the points in the central panels all scatter around the line $f\hat{\sigma} = \sigma$, with no significant bias. Finally, we note that equation (2.15) appears to be a good approximation to the variance in the surface overdensity estimator; from 9 simulations in 1 arcsec seeing we find a scatter in $\hat{\sigma}$ of 0.052 which compares well with the theoretical value of 0.045.

2.6.2 Variations in the Properties of the Background Galaxies

In our simulations so far we have assumed specific distributions of the sizes, shapes and redshifts of the background galaxies. These are realistic examples but it is nevertheless important to investigate how our results change when they are varied. In Figures 2.14 to 2.17 we explore the effect on the reconstructed surface overdensity maps and scatter plots of varying each of these distributions in turn. In all cases we employ 1 arcsecond seeing and therefore compare our results to Figure 2.12. The factors f are now calculated from a single frame rather than from the mean of ten frames as before, so they will be somewhat less reliable.

In Figure 2.14 we experiment with the sizes of the galaxies by assuming they are 20 percent larger than before. In this case we might expect the scatter in $f\hat{\sigma}$ to remain unchanged, but f to be reduced since the ratio of galaxy size to seeing is increased. Indeed, the scatter in Figure 2.14 is similar to that in Figure 2.12 and the value of f is reduced. The scatter does not change because the ellipticity distribution and the noise, the major contributors to the uncertainty, are unchanged.

In Figure 2.15 we explore the effect of varying the distribution of intrinsic galaxy ellipticities. We bias the distribution slightly towards less elliptical galaxies, so that the mean axial ratio is $b/a = 0.79$ rather than $b/a = 0.71$ as before. We see from the figures that the resulting effect is to reduce the scatter in accordance with equation (2.15). Although the value of f shown here is slightly diminished, the mean value of f from 5 frames is little changed.

In Figure 2.16 we use a deeper distribution of galaxy redshifts, namely placing all the galaxies at $z = 2$. This change reduces the value of S_{crit} (see equation 2.6) and increases the values of σ and $\hat{\sigma}$ proportionally at all grid points. This is the reason for the change of scale on the axes compared with the previous figures. Since the values of σ and $\hat{\sigma}$ increase in the same ratio, the mean value of f is unchanged.

In our final plot, Figure 2.17, we increase the signal-to-noise ratio so that galaxies can now be detected one magnitude fainter than before. The higher galaxy number density greatly reduces the scatter in $f\hat{\sigma}$, as expected from equation (2.15). The compensation factor is also reduced somewhat because the galaxy shapes are now less distorted by noise than before.

2.7   Conclusions

We have performed a series of controlled experiments to assess the reliability of the technique proposed by Kaiser & Squires (1993) to reconstruct the surface mass overdensity of galaxy clusters from observations of weak gravitational lensing. In particular, we have tested the KS method on a realistic cluster mass distribution, typical of those expected in an $\Omega_0 = 1$ universe. By simulating data from standard observing conditions, we have investigated the effects of seeing and signal-to-noise on the reconstructed dark matter maps and we have explored how the results vary with different assumptions for the distributions of intrinsic galaxy shapes and redshifts. Our main conclusions are as follows:

• With a careful analysis of data obtained in standard observing conditions, the KS method provides a remarkably faithful reconstruction of the morphology of a complex cluster, reproducing the richness of structure expected in an $\Omega_0 = 1$ universe.

• Our simulations show that the weak lensing assumption on which the KS technique is based begins to break down when the mass surface overdensity exceeds 10% of the critical surface density. However, even when it equals 30% of the critical value, the KS method underestimates the surface overdensity by only $\sim 25\%$. The noise in the reconstructed maps agrees well with a simple estimate (equation 2.15) of the uncertainties due to Poisson noise and to the scatter in the intrinsic ellipticities of the lensed background galaxies.

• The simple calibration procedure for CCD images which we have designed and tested, efficiently corrects for the effects of atmospheric seeing on the reconstructed

mass surface overdensity maps. This procedure is straightforward to apply to CCD data and yields a multiplicative "compensation factor", f, which allows the true surface overdensity in each pixel (in units of the critical density) to be recovered from the reconstructed map. The *absolute* value of the lens mass cannot be derived by this method unless the critical density, which depends on the redshift distribution of the lensed galaxies, is known. However, the dependence on redshift is fairly weak (see e.g. Figure 5 of Blandford & Kochanek 1987).

• Our method for calculating the compensation factor is quite robust. The value of f is primarily determined by the seeing, but the depth of the CCD image and the intrinsic properties of the lensed galaxies also affect it. Useful results can be obtained even with data acquired in seeing as large as 1.6 arcseconds, although the technique clearly works best with sub-arcsecond seeing. Our simulations indicate that it should work well when applied to data obtained in a wide range of observing conditions, allowing useful mass reconstructions to be made even when the correction factor is as large as $f = 2$.
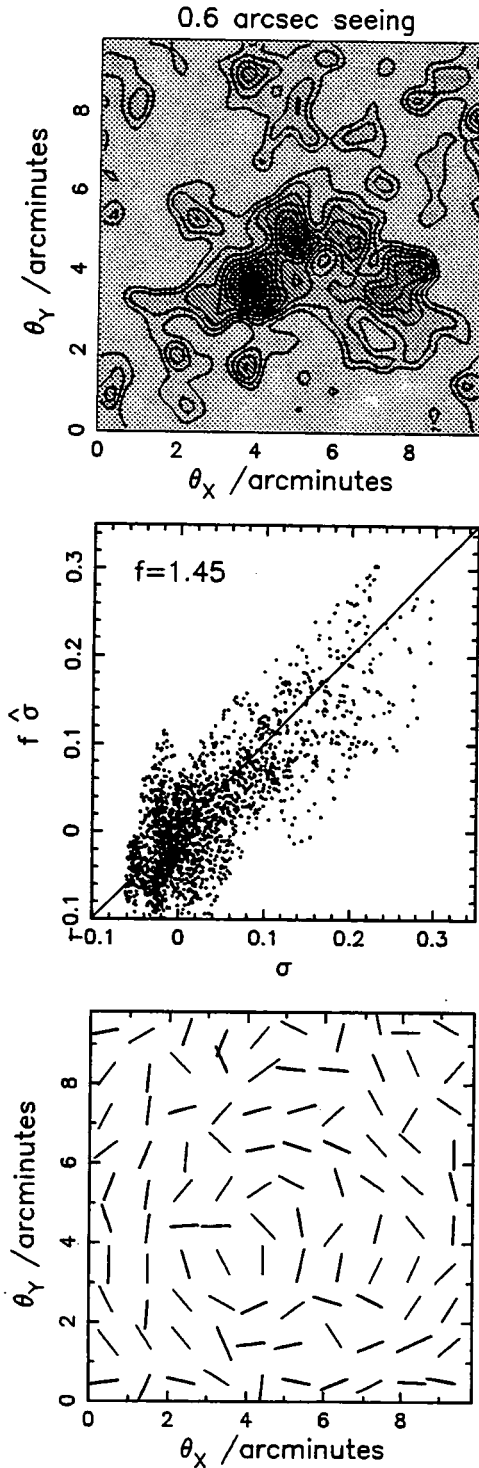
Figure 2.11: For simulated observations taken in conditions of $\theta_{\text{see}} = 0.6$ arcseconds seeing the panels show the reconstructed map of the lens surface overdensity, a scatter plot of the compensated estimated versus true surface overdensity and the estimated shear pattern across the face of the lens, respectively. The value of the compensation factor, f, estimated from this data is also shown on the middle panel. The details of the assumed background galaxy properties are detailed in Section 2.4.1. A magnitude cut, $m_{\text{cut}} = 25.5$, suggested by the Kolmogorov-Smirnoff test of Section 2.5.1, and an ellipticity cut of $e_{\text{cut}} = 0.5$ were used to define the galaxy sample that was analysed.
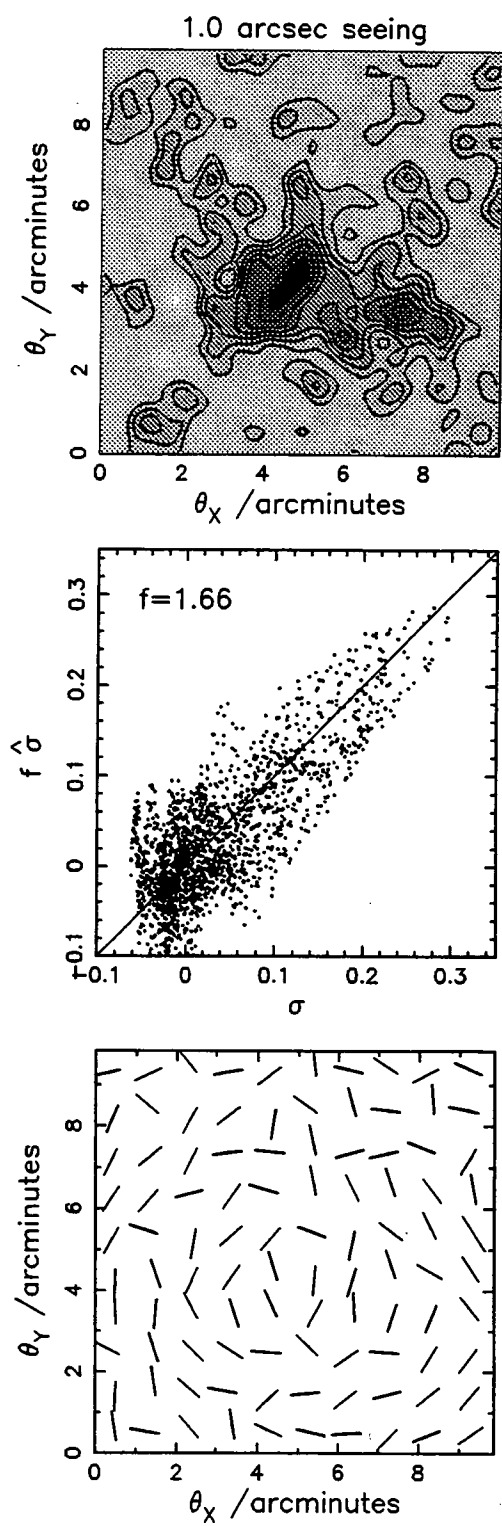
Figure 2.12: As Figure 2.11 but for seeing of $\theta_{\text{see}} = 1.0$
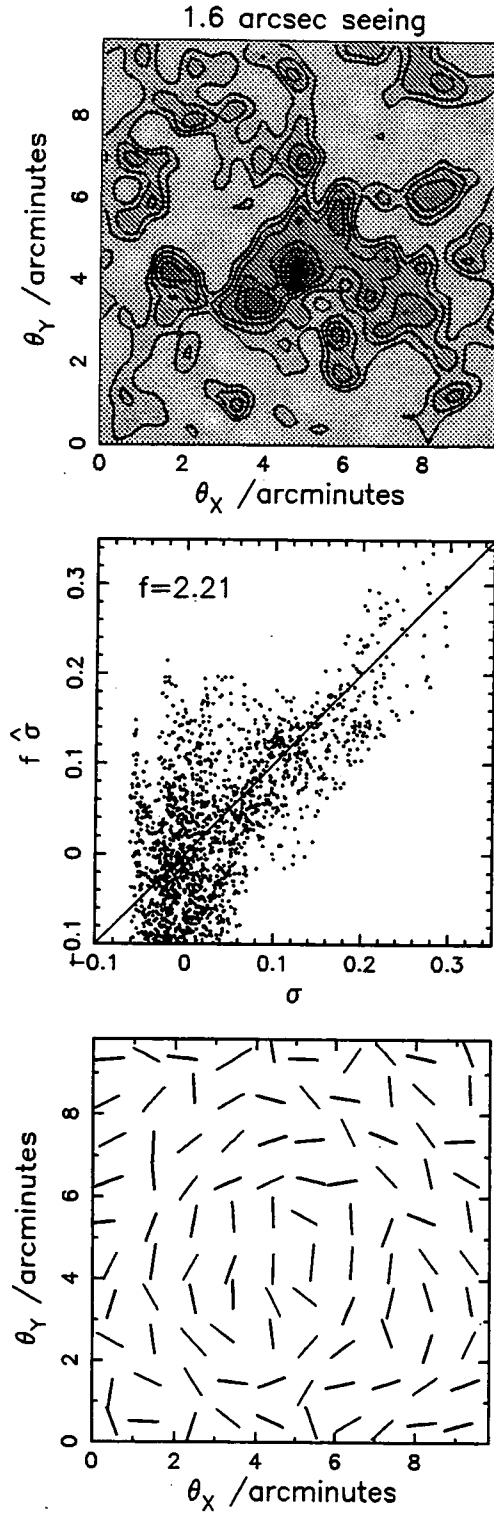
Figure 2.13: As Figures 2.11 and 2.12, but for seeing of $\theta_{see} = 1.6$ arcseconds.
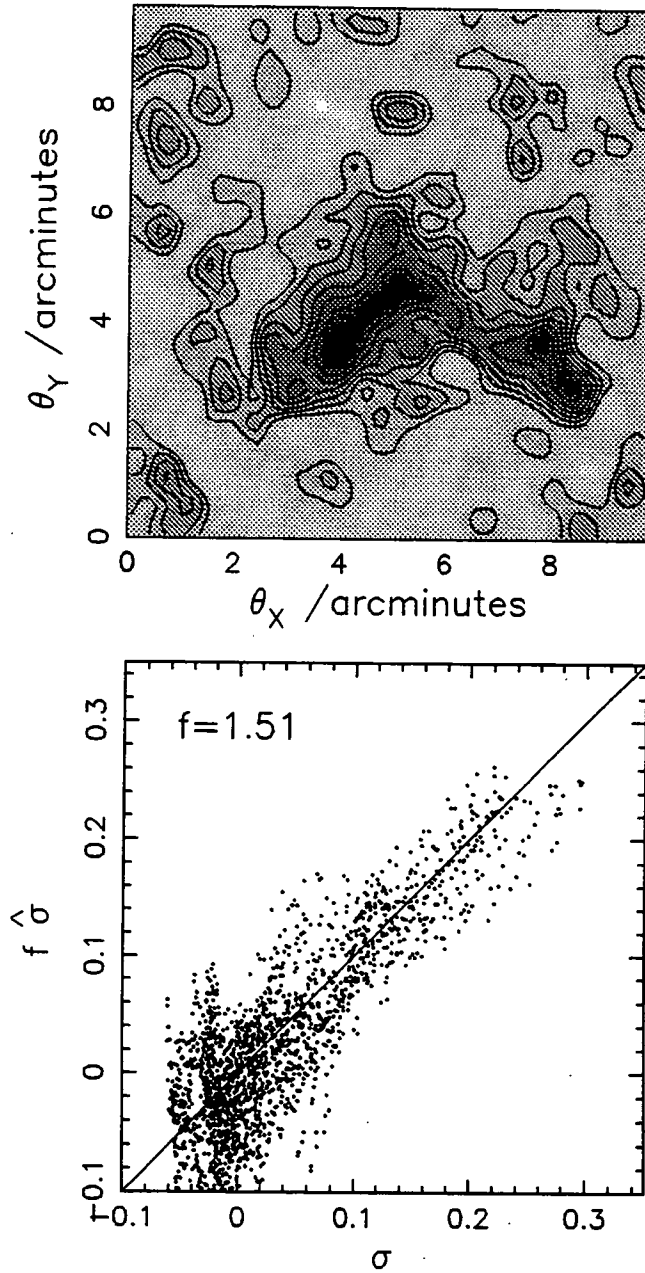
Figure 2.14: The reconstructed surface overdensity map and scatter plot for $\theta_{\text{see}} =$ 1.0 arcseconds (as in Figure 2.12), but for galaxies with scale lengths 20% larger than assumed in Figure 2.12.
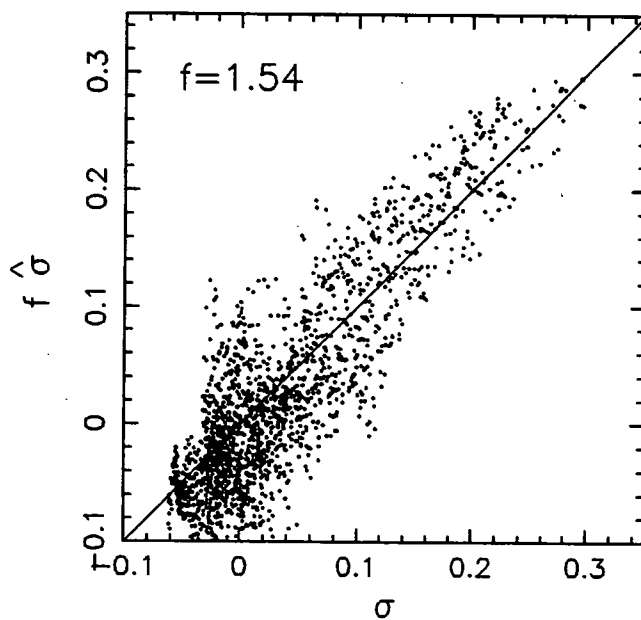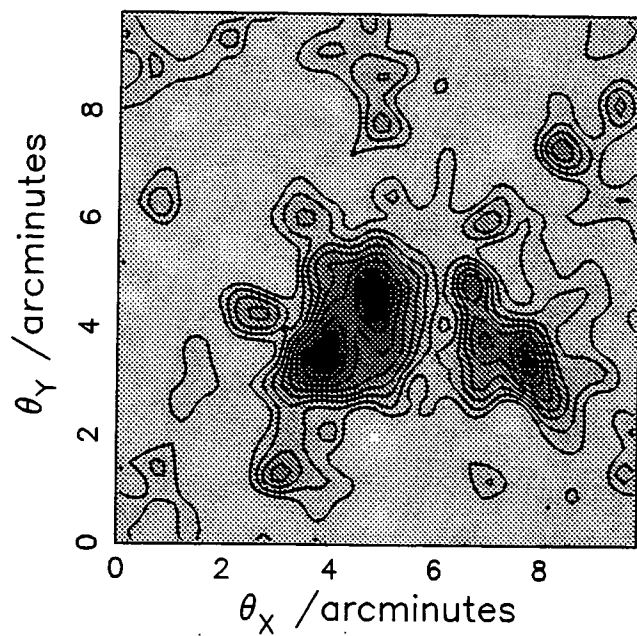
Figure 2.15: As Figure 2.12, but for a narrower distribution of intrinsic ellipticities for the background galaxies. The mean of b/a is now 0.79 compared with 0.71 in Figure 2.12.
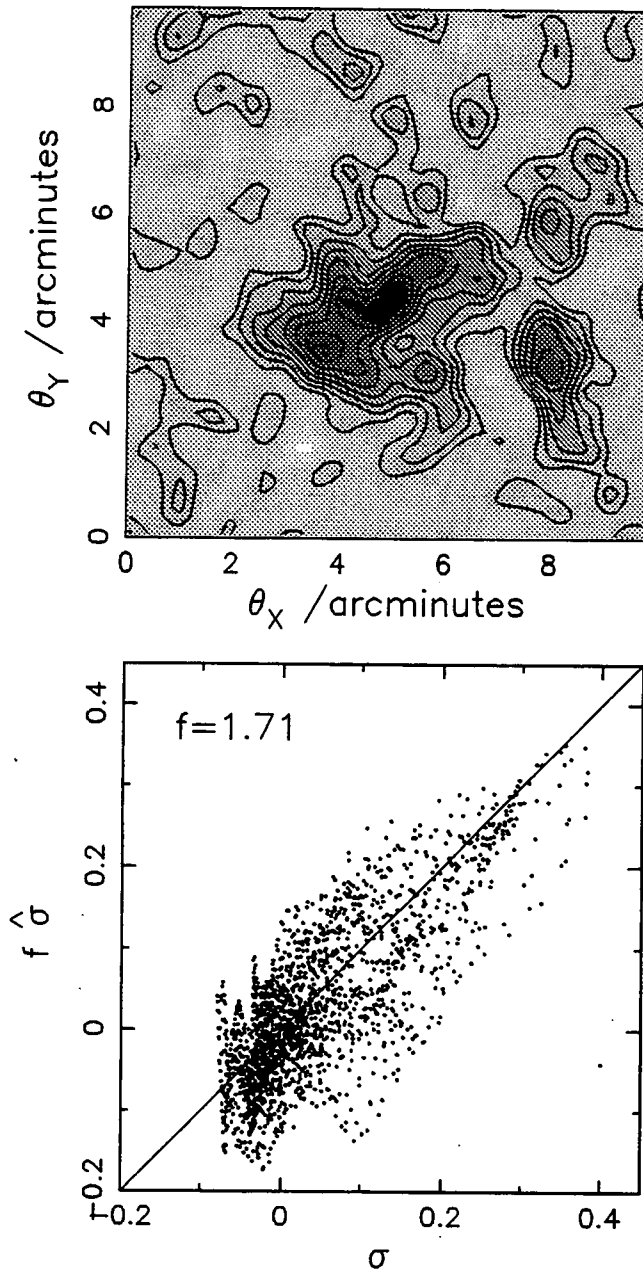
Figure 2.16: As Figure 2.12, but with the background galaxies all at redshift $z = 2$.
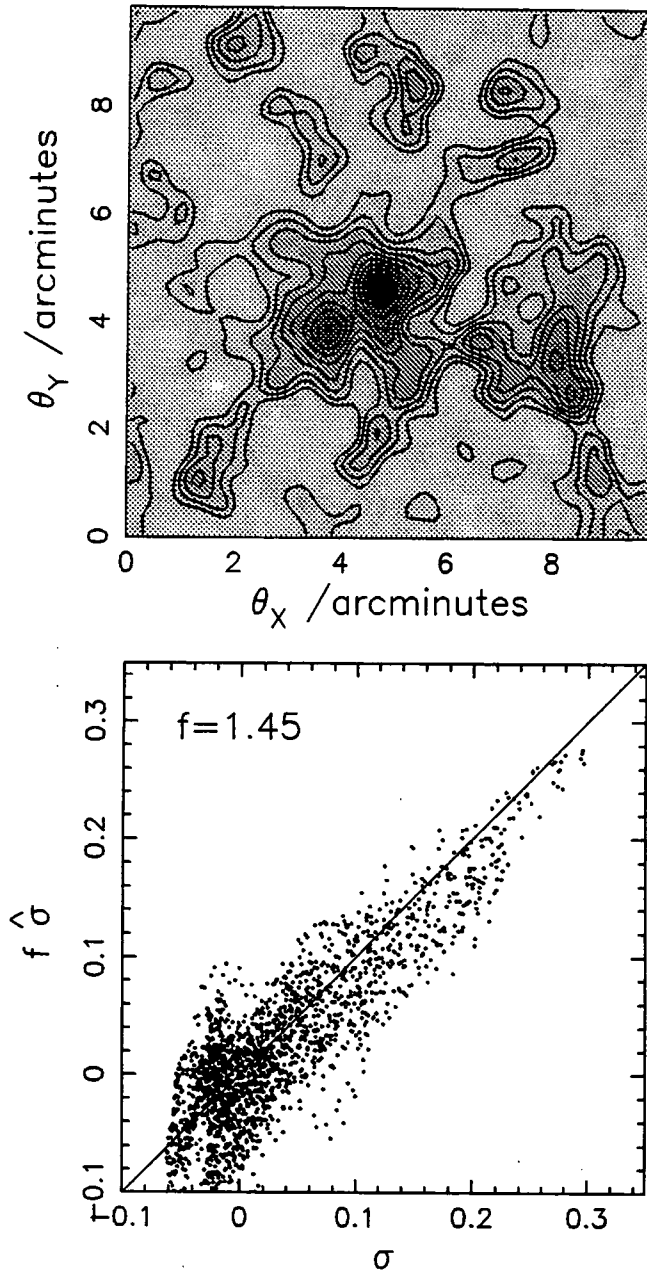
Figure 2.17: As Figure 2.12 , but for a deeper CCD frame in which galaxies down
to $m_{cut} = 26.5$ are retained.

Chapter 3

Cluster Morphology

3.1 Introduction

Our aim in this chapter was to simulate weak lensing through clusters from three different cosmologies. For our lenses, we used a set of clusters from Evrard et al. (1994) . The motivation behind these cluster simulations was to investigate whether cluster morphologies could be used as constraints on the cosmological "constants", Ω_0 and λ_0. (The subscript 0 denotes the value at the present day). Ω_0 is the ratio of the actual mass density of the Universe to the critical density required for closure. λ_0 is the so-called cosmological constant measured in units of $3H_0^2$, where H_0 is the present value of the Hubble constant. (Throughout this chapter we use $H_0 = 50$ km s^{-1} Mpc^{-1}).

In the initial paper by Evrard et al. (1994), and also in a second paper (Mohr et al. 1995), it was demonstrated that, in agreement with analytic predictions (Richstone et al. 1992; Lacey & Cole 1993), cluster evolution was sensitive to the cosmological model. In a low Ω_0 universe, density fluctuations cease to grow after a redshift $z \sim \frac{1}{\Omega_0} - 1$ (See e.g. Peebles 1980, Sections 11 & 13). Introducing a cosmological constant makes this cessation more abrupt. Hence, in low Ω_0 models, both with and without cosmological constants, clusters form at moderate redshift ($z = 1$–4), and then accrete very little material. In this period, which can span many dynamical times, the internal structure of the clusters relaxes to produce smooth, near spherical, density profiles. In contrast, if $\Omega_0 = 1$, structure formation is continuous, galaxy clusters form at very low redshift ($z = 0.2$–0.3), and continue to accrete material even at the present epoch. Hence, for $\Omega_0 = 1$, many clusters will show evidence of having undergone a recent merger and will have irregular morphologies.

Over the past few years a number of observational optical and X-ray studies (e.g. Geller & Beers 1982; Dressler & Schectman 1988; West & Bothun 1990; Forman & Jones 1990; West et al. 1995) have suggested that a significant proportion, perhaps $\sim 40\%$ of clusters have evidence of substructure. Motivated by these interesting but

controversial observations suggesting recent cluster growth, Evrard et al. (1994) calculated X-ray maps from the gas particle data obtained from their simulations and compared these with maps of 65 clusters observed with the Einstein Imaging Proportional Counter. They were able to conclude that galaxy clusters with the observed range of X-ray morphologies are very unlikely in low Ω_0 cosmologies.

By creating mock CCD frames and using the Kaiser & Squires (1993) technique to reconstruct cluster surface mass over-densities as explained in Chapter 2, we investigated the feasibility of using gravitational lensing to constrain Ω_0 and λ_0. The layout is as follows. In Section 3.2 we describe the simulations of cluster formation. In Section 3.3 we recall how we generate a background distribution of galaxies, create CCD frames simulating their distortion due to the clusters, and analyse these distortions to produce maps of the cluster surface over-densities. In Section 3.4 we compare the reconstructions to the original clusters. In Section 3.5 we put this analysis on a more quantitative footing by introducing some statistics for measuring cluster shapes. In Section 3.6 we analyse the cluster from Chapter 2 in the same way. We conclude in Section 3.7 with a summary of our main results.

3.2   The Cluster Simulations

For our lenses, we used a set of eight N-body gas dynamic simulations of the formation of galaxy clusters. The clusters evolved from the same eight sets of initial density fields but in three different cosmologies. These cosmologies were:-

1. A biased Einstein-de Sitter model [$\Omega_0 = 1$, $\sigma_8 = 0.59$ (where $\sigma_8 = < (\frac{\delta\rho}{\rho})^2 >^{\frac{1}{2}}$ on an $8 \times \{100 \text{ kms}^{-1}\text{Mpc}^{-1}/H_0\}$ Mpc scale)]

2. An unbiased ($\sigma_8 = 1.0$) open model with $\Omega_0 = 0.2$ and $\lambda_0 = 0$

3. An unbiased model with $\Omega_0 = 0.2$ and $\lambda_0 = 0.8$

These three cosmologies will be referred to as the $\Omega_0 = 1$, $\Omega_0 = 0.2$ and $\Omega_0 + \lambda_0 = 1$ cases respectively.

In each of four periodic boxes of size $L = 30, 40, 50$ and 60 Mpc, Evrard et al. (1994) created two constrained realizations of Gaussian random density fields, with the standard cold dark matter power spectrum appropriate for $H_0 = 50$ km s^{-1} Mpc^{-1}. In each case, using the technique of Bertschinger (1987), they imposed the constraint that when smoothed with a Gaussian of $R_f = 0.2L$, there be a peak at the centre of the box with height 2.5–5 times the *rms* density fluctuation on this scale.

The P3MSPH (particle-particle, particle-mesh, smoothed particle hydrodynamics) algorithm (Evrard 1988) was used to evolve the particle distributions in time. Two sets of 32^3 particles represented the dark matter and baryons respectively. A

baryon content of $\Omega_b = 0.1$ was assumed for all the models. Gravity, PdV work and shock heating were incorporated for the baryons but the effects of radiative cooling were ignored. The spatial resolution was approximately $0.005L$, varying from 150 to 300 kpc depending on the box length.

3.3 Lensing Methods

3.3.1 The Cluster Masses

For our lensing simulations we chose the output epoch from each cosmology closest to redshift $z = 0.18$. This value was chosen to correspond to the cluster redshift in Chapter 2.

In the simulations of Evrard et al. (1994), for each given cosmology, the mass of each cluster was approximately proportional to the volume of the simulation box. Our aim was to study the morphology of clusters detected by gravitational lensing with similar signal-to-noise ratio in each cosmology. Thus, for our purposes it was more convenient to have a set of clusters all of the same mass. To achieve this we simply rescaled the mass of each particle in the smaller clusters so that the total mass was the same as the total mass in the largest cluster i.e. the $L = 60$ Mpc box. This involved multiplying each mass by the factor $(\frac{60\mathrm{Mpc}}{L})^3$. In order to maintain the correct density we also multiplied the simulation length by $\frac{60\mathrm{Mpc}}{L}$.

The typical mass of a rich cluster is known approximately from observations. Ideally, we would like all the clusters in our simulations to have approximately the same mass within some radius e.g. an Abell radius (3 Mpc). The simulated clusters in the $\Omega_0 = 0.2$ ($\lambda_0 = 0$) and $\Omega_0 + \lambda_0 = 1$ cosmologies were less massive so we scaled them as in the previous paragraph to have approximately the same total mass as the average $\Omega_0 = 1$ cluster (i.e. $\sim 2.72 \times 10^{15} M_\odot$ within an Abell radius).

After this rescaling the initial conditions were no longer appropriate for a standard CDM model but instead had power spectra with slightly different slopes. It turns out, however, that moderate changes in the spectral slope of the power spectrum are far less important in determining the formation history of a cluster than the cosmology (Lacey & Cole 1993), so this rescaling should have only negligible effect on our results.

Lensing is sensitive only to the cumulative mass along any chosen line of sight. We therefore tripled the size of our cluster sample by choosing three perpendicular axes through the centre of each cluster and considering the total projected mass along each line of sight independently, as a different cluster. This resulted in 72 cluster simulations, 24 from each of the three cosmologies.

3.3.2 CCD images

We employed our "default" distributions of galaxy ellipticity, scale length, redshift, magnitude, noise and seeing from Chapter 2, Section 2.4.1; namely, an empirical ellipticity distribution from a deep CCD exposure (Brainerd et al. 1996), an empirical scale length distribution from Tyson (1996), an empirical magnitude distribution from Metcalfe et al. (1995), and a redshift distribution from the simulations of Cole et al. (1994). The value of the noise was chosen to mimic detections of galaxies down to $m_B = 26.5$. The seeing was 1 arcsecond.

We created one CCD frame per cluster and then analysed it using FOCAS as before. As described in section 2.5.1, a magnitude cut, $m_{cut} = 25.5$, suggested by the Kolmogorov-Smirnoff test, and an ellipticity cut of $e_{cut} = 0.5$ were used to define the galaxy sample that was analysed.

3.4   Views of the Clusters

At the end of the chapter, we show the projected surface densities of the central regions of the clusters. On each page are shown the three orientations of each cluster. The left panels have been smoothed with a Gaussian of $\theta_{sm} = 0.25$ arcminutes which is the same smoothing as used in the Kaiser and Squires reconstruction. The resulting surface densities are expressed in terms of S_{crit} where, for our redshift distribution, $S_{crit} \simeq 3 \times 10^{15} M_\odot / \mathrm{Mpc}^2$, the exact value depending on the cosmology. The greyscale shows the surface overdensity with high overdensity being represented by dark colouring. The right panels show the corresponding reconstruction. The contour encloses the 150 pixels of highest overdensity. The field of view is ~ 2.5 Mpc.

It should be noted that the greyscale range of the panels on the left is not the same as the scale for those on the right. The reconstructed surface densities are always diminished when compared to the original. This is partly due to observational effects such as seeing and noise, and partly due to the effects of nonlinearity - weak lensing techniques generally begin to fail when the surface density rises above a few tenths of critical. It is therefore necessary to show the clusters using different greyscales, as detailed below, for the substructure of the reconstructions to be clearly visible. Note that the surface densities on the left hand side have been normalised, such that the mean value is zero. This is to allow for the fact that the mean value from the KS reconstruction is zero.

The clusters from the $\Omega_0 = 1$ cosmology are obviously in the process of forming. In many cases clumps of matter may be seen falling towards the centre. Even when the cluster consists of only one aggregation of matter, it is very often elongated in shape rather than spherical. The left panel greyscale depicts a range of surface overdensity from $\hat{\sigma}$ of -0.1 to 0.35, the right $\hat{\sigma}$ of -0.1 to 0.25. Note that the general shapes of the reconstructed clusters, with the exception of some noisy pixels, are

very similar to the originals.

The clusters from the $\Omega_0 = 0.2$, $\lambda_0 = 0$ cosmology are much more spherically symmetric and centrally concentrated than those from the $\Omega_0 = 1$ case. This time the left panel greyscale depicts a range of surface overdensity from $\hat{\sigma}$ of -0.1 to 0.7. The right panel greyscale is unchanged i.e. from -0.1 to 0.25. Note that the left hand panels appear uniformly black near the centre. Limitations of scale conceal the reality that the density distribution is in fact very highly peaked. The maximum surface density can be critical or even greater. In contrast, the maximum surface overdensity in the right hand panels is $\simeq 0.2$ or 0.3 of critical and systematically underestimates the density in the regime where the overdensity is ≥ 0.2 of critical. This failure of the KS technique results in the reconstruction profiles being very flat near the cluster centre. All overdensities higher than ~ 0.2 are assigned approximately the same value. This results in a broad plateau around the central region with many hundreds of pixels being assigned approximately the same value. The value of each of the central pixels is, of course, subject to small fluctuations about this value because of the random influence of noise. The 150 highest value pixels may not reflect accurately the true shape of the region of highest overdensity. Closer inspection of the reconstructions reveals that if one chooses a larger area, corresponding to 200–300 pixels, which extends beyond this plateau, then its shape more closely matches the original.

The clusters from the $\Omega_0 + \lambda_0 = 1$ cosmology are again very spherically symmetric and centrally concentrated. Here, the left panel greyscale depicts a range of surface overdensity from $\hat{\sigma}$ of -0.1 to 0.5 and the right panel greyscale is unchanged. The clusters in this case are a little more elongated and have slightly lower central surface over-densities than the $\Omega_0 = 0.2, \lambda_0 = 0$ case. In general the reconstructed shapes match the originals well.

Qualitatively, the reconstructions appear to preserve the essential features of the different cluster morphologies quite well. In the next section we suggest a set of statistics which enable us to make the comparisons quantitative.

3.5   The Statistics

As we have discussed in the Introduction and Chapter 2, lensing analyses such as KS, although very reliable for finding the *relative* values of surface overdensity $\hat{\sigma}(\vec{\theta})$ (equation 2.7), are subject to uncertainties in the *absolute* value of surface overdensity. We therefore decided to use the following two dipole- and quadrupole-like statistics, D and Q, to quantify cluster morphology, specifically chosen to be independent of the mean value of surface density $\frac{\bar{S}}{S_{\text{crit}}}$ (see Section 2.2).

$$D = \frac{|d|}{A^{\frac{3}{2}}}$$

where

$$d_1 = \int H(\hat{\sigma} - \sigma_{\text{con}})x\, dA$$

$$d_2 = \int H(\hat{\sigma} - \sigma_{\text{con}})y\, dA$$

$$|d| = [d_1^2 + d_2^2]^{\frac{1}{2}}$$

$$A = \int H(\hat{\sigma} - \sigma_{\text{con}})\, dA$$

and H is the Heaviside step function,

$$H(\hat{\sigma} - \sigma_{con}) = 0, \hat{\sigma} < \sigma_{\text{con}}$$

$$= 1, \hat{\sigma} \geq \sigma_{\text{con}}$$

σ_{con} is the surface overdensity of the contour level above which we choose to evaluate the statistic and A is the area within that contour.

Analogously,

$$Q = \frac{|q|}{A^2}$$

where

$$q_1 = \int H(\hat{\sigma} - \sigma_{\text{con}})(x^2 - y^2)\, dA$$

$$q_2 = \int H(\hat{\sigma} - \sigma_{\text{con}})2xy\, dA$$

$$|q| = [q_1^2 + q_2^2]^{\frac{1}{2}}$$

$$A = \int H(\hat{\sigma} - \sigma_{\text{con}})\, dA$$

Note that both of the above statistics are dimensionless. The statistics are not intended to be unique - any combination of first moments for D and second moments for Q would be equally good. In practice, the integrals become sums over pixels. Note also that the integrals are not weighted by surface overdensity.

Once we have chosen a suitable size of fixed area A, say 100 pixels, over which to evaluate the statistics, the corresponding value of σ_{con} enclosing that area is fixed. We evaluate the integrals over the same area for all the clusters. Because the two statistics, D and Q, are dependent only upon this chosen area, they too are independent of any inherent uncertainties in the estimated values of surface overdensity. That is to say, the statistics are independent of:-

1. Any dilution of the lensing signal due to seeing.

2. Nonlinearity effects causing the surface overdensity to be underestimated in regions of high surface overdensity.

3. The actual (unknown) value of σ_{crit}.

In what follows we will use two definitions of the cluster centre, firstly the most dense pixel and secondly the point at which $D = 0$. We begin by evaluating the statistics using the pixel with maximum surface density as centre.

In Figures 3.1 and 3.2 the statistics are evaluated for the highest 100 and 200 pixels. The pixel-size used in the KS reconstructions is about a fifth of a square arcminute or 0.04 Mpc^2.

In Figure 3.1 the top panel shows the estimated probability that a cluster will have a dipole greater than the abscissa value for each of the three cosmologies. The solid lines are for $\Omega_0 = 1$, the dotted lines $\Omega_0 = 0.2$, and the dashed lines $\Omega_0 + \lambda_0 = 1$. In each case, the line marked by triangles, usually with the smaller dipole value, is from the original, smoothed but unlensed clusters. Examining the original clusters first, it is apparent that an $\Omega_0 = 0.2$ universe has clusters with smallest dipoles, followed by an $\Omega_0 + \lambda_0 = 1$ universe, and finally $\Omega_0 = 1$. After lensing the dipole value becomes larger in all cases. This is partly due to noise in the reconstructions i.e. rogue outlying pixels increasing the dipole. The noise can also displace the cluster centre. This is particularly apparent in the $\Omega_0 = 0.2$ case. Because the reconstruction is so flat in the centre, an off-centre pixel can easily appear to have the highest surface density. This can obviously increase the overall dipole value dramatically and explains why the reconstructed $\Omega_0 = 0.2$ and $\Omega_0 = 1$ lines almost coincide. The effect is less marked for $\Omega_0 + \lambda_0 = 1$ and it always has a smaller dipole.

The lower panel shows the estimated probability that a cluster will have a quadrupole, Q, greater than the abscissa value when the statistic is evaluated within the 100 highest pixels. Again, the original $\Omega_0 = 0.2$, $\Omega_0 + \lambda_0 = 1$ and $\Omega_0 = 1$ models, in that order, have increasing quadrupole value. Once again the reconstructed $\Omega_0 + \lambda_0 = 1$ clusters have noticeably lower quadrupoles than the other cases. The suggestion is that the "plateau problem", as for the dipole, also affects the $\Omega_0 = 0.2$ quadrupole. There is also the concern that 100 pixels may be too small an area over which to evaluate the statistic. In Figure 3.2, therefore, we show the equivalent plots where the statistic has been evaluated over the highest 200 pixels.

In Figure 3.2 the dipole values are very similar to those in Figure 3.1. The main difference is in the quadrupole values. Here, the $\Omega_0 = 0.2$ and $\Omega_0 + \lambda_0 = 1$ cases clearly have smaller quadrupole after lensing than the $\Omega_0 = 1$ case. The quadrupole value for $\Omega_0 = 1.0$ has also increased relative to Figure 3.1. This is probably due to the fact that the larger area of 200 pixels can contain more elongated objects. Note that in plots similar to the right hand panels of the cluster views, but using 200 pixels as the contour level, it is apparent that some outlying noisy pixels are being included in the analysis.

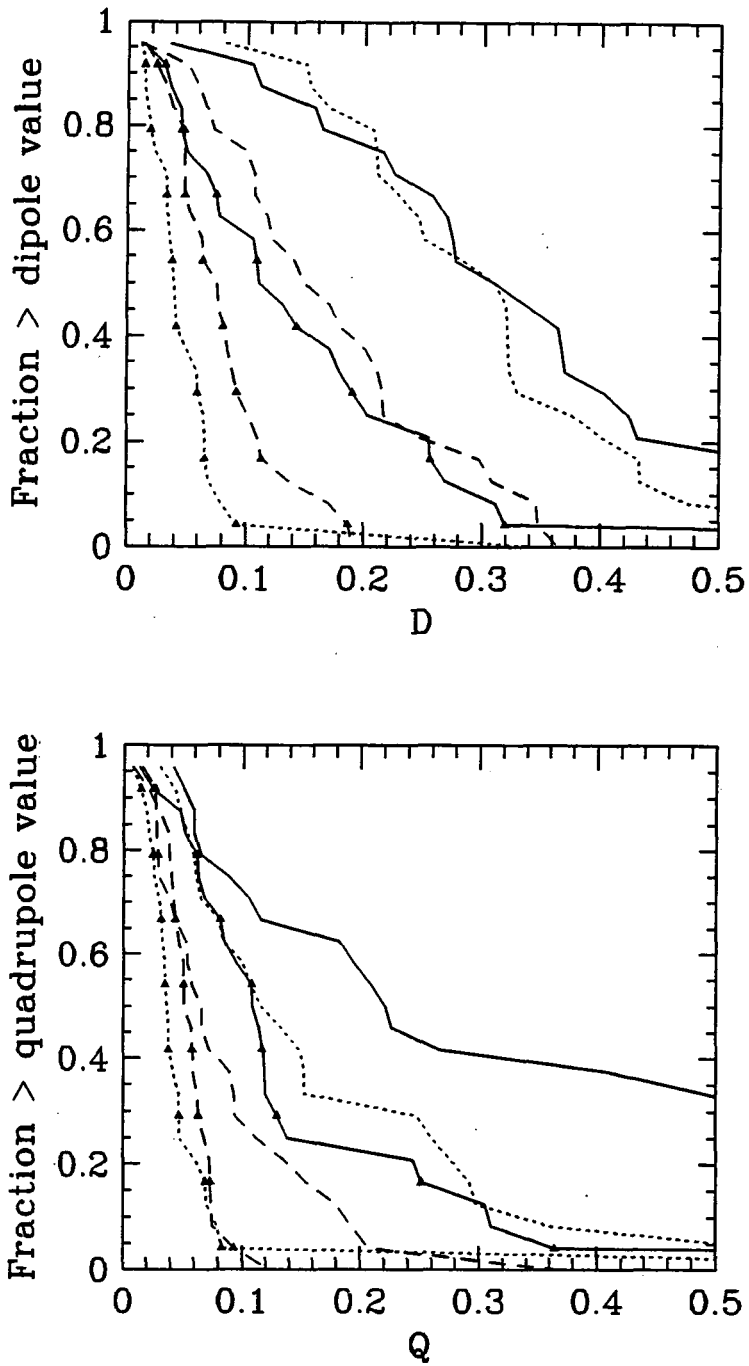The above results suggests that the dipole is unlikely to be a very useful statistic

Figure 3.1: The top panel shows the probability that a cluster will have a dipole D greater than the abscissa value. The solid lines are for $\Omega_0 = 1$, the dotted lines $\Omega_0 = 0.2$, and the dashed lines $\Omega_0 + \lambda_0 = 1$. In each case the line marked by triangles is from the original, unlensed clusters. The lower panel shows the probability that a cluster will have a quadrupole Q greater than the abscissa value. The 100 highest surface density pixels have been used. See text for details.
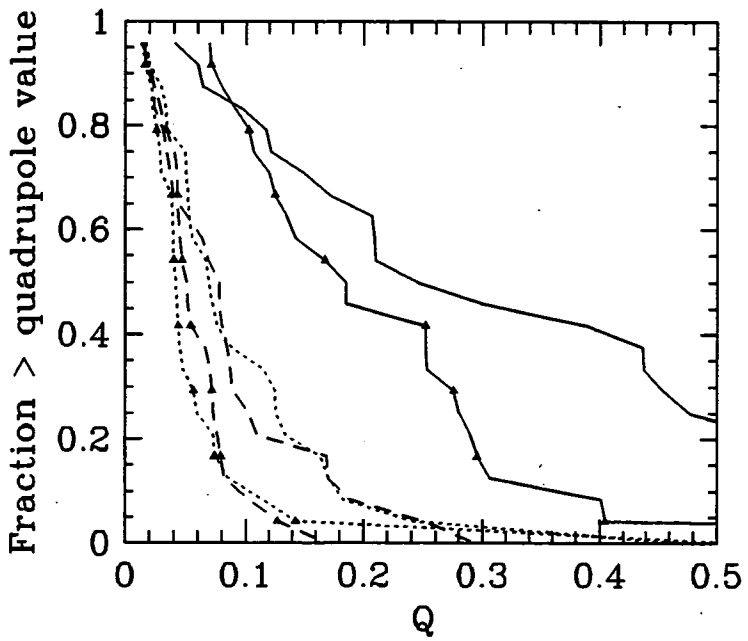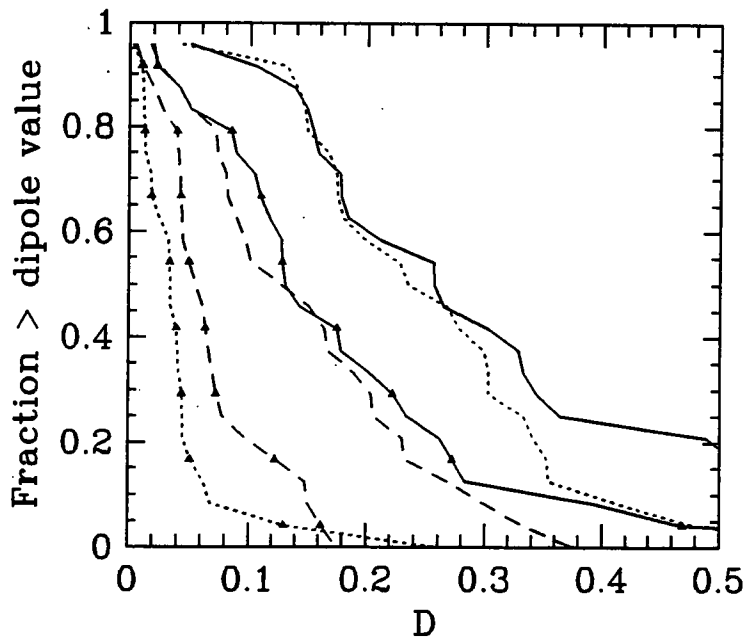
Figure 3.2: As for Figure 3.1. In this case, the 200 highest surface density pixels have been used. See text for details.
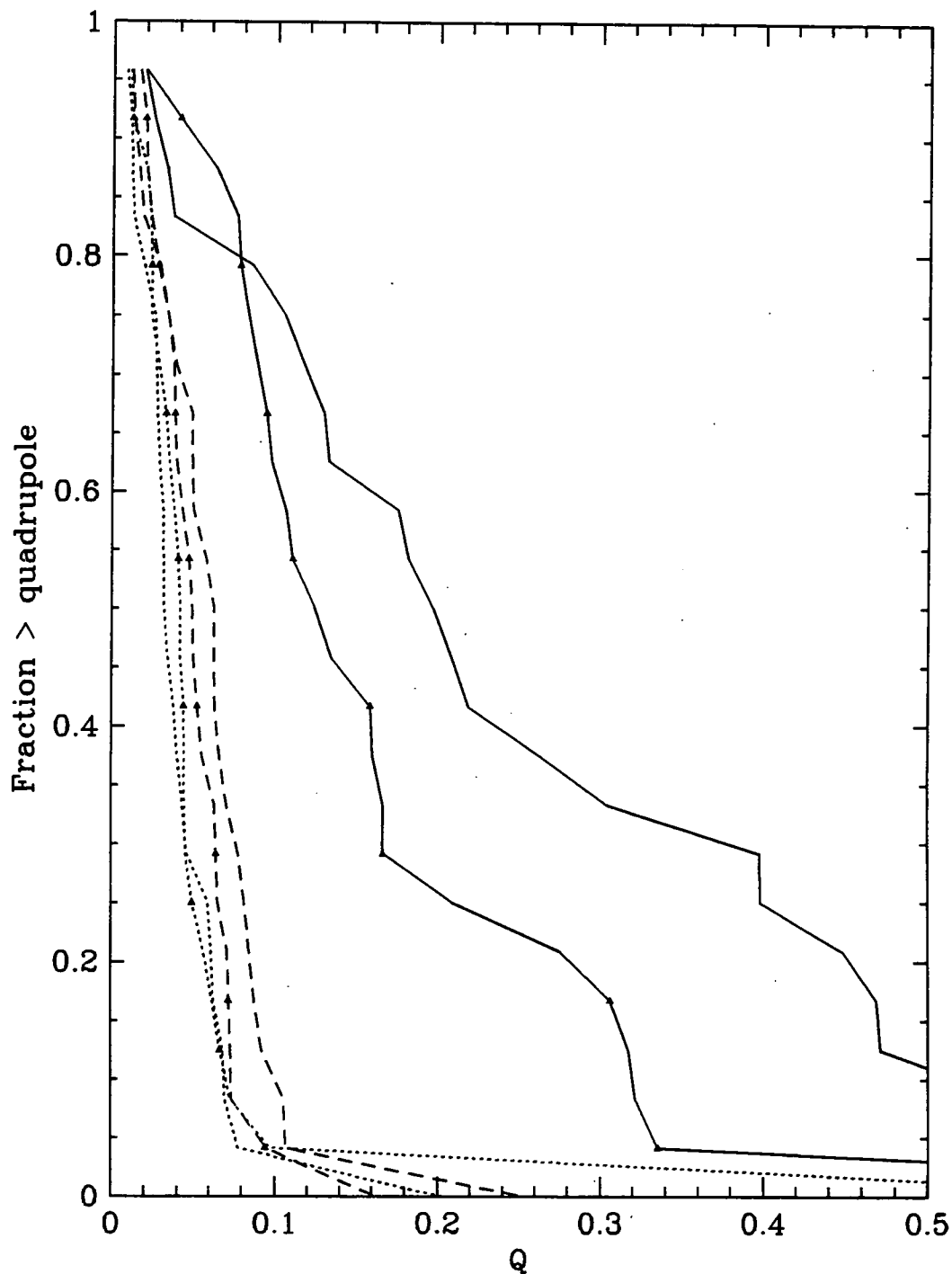
Figure 3.3: The lines show the probability that a cluster will have a quadrupole Q greater than the abscissa value. Here, the dipole D has been used to define the cluster centre. The solid lines are for $\Omega_0 = 1$, the dotted lines $\Omega_0 = 0.2$, and the dashed lines $\Omega_0 + \lambda_0 = 1$. In each case the line marked by triangles shows the original, unlensed clusters. The 150 highest surface density pixels have been used. See text for details.
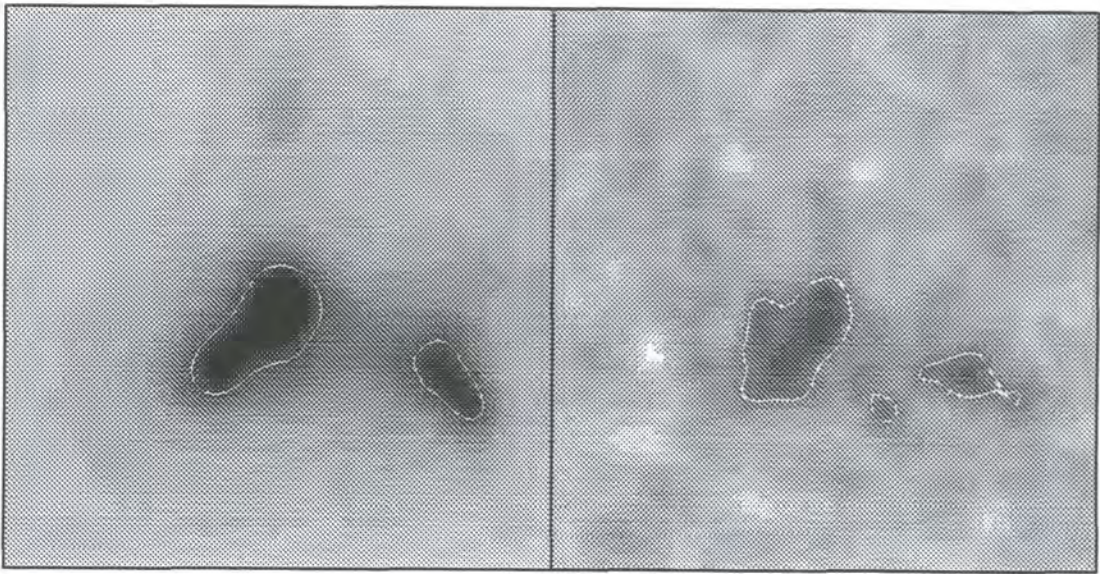
Figure 3.4: The left panel shows the cluster from Chapter 2. The right panel shows the reconstruction of the same cluster. The grey scale ranges from -0.1 to 0.25 $\hat{\sigma}$ in each case. The contour encloses the highest 150 pixels.

for characterising cluster morphology unless the signal-to-noise of the reconstruction is very high. In the light of this we tried a second choice of cluster centre which is more robust than simply selecting the densest pixel. We decided to use the point at which the dipole is zero as centre, and calculate the quadrupole relative to this point. In addition, we decided to evaluate this statistic at a compromise area of 150 pixels. We are less interested in optimising the area over which we evaluate the statistic, than in demonstrating that the method is sound for a sensible choice of area.

Figure 3.3 shows the resulting quadrupole evaluated in this way. All the values are reduced compared to the bottom panel in Figure 3.2. The most marked reduction is to the lensed clusters from $\Omega_0 = 0.2$, confirming that minimising the dipole is a more reliable measure of the true centre.

It would appear, therefore, that providing the cluster simulations are reasonably accurate representations of actual rich clusters expected to form in these different cosmologies, there is considerable hope for using gravitational lensing as a tool for cosmological model discrimination. For example, from Figure 3.3 we can see that 60% of clusters in an $\Omega_0 = 1$ universe have a Q value in excess of 0.1. Conversely, only about 5% of clusters in an $\Omega_0 = 0.2$ universe are so aspherical. It is unlikely that $\Omega_0 = 0.2$ and $\Omega_0 + \lambda_0 = 1$ clusters could be distinguished in this way, but, given even a small sample of clusters, it should be possible to put a very interesting constraint on Ω_0.

3.6   Comparison with Chapter 2 Cluster

For interest we compare the mass and shape of the $\Omega_0 = 1$ cluster from Chapter 2 to the above results. This cluster has a mass of $2.06 \times 10^{15} M_\odot$ within an Abell radius. This is of the same order as the mean mass of the 24 $\Omega_0 = 1$ clusters i.e. $2.72 \times 10^{15} M_\odot$.

Figure 3.4 shows the smoothed original cluster on the left and its reconstruction on the right. The greyscale ranges from -0.1 to 0.25 $\hat{\sigma}$ in both cases.

The quadrupole value, evaluated for the highest 150 pixels, is 0.6027, using minimised dipole as centre . For the reconstruction, the corresponding value is 0.3952. From Figure 3.3 we see that we would expect only a small fraction, $\sim 10\%$ of $\Omega_0 = 1$ clusters to have such a large quadrupole.

3.7   Conclusions

• We have examined 72 simulated clusters, 24 from each of three cosmologies. The greyscale views confirm that the clusters formed in $\Omega_0 = 0.2$ and $\Omega_0 + \lambda_0 = 1$

cosmologies are more regular than those formed in $\Omega_0 = 1$ cosmologies.

- We have simulated the gravitational lensing of background galaxies by these clusters. We used the resulting galaxy distortions to reconstruct the mass surface overdensity for each cluster. We find that although the mass overdensity is always diminished relative to the original, the general shape of the reconstructed mass distribution is usually in excellent agreement with the original.

- To quantify our discussion we have introduced new statistics, D and Q which essentially measure the cluster dipole and quadrupole. These are designed to minimise the influence of the systematic uncertainties inherent in the density field reconstructed from weak lensing observations. The intrinsic distributions of D and Q are very sensitive to Ω_0 but only weakly dependent on λ_0.

- The noise present in realistic constructions of these density fields from weak lensing data adds to the measured D and Q, but the Q distribution for $\Omega_0 = 0.2$ and $\Omega_0 = 1$ remain clearly distinguishable. Thus it will be necessary to model the observing conditions but it will still be possible to constrain Ω_0. We showed in Figure 3.3 that, given a sufficiently large sample of clusters, it should be relatively easy to distinguish between a low Ω_0 universe and a critical Ω_0 universe using only weak lensing techniques. The difference between the quadrupoles values from $\Omega_0 = 0.2$ and $\Omega_0 + \lambda_0 = 1$ clusters is much smaller and it would probably be impossible to distinguish between them using cluster shape information alone. Of course, the Universe may turn out to have a value of Ω_0 somewhere between the observers' preferred value of 0.2 and the theorists' preferred value of 1.0 but gravitational lensing studies of the shapes of rich galaxy clusters offers the hope, at least, of narrowing the likely range of Ω_0.
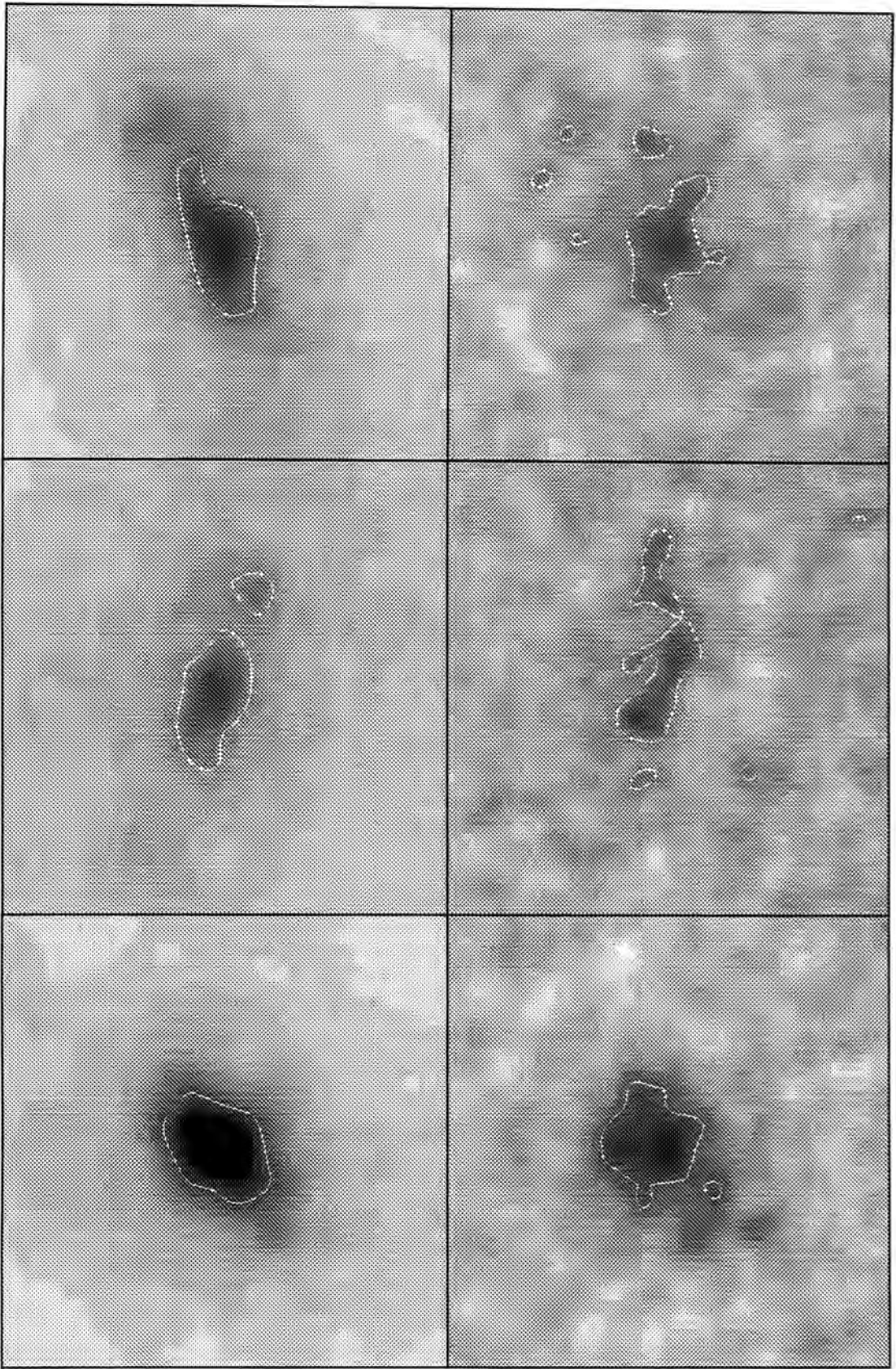
Figures 3.5 to 3.12 show the projected surface densities of the central regions of the clusters evolved in an $\Omega_0 = 1$ universe. On each page are shown the three orientations of each cluster. The left panels have been smoothed with a Gaussian of $\theta_{sm} = 0.25$ arcminutes which is the same smoothing as used in the Kaiser and Squires reconstruction. Their resulting surface overdensities are in terms of S_{crit}. The greyscale represents the surface overdensity with high overdensity being represented by dark colouring and ranges from $\hat{\sigma}$ of -0.1 to 0.35. The right panels show the corresponding reconstruction with greyscale ranging from -0.1 to 0.25. The contour encloses the 150 pixels of highest overdensity.
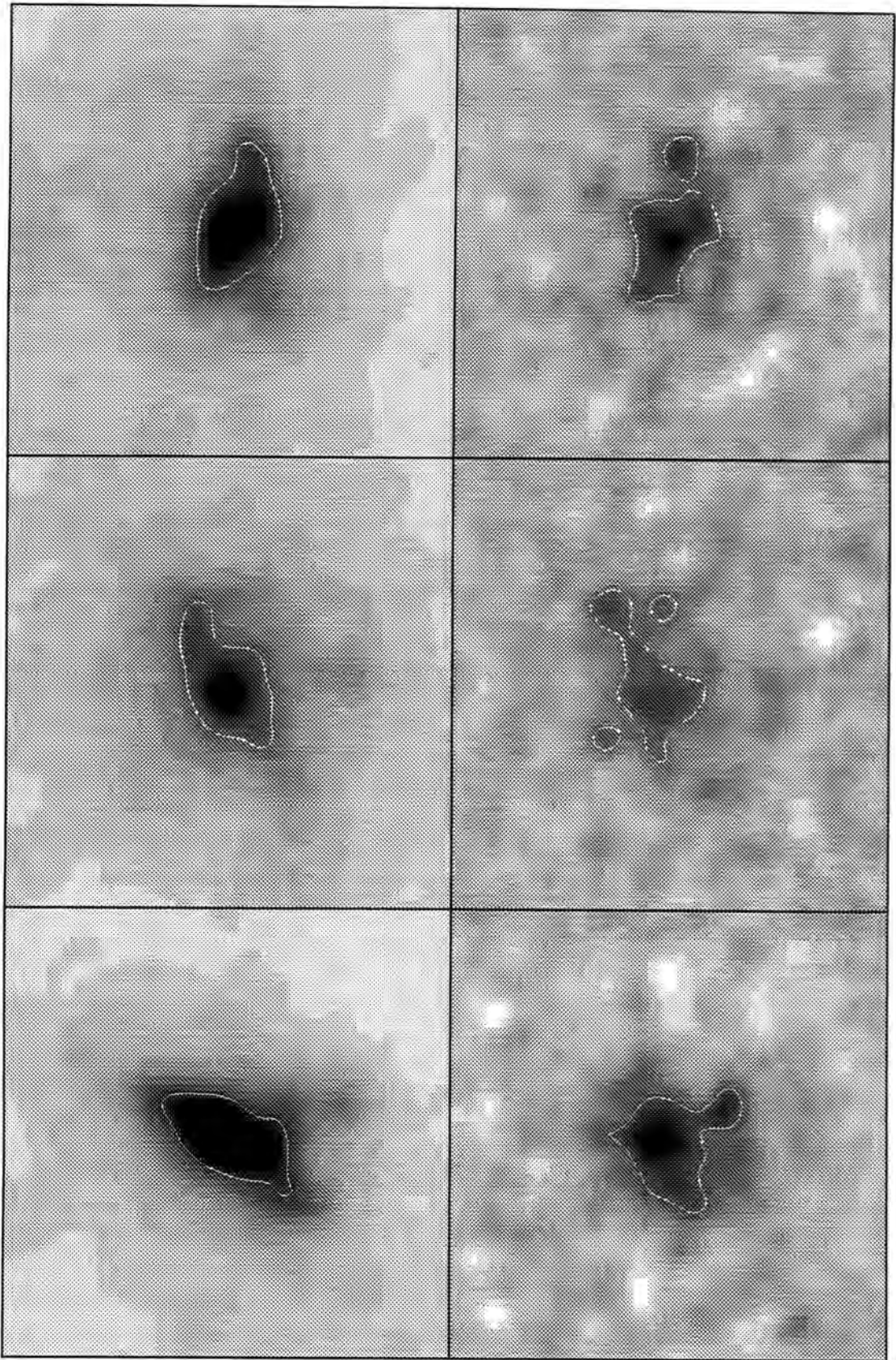
Figure 3.5:
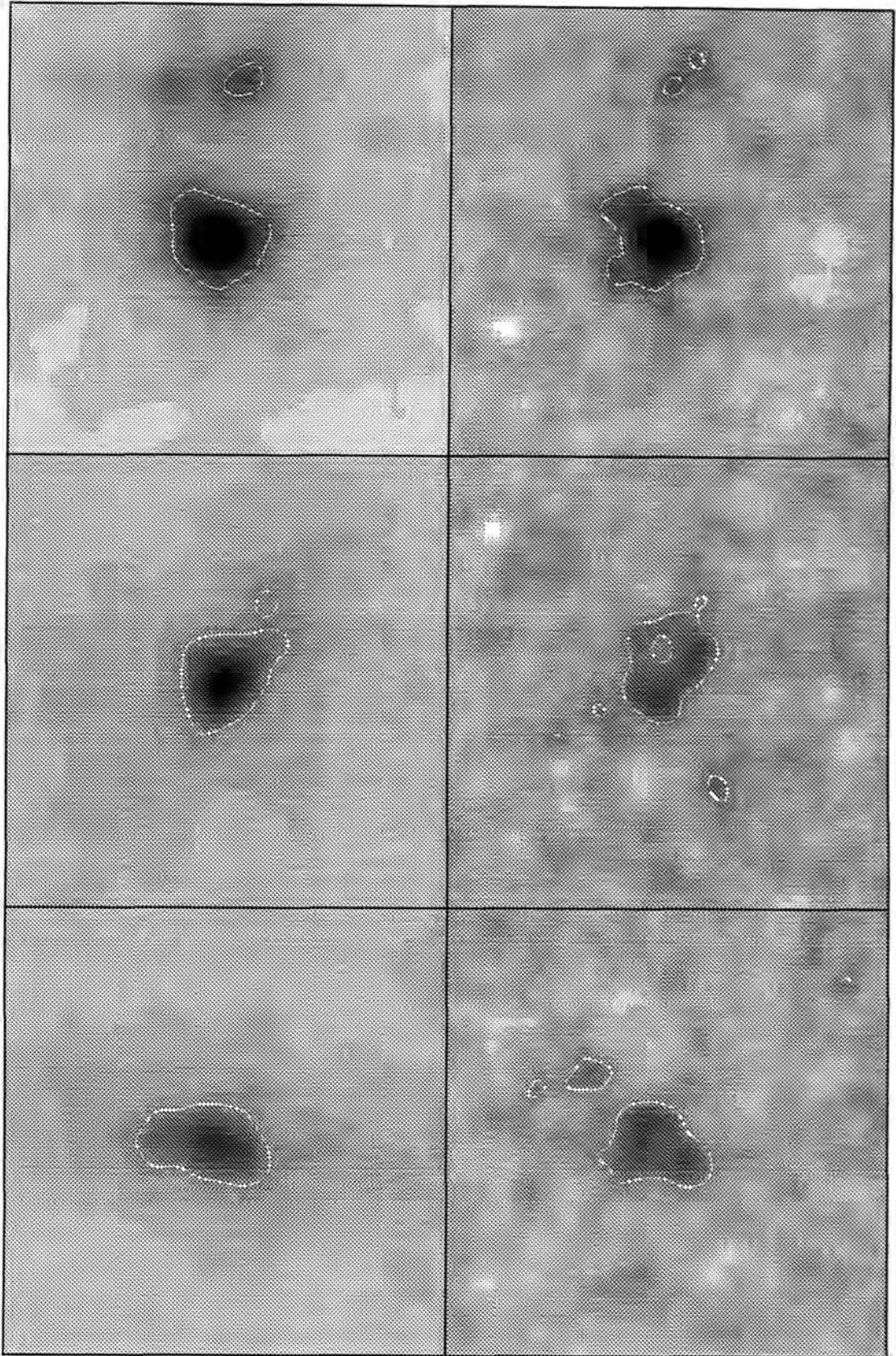
Figure 3.6:
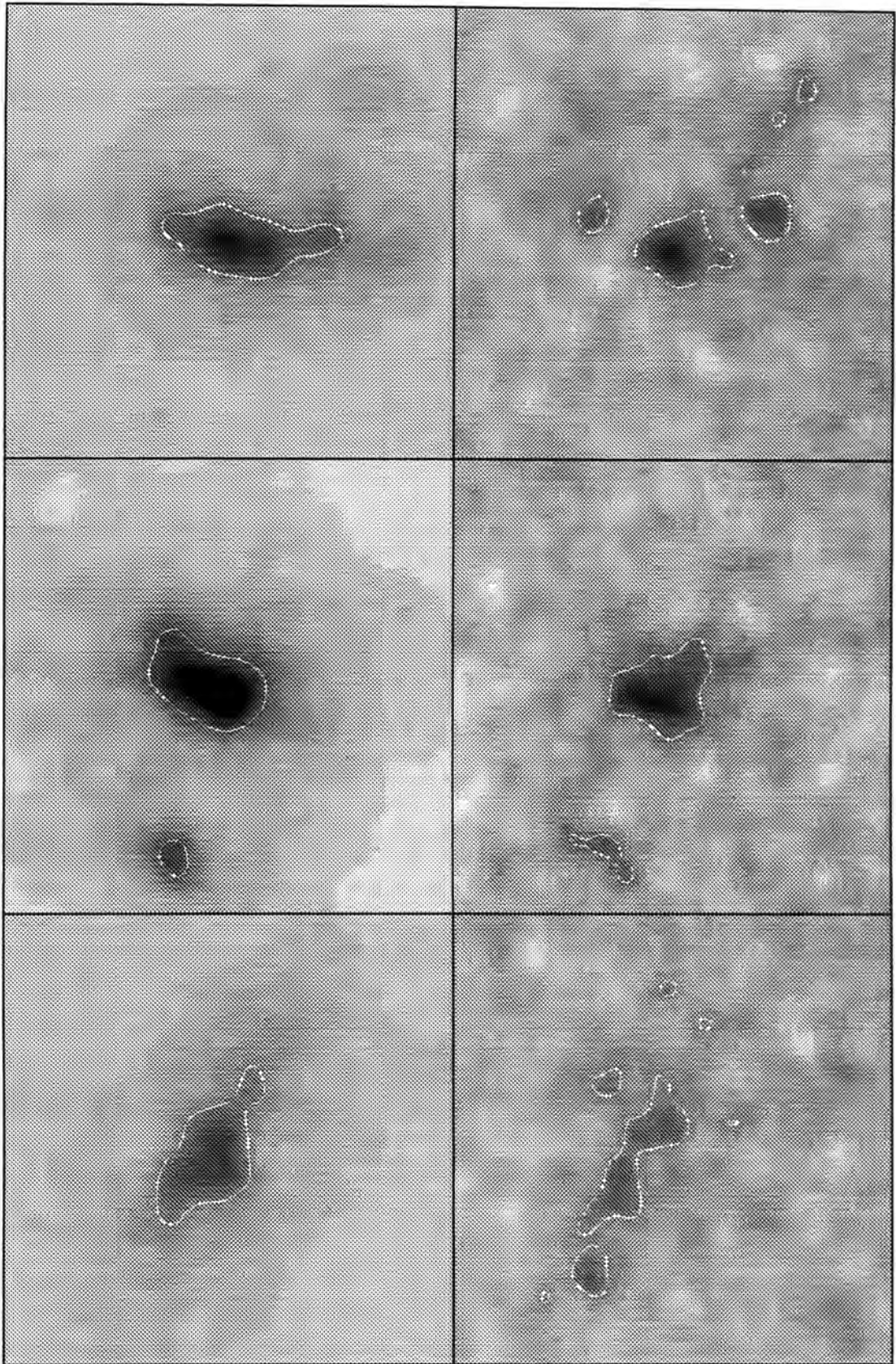
Figure 3.7:

Figure 3.8:

56
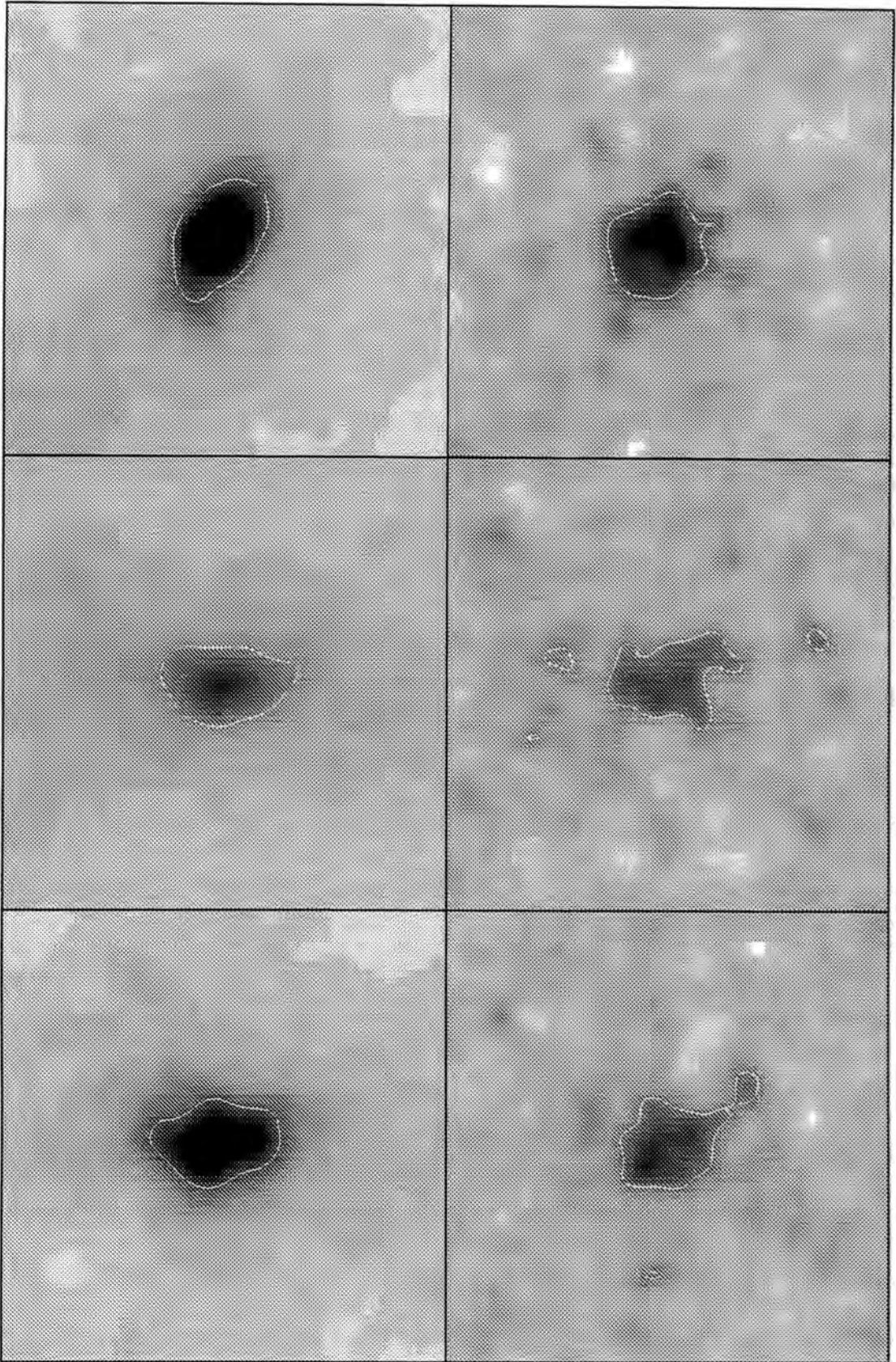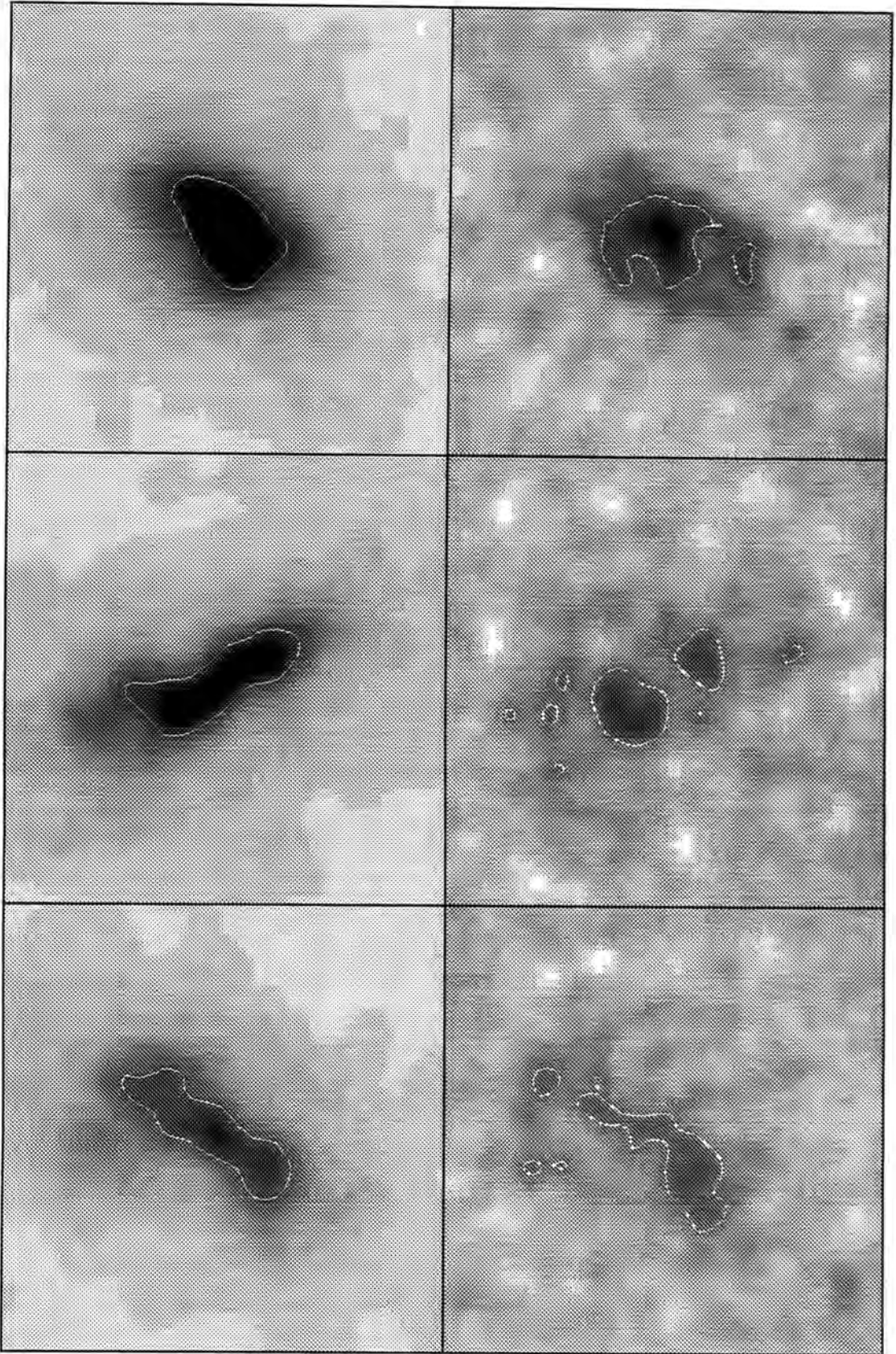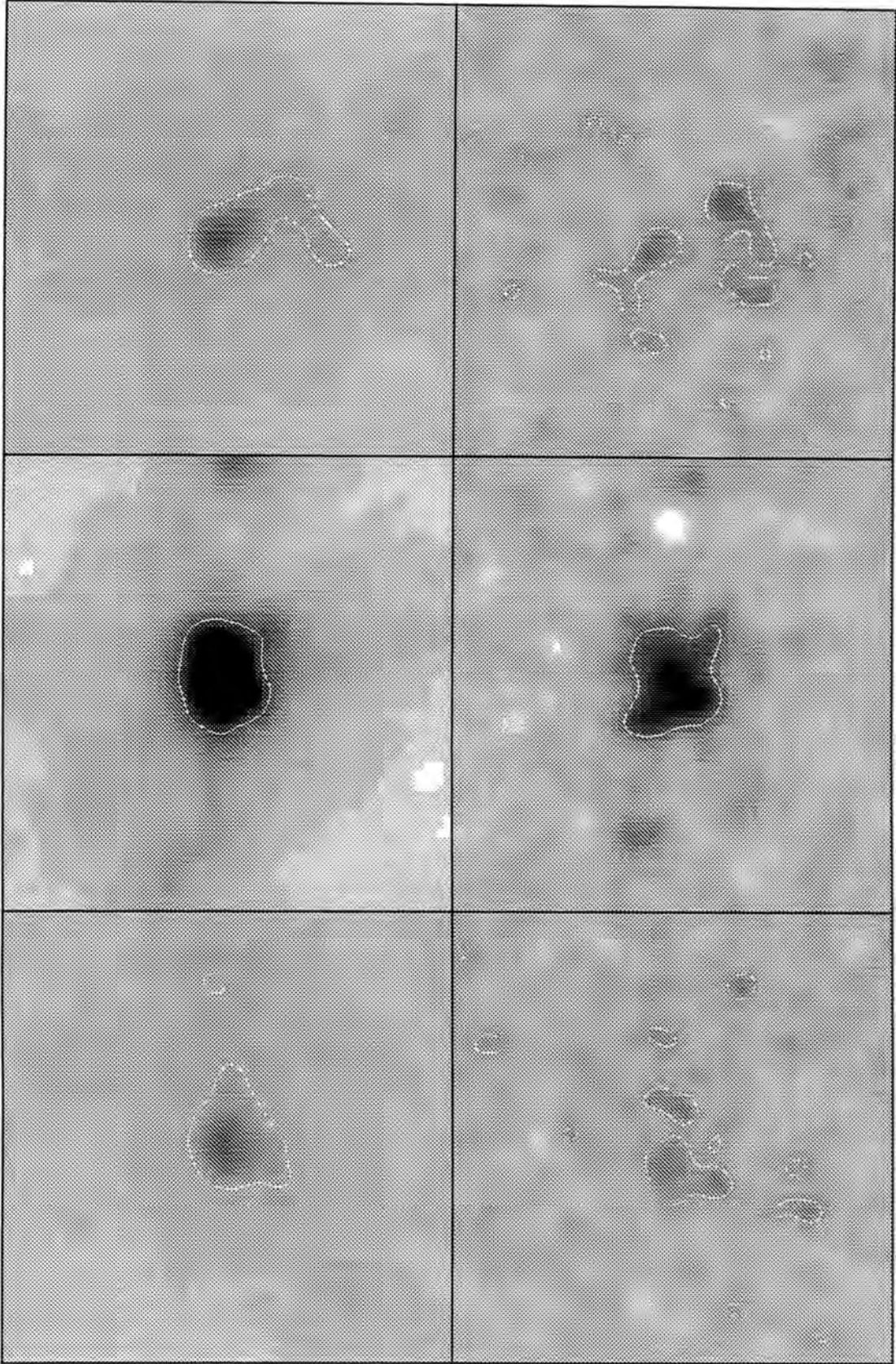
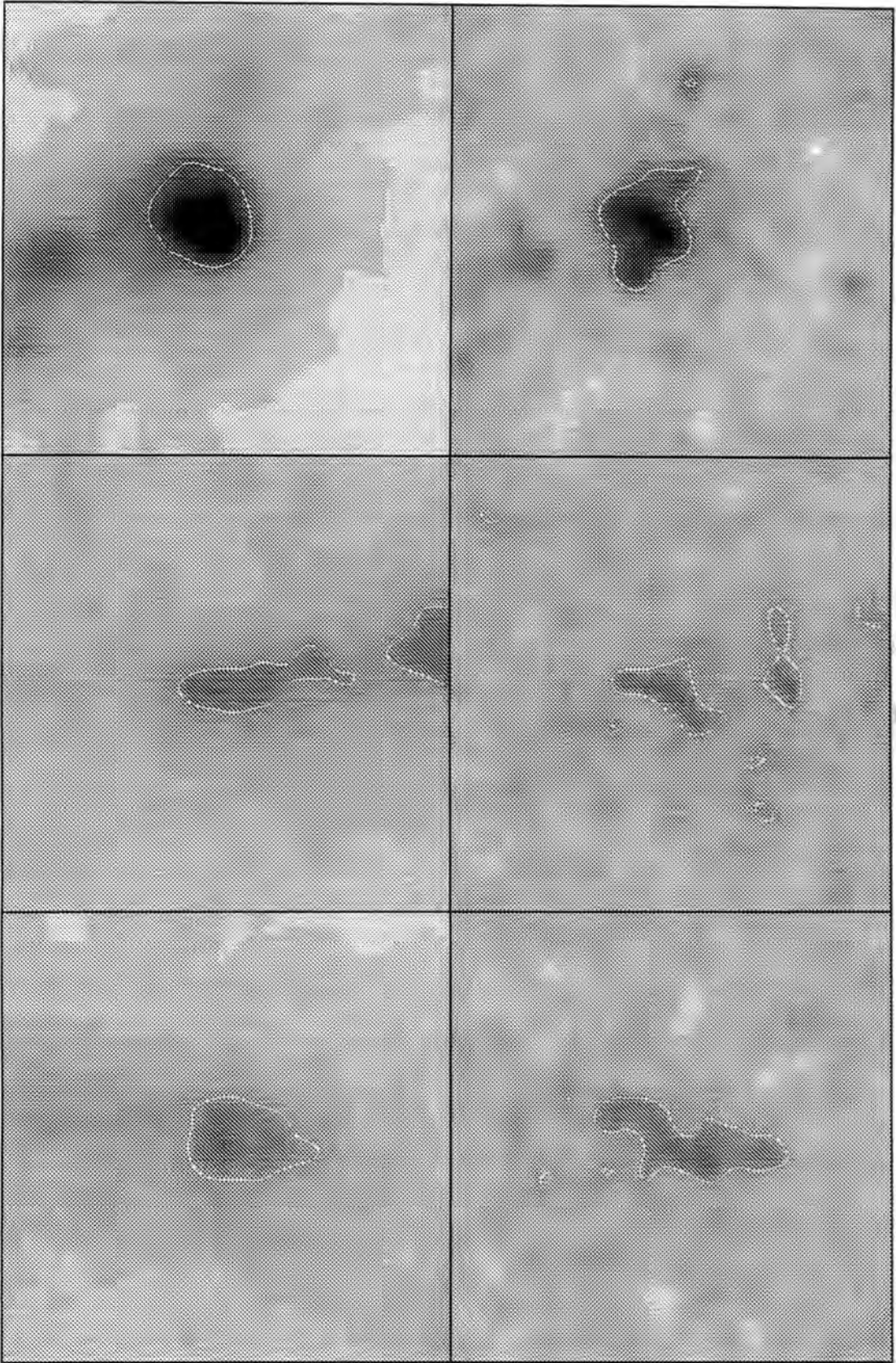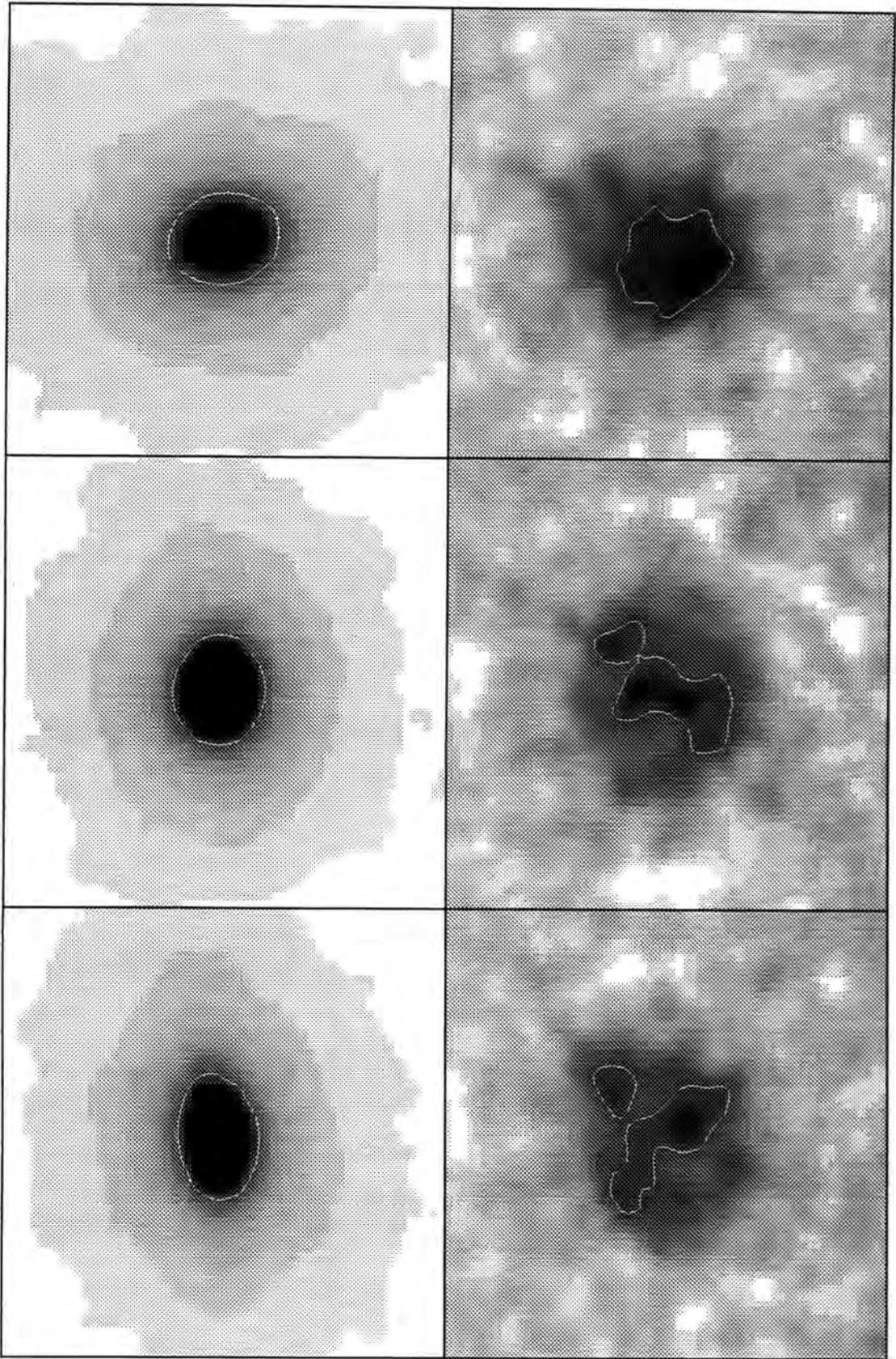Figure 3.9:

Figure 3.10:

Figure 3.11:

Figure 3.12:

Figures 3.13 to 3.20 show the projected surface densities of the central regions of the clusters evolved in an $\Omega_0 = 0.2$ universe. On each page are shown the three orientations of each cluster. The left panels have been smoothed with a Gaussian of $\theta_{sm} = 0.25$ arcminutes which is the same smoothing as used in the Kaiser and Squires reconstruction. Their resulting surface overdensities are in terms of S_{crit}. The greyscale represents the surface overdensity with high overdensity being represented by dark colouring and ranges from $\hat{\sigma}$ of -0.1 to 0.7. The right panels show the corresponding reconstruction with greyscale ranging from -0.1 to 0.25. The contour encloses the 150 pixels of highest overdensity.
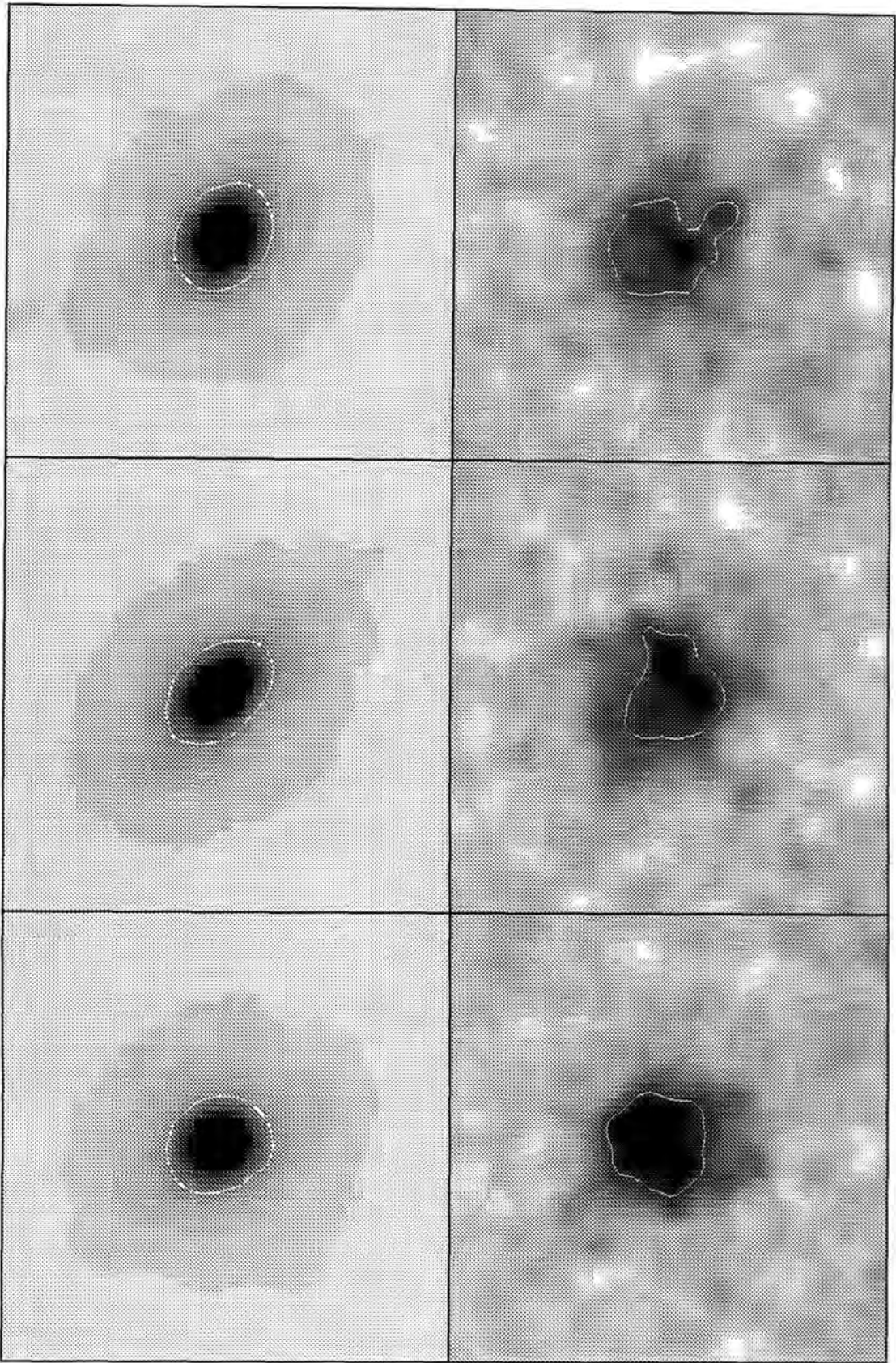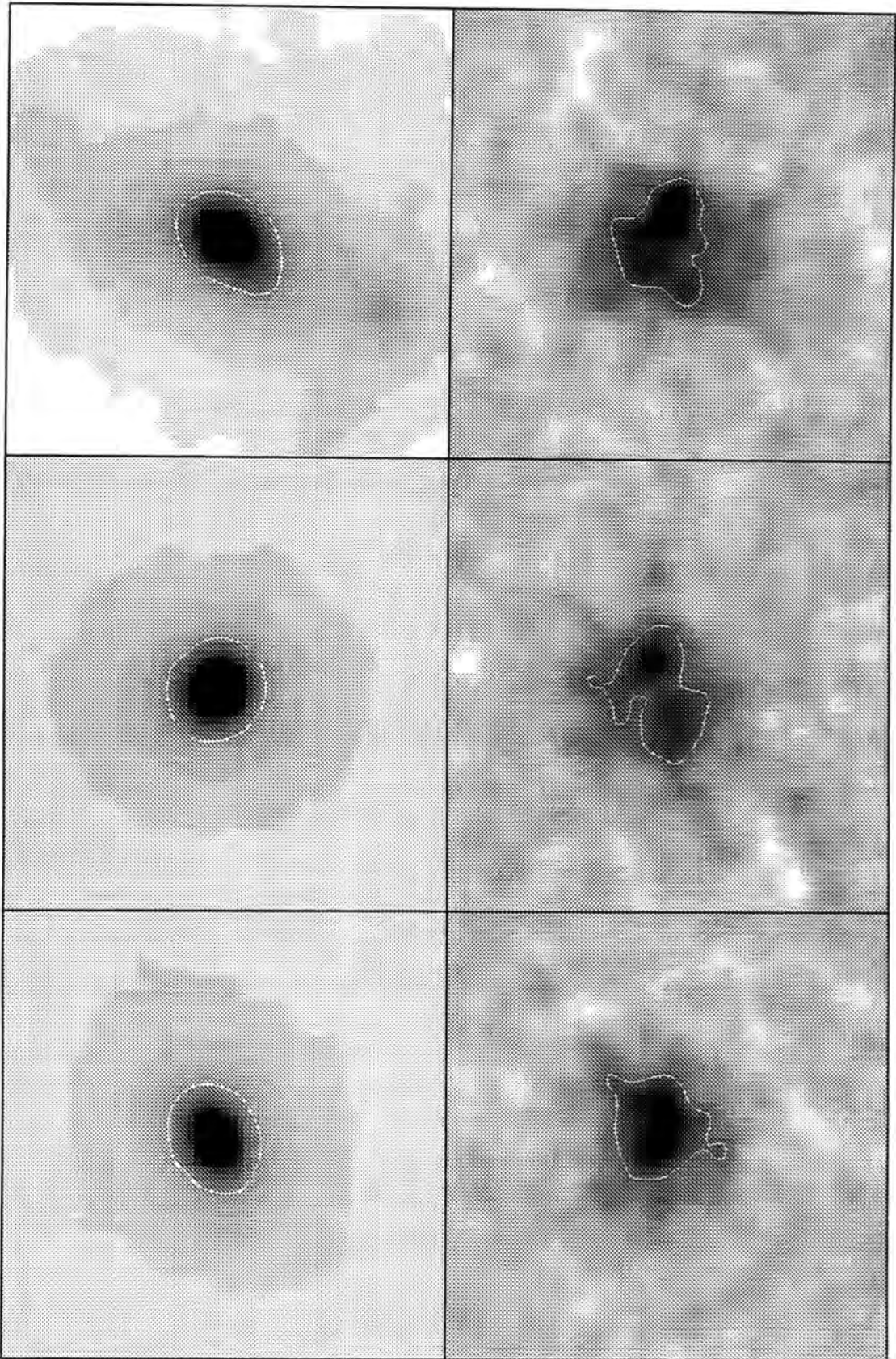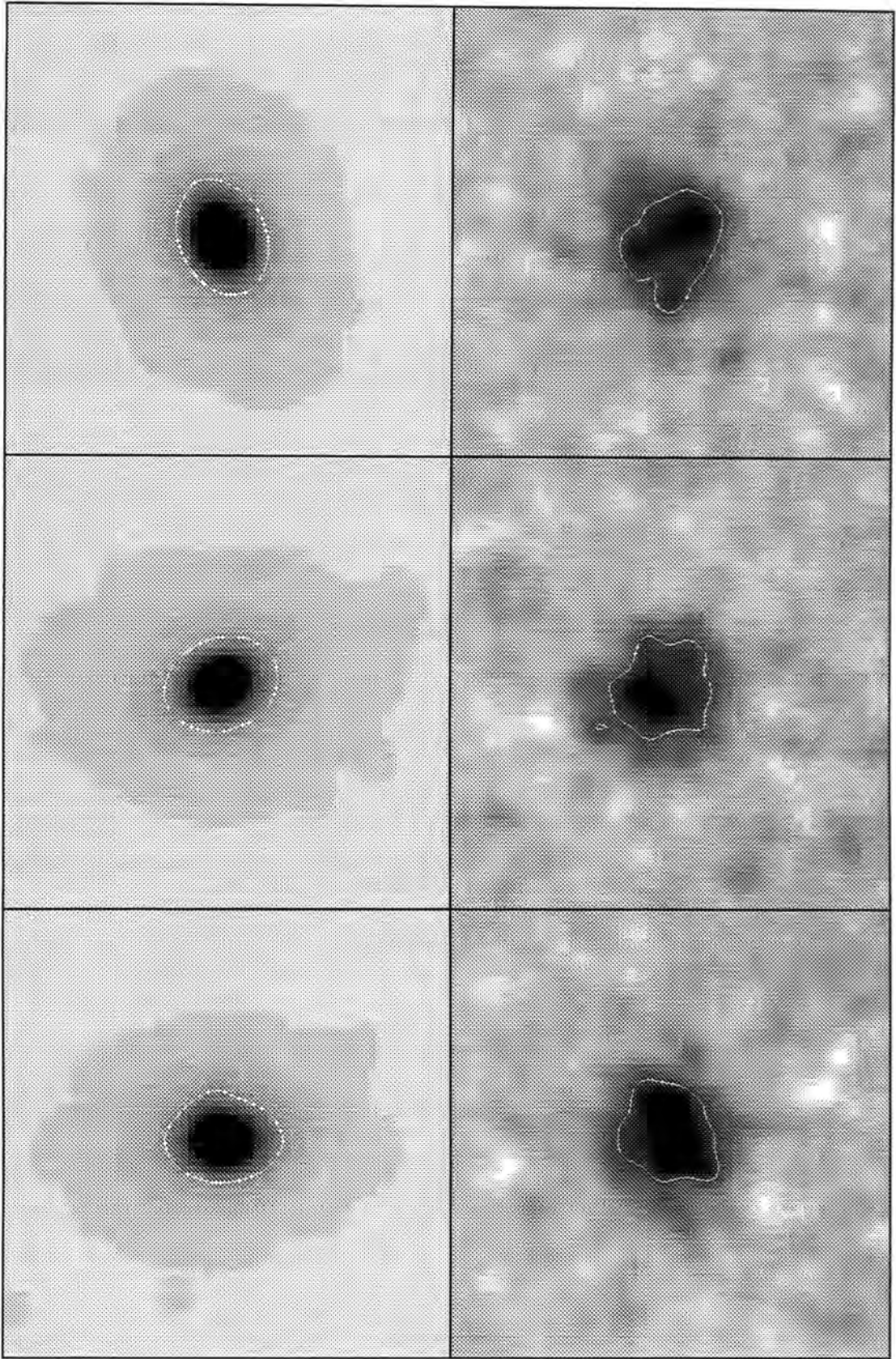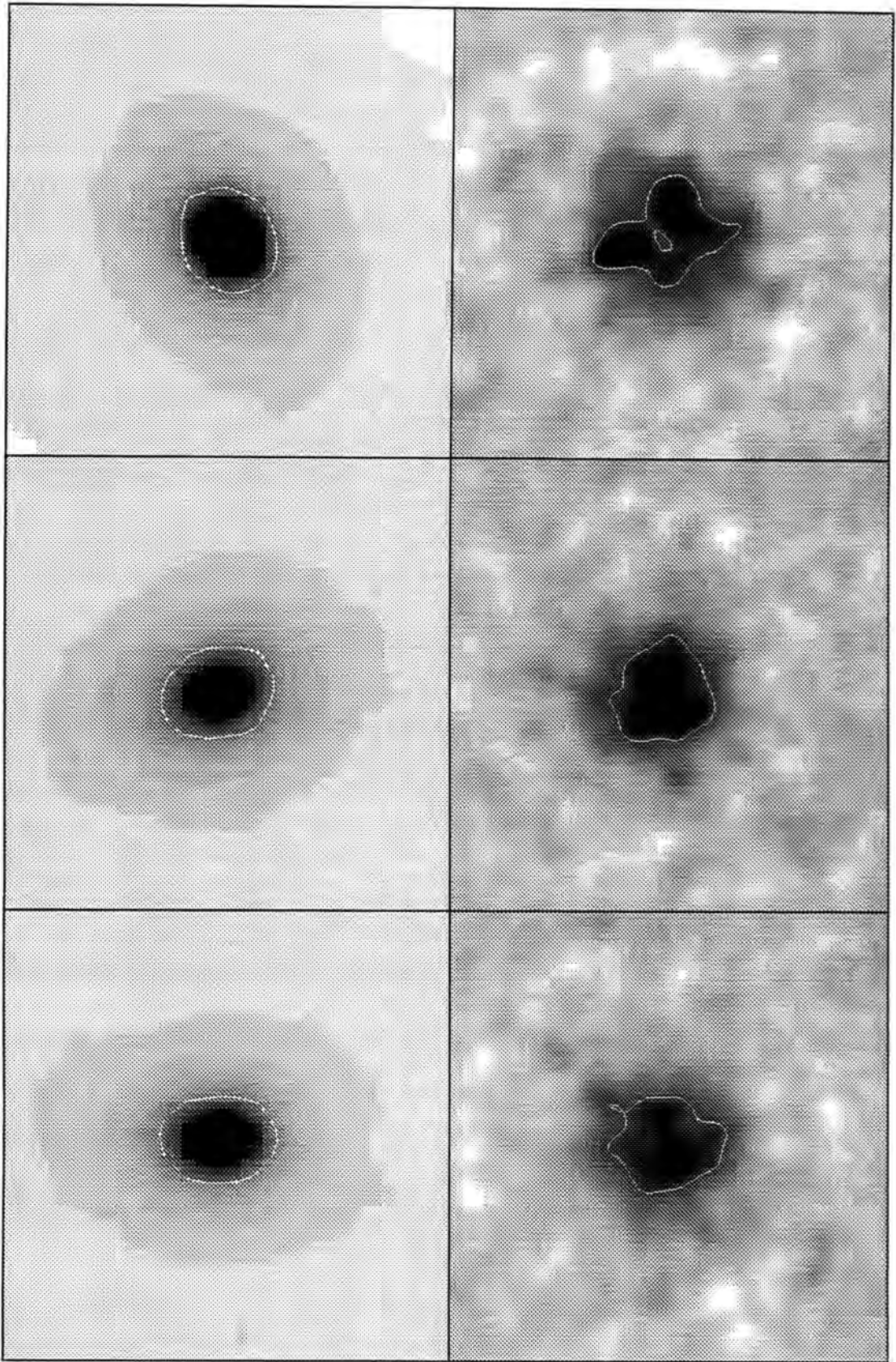
Figure 3.13:
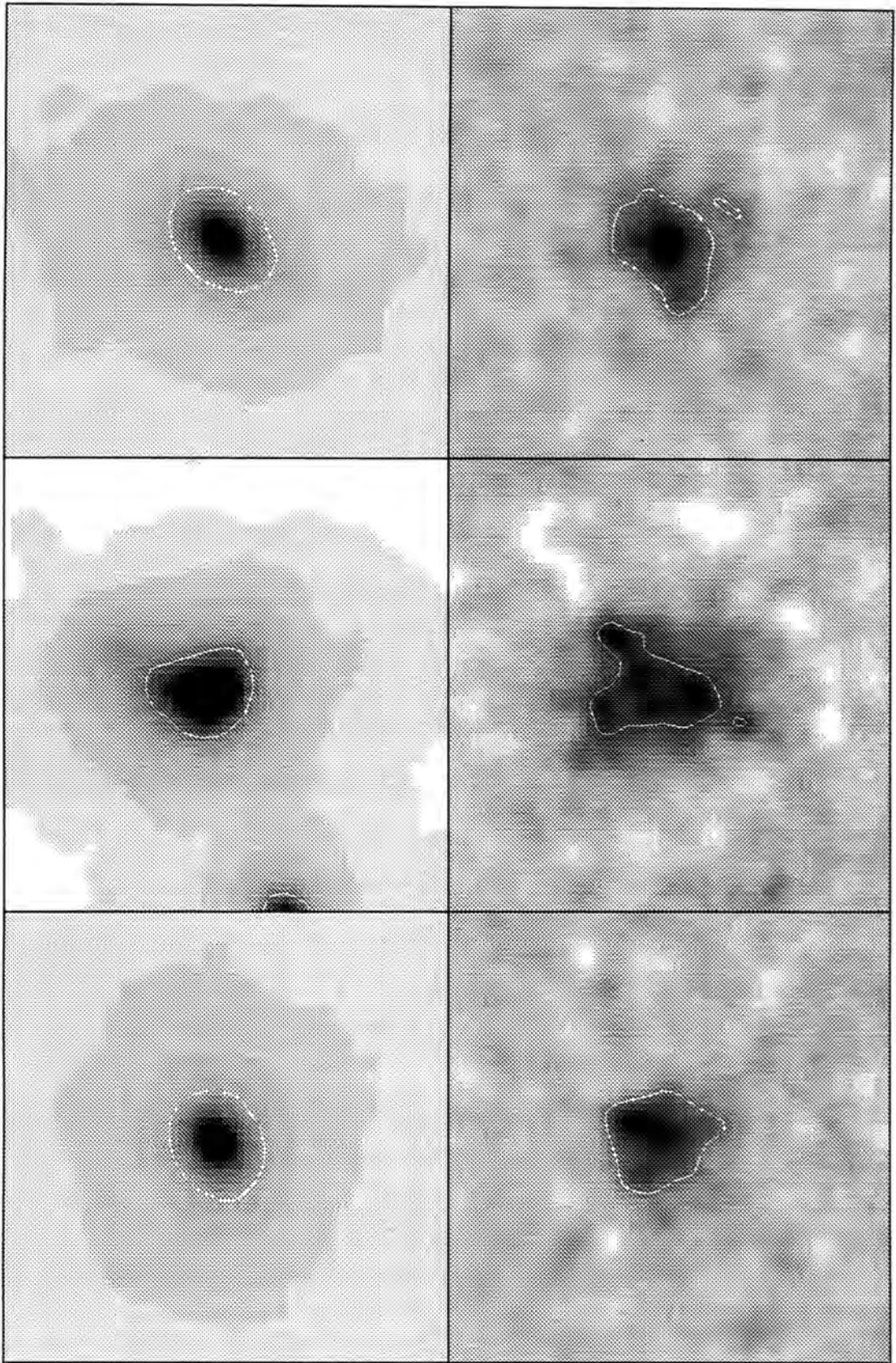
Figure 3.14:

Figure 3.15:

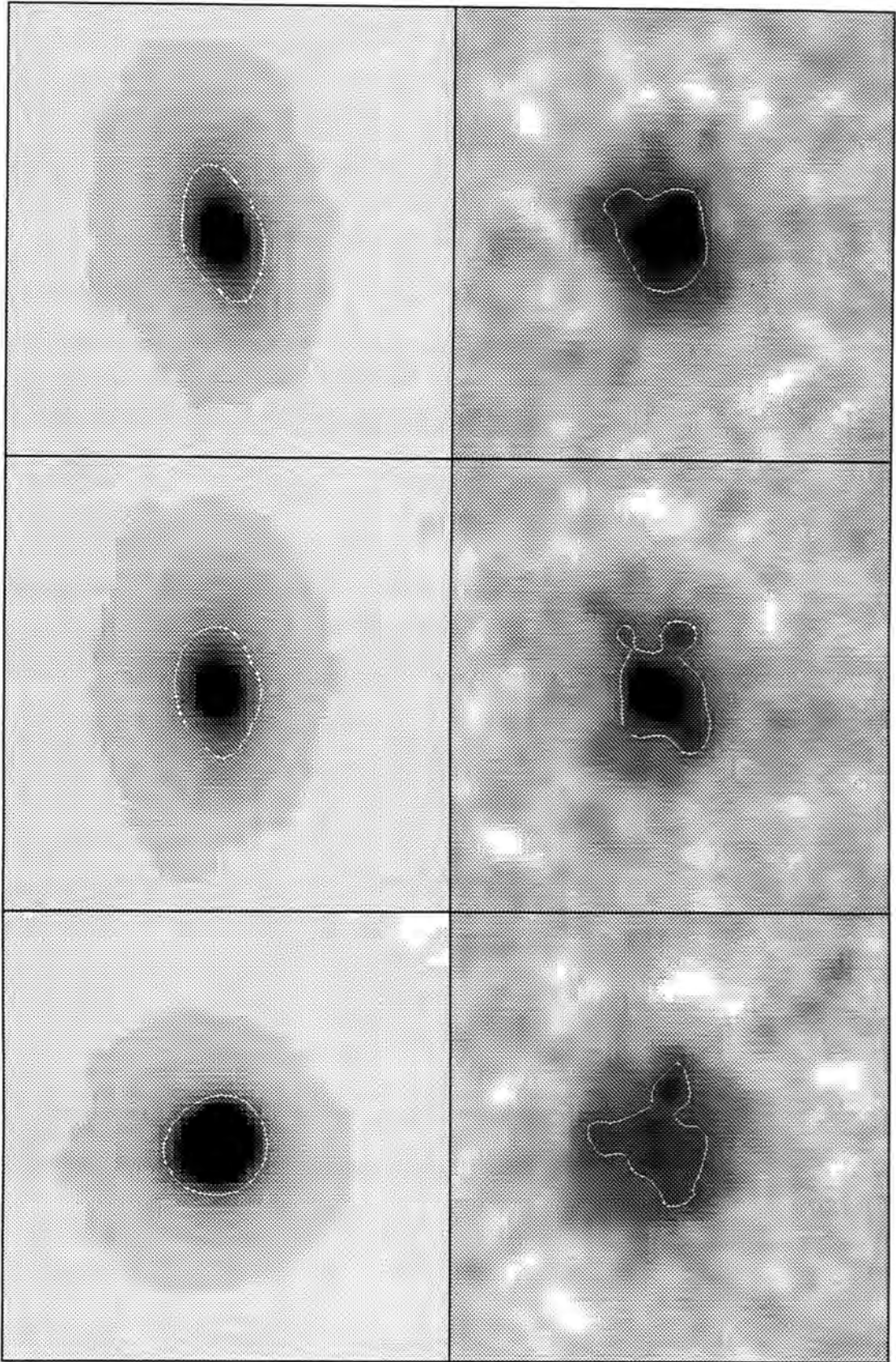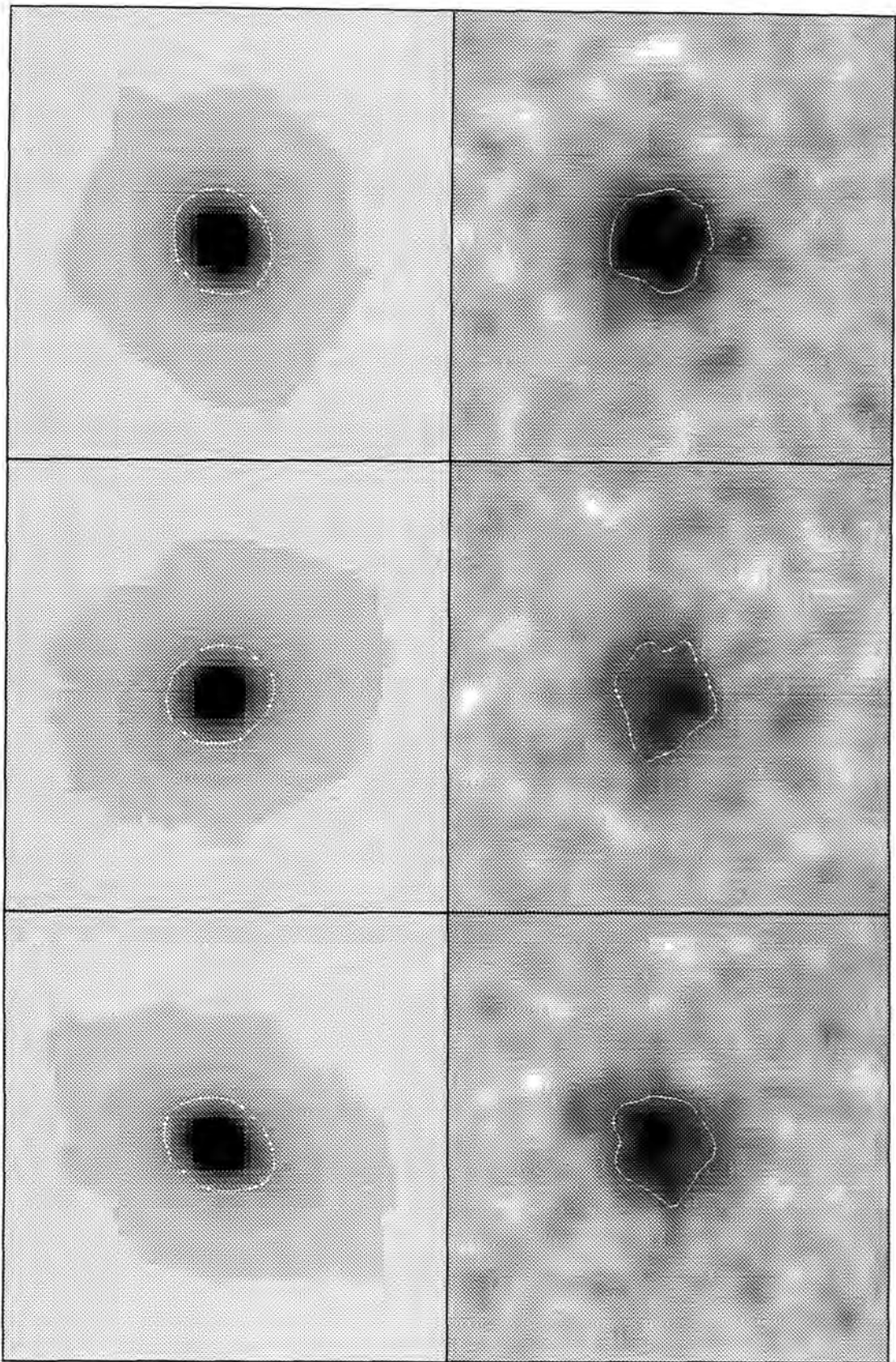Figure 3.16:

Figure 3.17:

Figure 3.18:

Figure 3.19:

Figure 3.20:

Figures 3.21 to 3.28 show the projected surface densities of the central regions of the clusters evolved in an $\Omega_0 + \lambda_0 = 1$ universe. On each page are shown the three orientations of each cluster. The left panels have been smoothed with a Gaussian of $\theta_{sm} = 0.25$ arcminutes which is the same smoothing as used in the Kaiser and Squires reconstruction. Their resulting surface overdensities are in terms of S_{crit}. The greyscale represents the surface overdensity with high overdensity being represented by dark colouring and ranges from $\hat{\sigma}$ of -0.1 to 0.5. The right panels show the corresponding reconstruction with greyscale ranging from -0.1 to 0.25. The contour encloses the 150 pixels of highest overdensity.
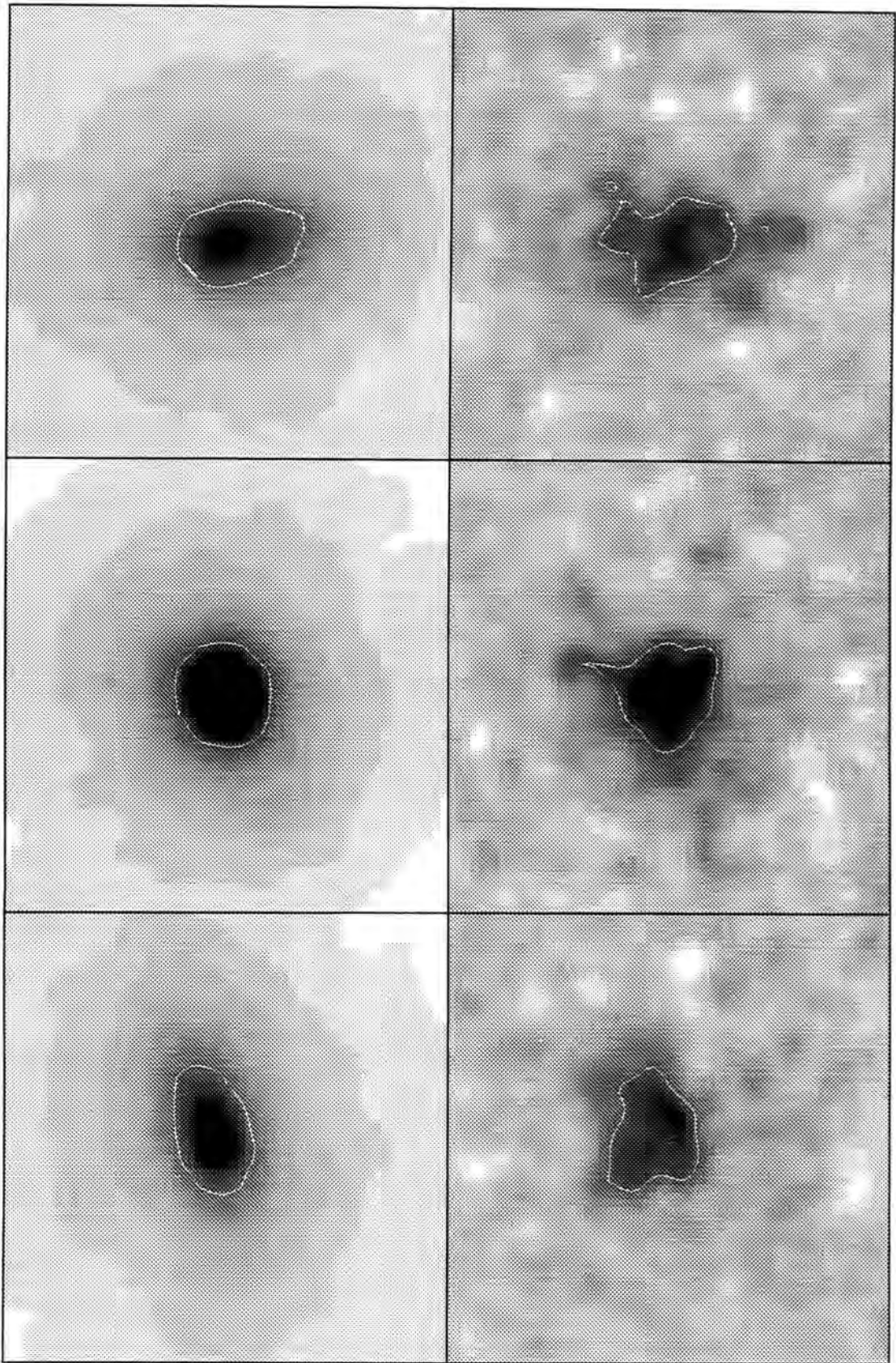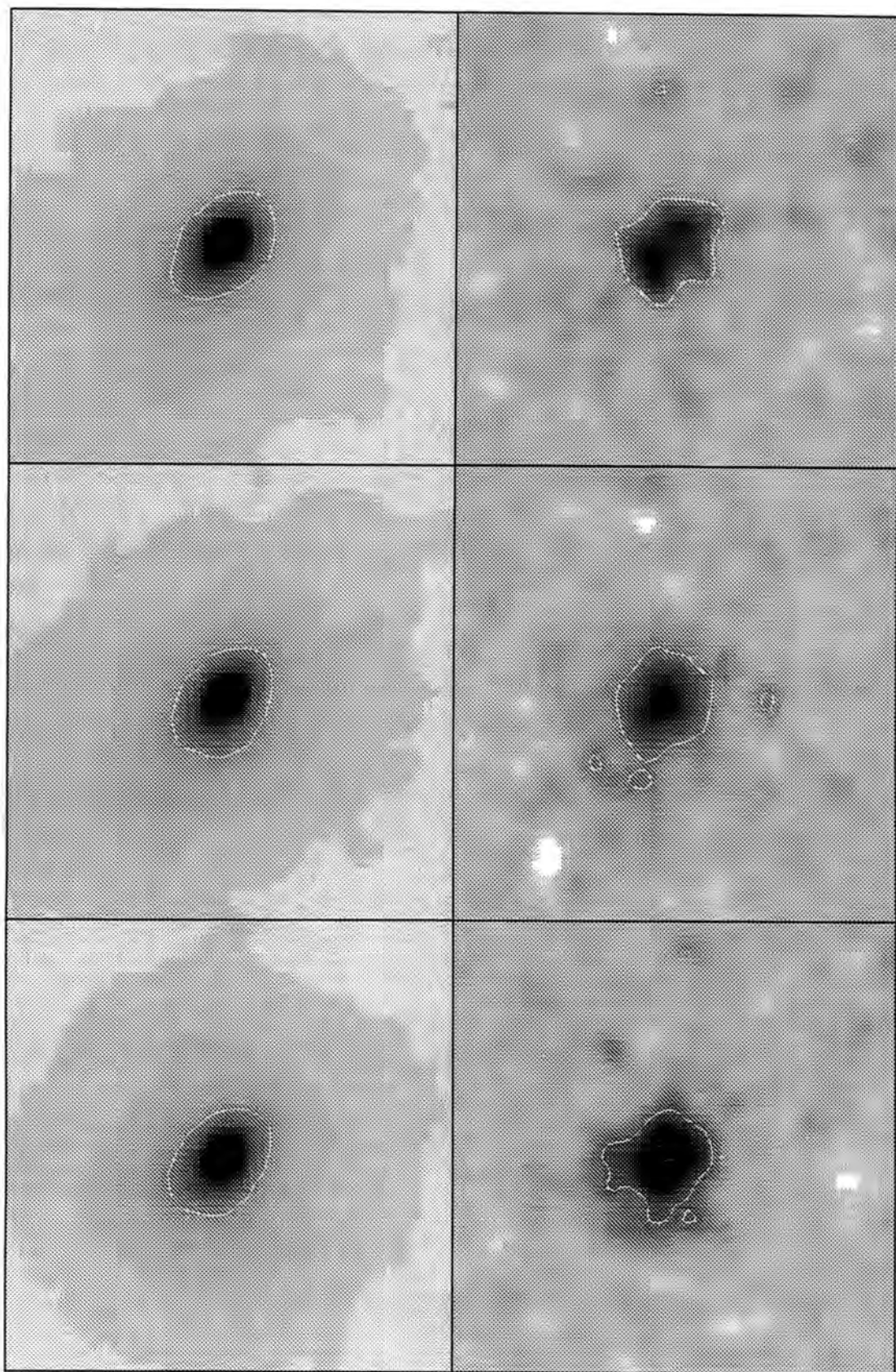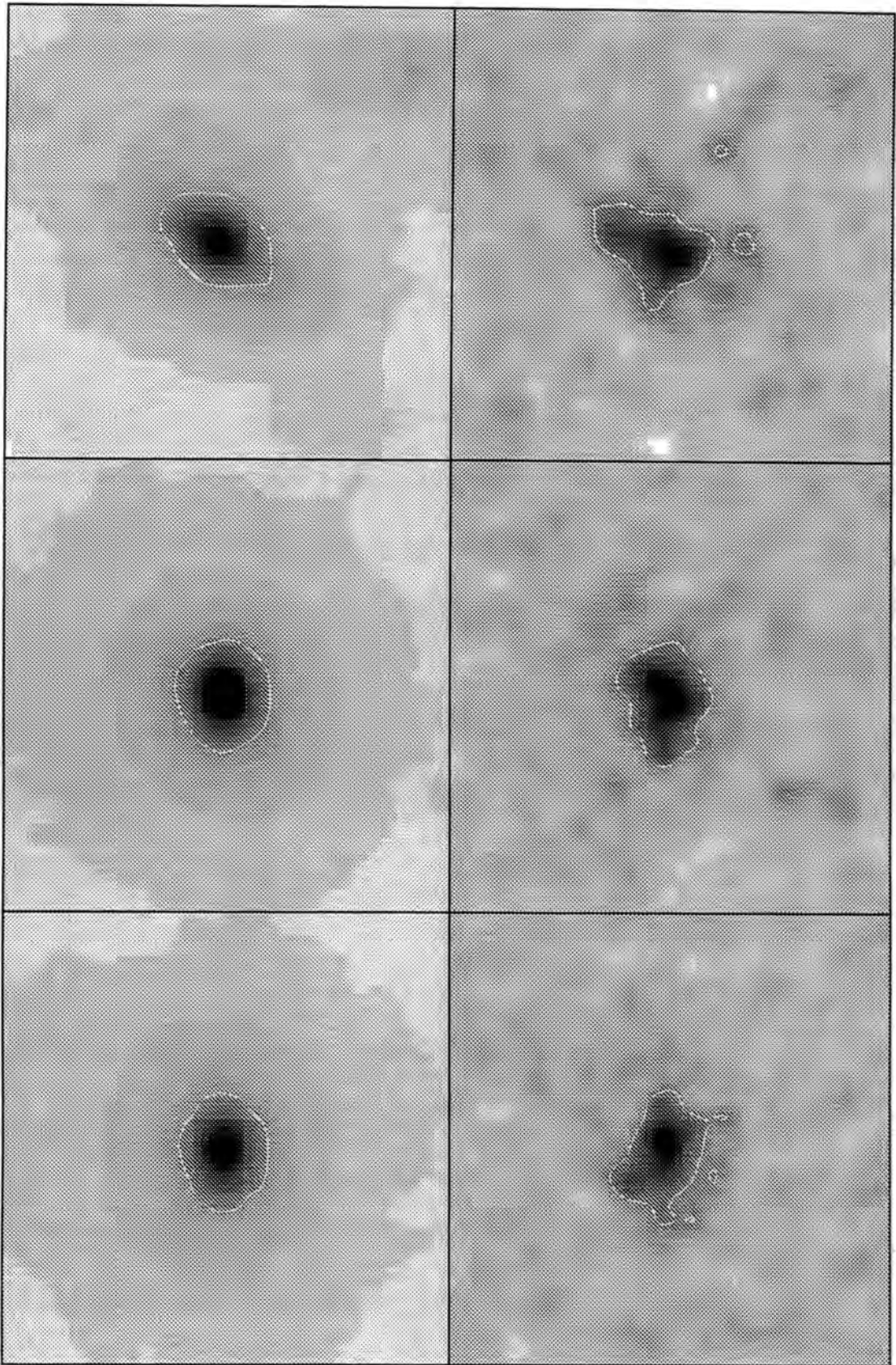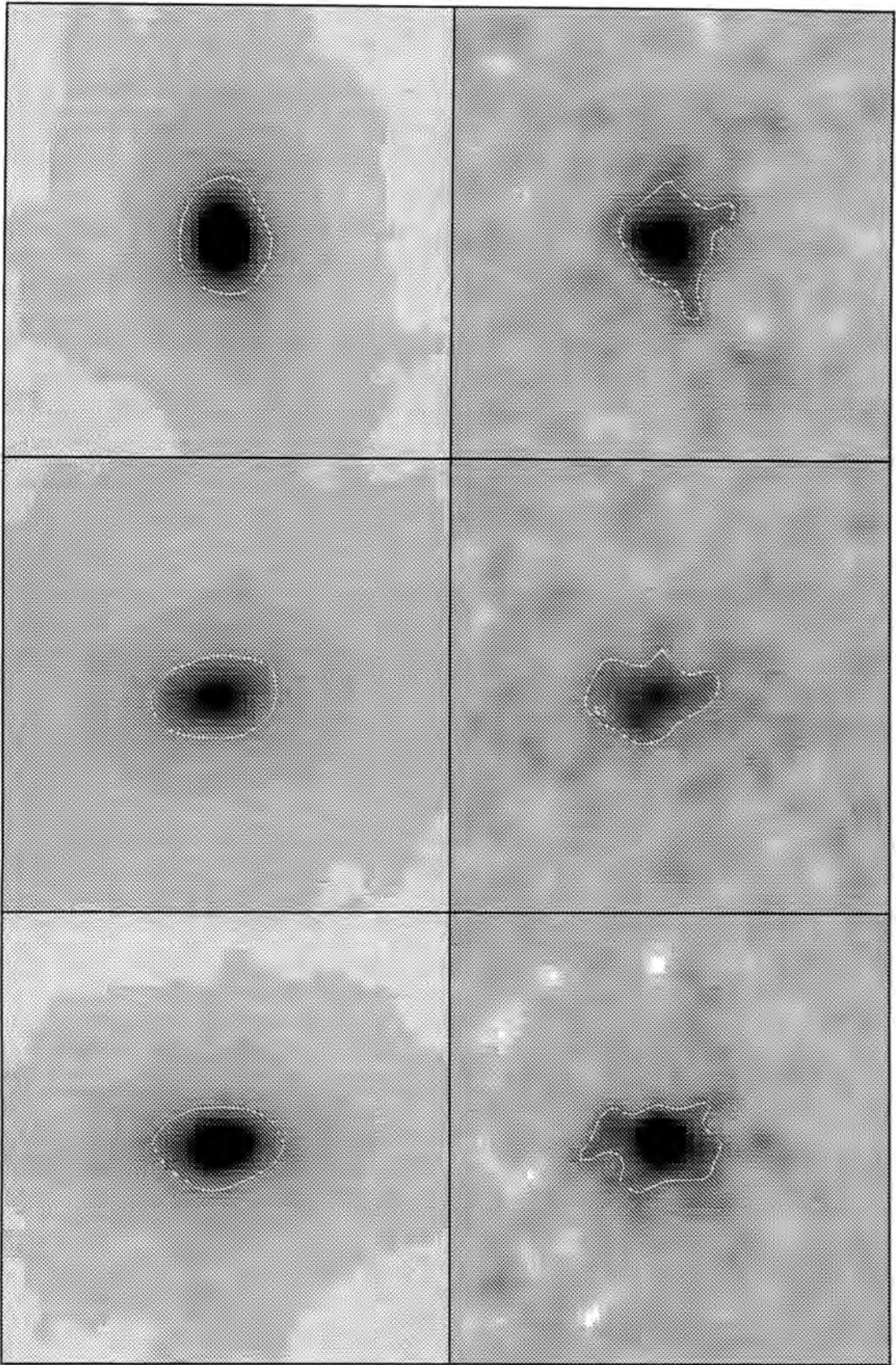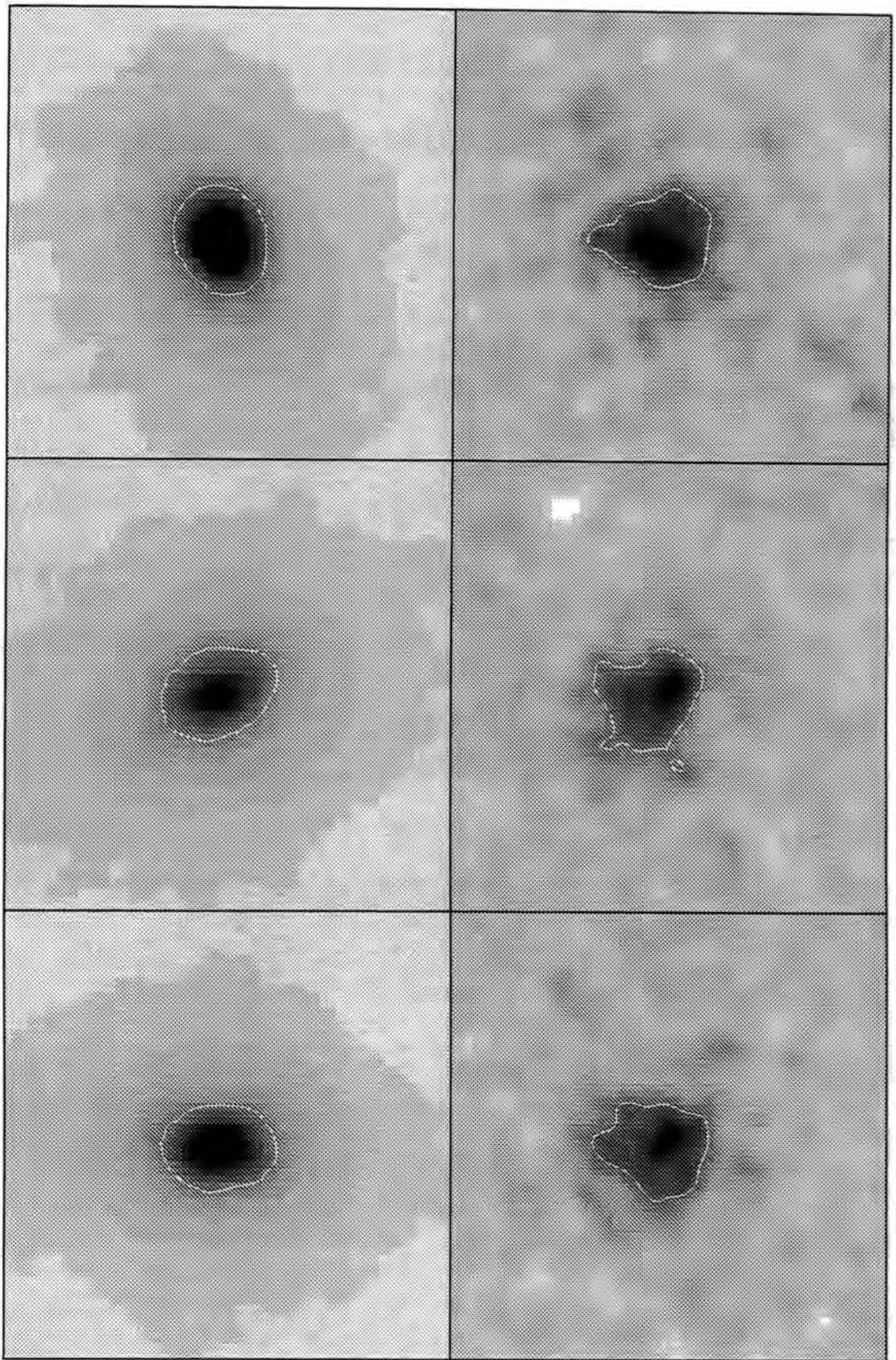
Figure 3.21:

Figure 3.22:

Figure 3.23:

Figure 3.24:

Figure 3.25:
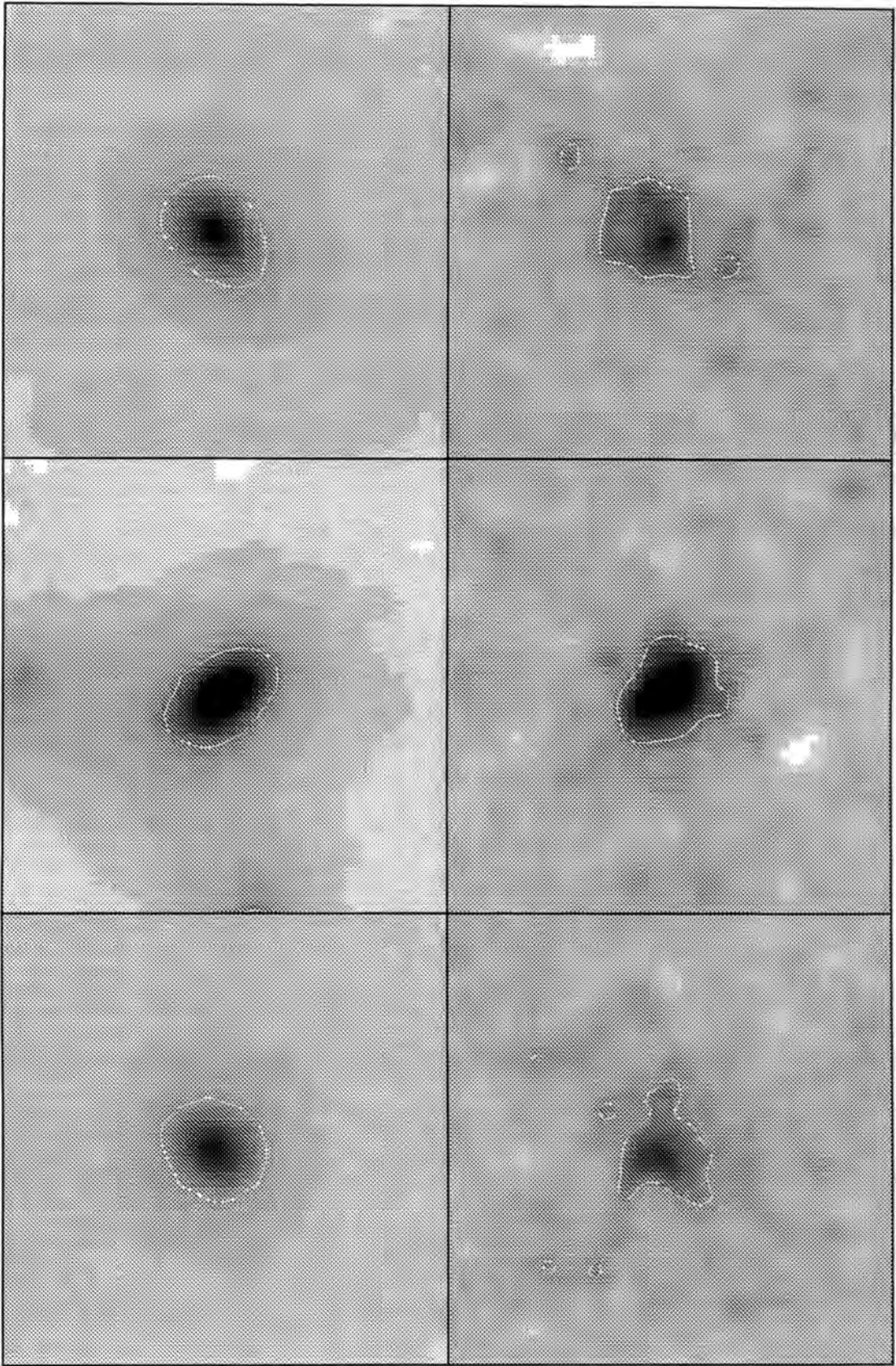
Figure 3.26:
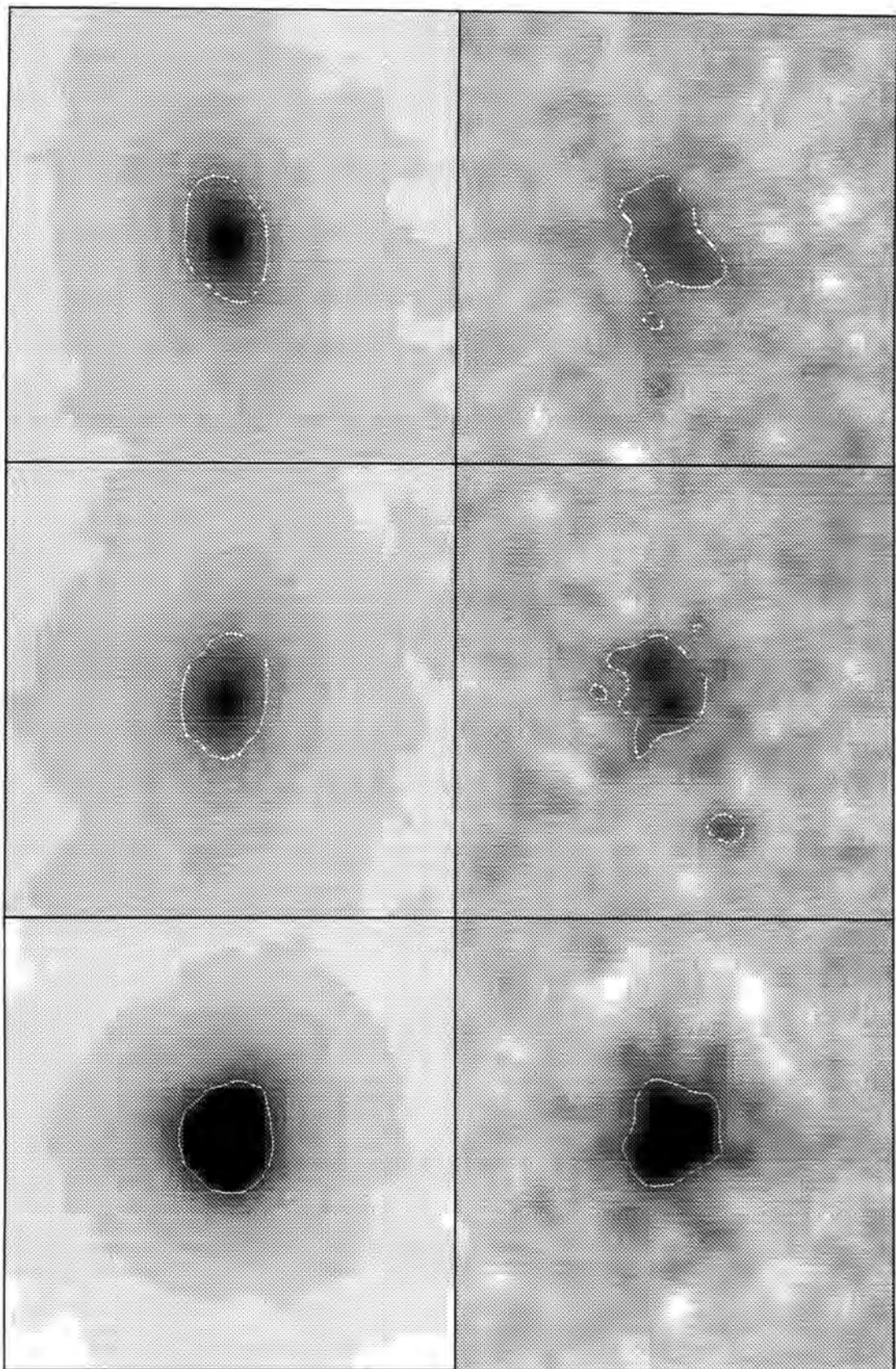
Figure 3.27:
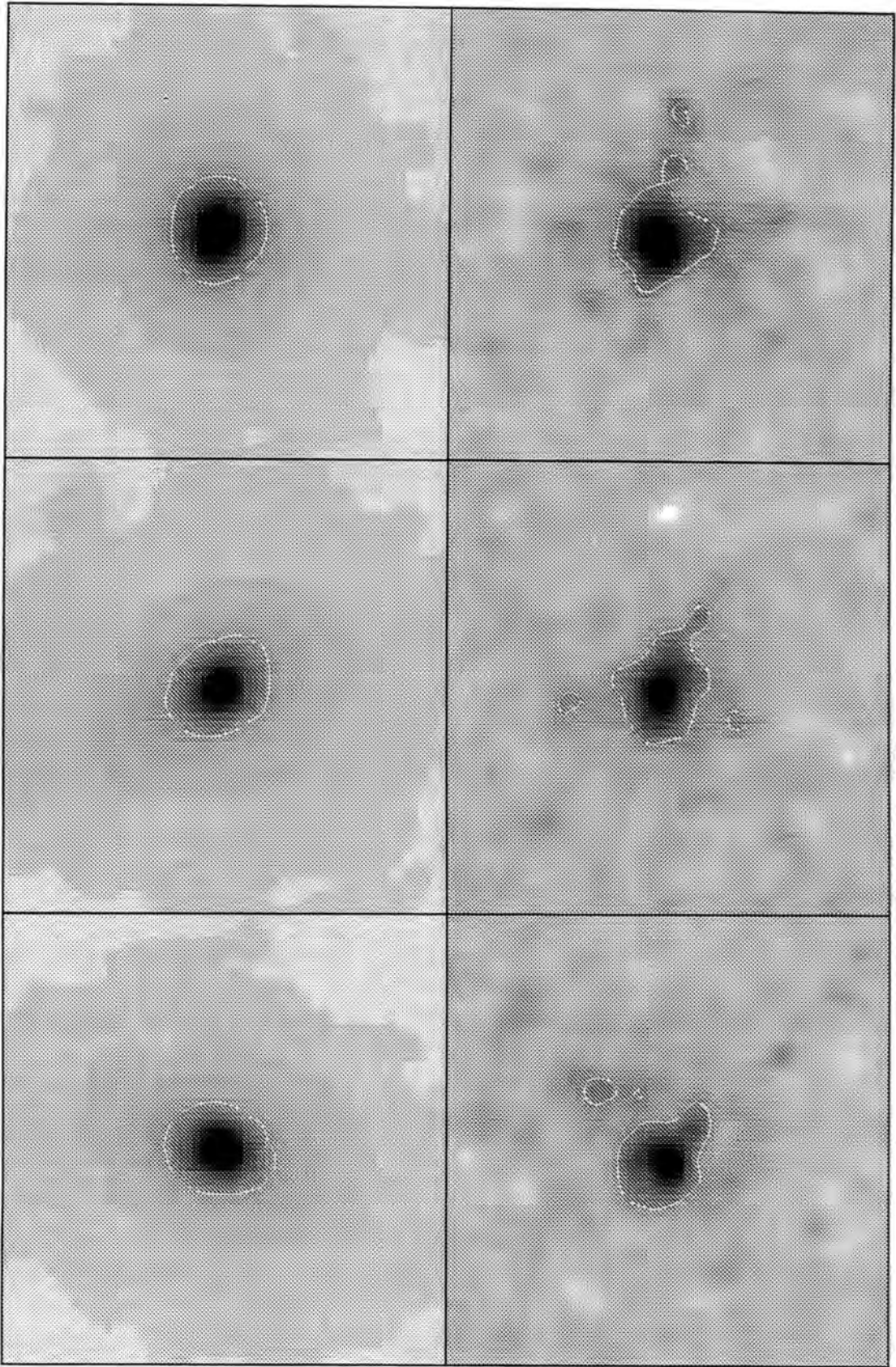
Figure 3.28:

Chapter 4

The Faint End of the LF in Moderate Redshift Clusters

4.1 Introduction

As an extension to our theoretical studies of weak gravitational lensing by rich clusters of galaxies we planned to measure the lensing distortion caused by two clusters using the Isaac Newton Telescope on La Palma. Unfortunately the seeing was too large to obtain data useful for a lensing analysis so we implemented our back-up project of deep imaging of the clusters in order to study the faint end of the luminosity function. As we describe in more detail in the following section the slope of the faint end has been the subject of much recent controversy.

4.1.1 The Schechter Function

The differential luminosity function $N(L)\,dL$ is the number of galaxies with luminosities in the range L to $L + dL$. The shape of the luminosity function must reflect in some way the formation history of the galaxies. Schechter (1976) proposed an analytic functional fit to observations, based on the theoretical form predicted for the mass distribution of galaxies (Press & Schechter 1974).

$$N(L)\,dL = N^\star \left(\frac{L}{L^\star}\right)^\alpha exp\left(\frac{L}{L^\star}\right) d\left(\frac{L}{L^\star}\right) \qquad (4.1)$$

Using the relationship between luminosity and magnitude, the Schechter function may be written in terms of magnitudes.

$$N(M)\,dM = \frac{2}{5}(\ln 10)N^{\star}10^{\frac{2}{5}(\alpha+1)(M^{\star}-M)}e^{-10^{\frac{2}{5}(M^{\star}-M)}}\,dM \qquad (4.2)$$

or, more compactly,

$$N(M)\,dM = kN^{\star}e^{k(\alpha+1)(M^{\star}-M)}e^{-e^{k(M^{\star}-M)}}\,dM \qquad (4.3)$$

where $k = \frac{2}{5} \times (\ln 10)$.

The factor $e^{-e^{k(M^{\star}-M)}}$ means that the function has a double exponential cut-off at the bright end. The slope at the faint end is determined by the α parameter. The "knee" of the function, the crossover point between the two power laws is determined by $M^{\star}$. The absolute normalisation is determined by $N^{\star}$.

The Schechter function has been applied to differential counts of both field galaxies and cluster galaxies. The slope of the faint end tends to be steeper in clusters ($\alpha \sim -1.5$) than in the field ($\alpha \sim -1$). It is very difficult, however, to measure the field luminosity function as it is necessary to measure both apparent magnitudes and redshifts to determine the absolute magnitude of the galaxies surveyed. Redshift surveys of magnitude limited samples tend to measure $M^{\star}$ objects and therefore the range in luminosities surveyed is relatively narrow. The field luminosity function has only been compiled for local redshift surveys (e.g. Peterson et al. 1986; Efstathiou et al. 1988; Loveday et al. 1992; Marzke et al. 1994). Observing cluster galaxies eliminates the uncertainty about the distance to the objects and the Schechter parameters for clusters are therefore more reliable.

4.1.2 The Schechter Function for Clusters

In a seminal paper Binggeli et al. (1985) published the luminosity function (LF) derived from their extensive study of the galaxy population in the Virgo region. The advantage of working in the Virgo cluster is that its relative proximity means that it is possible to reach far down the luminosity function. Using deep plate material they classified morphologically the galaxy populations and then derived luminosity functions for various types. Without extensive redshift information they had to assume that the populations all lay at the distance of Virgo. The luminosity function they derived had a steeply rising faint end population – at odds with the extrapolations of the luminosity functions measured in other, predominantly richer and more distant clusters e.g. Colless (1987). Unfortunately, without redshifts it was impossible to disentangle the contributions from background interlopers in this dataset and so their result while interesting was not conclusive.

Part of the reason for the interest in the faint end of the cluster luminosity function is that recently there have been a number of developments in the study of

that end of the field luminosity function. It has long been acknowledged that deep optical counts show much higher number densities of galaxies to faint limits than expected from no-evolution predictions (Tyson 1988; Metcalfe et al. 1995; Smail et al. 1995). There are several possible explanations for this:-

1. Galaxies were more abundant in the past and subsequently merged e.g. Guiderdoni & Rocca-Volmerange (1990); Broadhurst et al. (1991).

2. Very faint galaxies from far down the luminosity scale have been brightened considerably by some evolutionary process like starbursting (Broadhurst et al. 1988). These galaxies would add to the measured number density at the faint magnitudes presently observed.

3. More controversially, some authors have claimed that the luminosity function of the local field galaxy population has been substantially under-estimated (Davies et al. 1994; McGaugh 1994; Cole et al. 1994; McGaugh et al. 1995). They claim that, as a result of surface brightness biases in the photographic material of the plates used to select objects for local field studies, a large population of extended low surface brightness galaxies has been missed.

4. Confusingly (and even more specifically) some authors (Impey et al. 1988; Phillipps & Driver 1995; Babul & Ferguson 1996) claim that only faint dwarf galaxies have been missed. The inclusion of these dwarf galaxies increases the slope of the Schechter function because the dwarfs only begin to appear lower down the luminosity function. If this is true then the local field luminosity function, instead of having a relatively flat faint end slope $\alpha \sim -1$, in the standard Schechter (1976) parametrisation (Efstathiou et al. 1988; Loveday et al. 1992) may have a steeply rising tail, $\alpha \sim -1.5$.

To determine accurately the true local field luminosity function is a laborious task. However, there are other environments where looking for evidence of a steep end slope to the galaxy luminosity function is easier and hints uncovered in these regions may throw light on the true local field population. The simplest environment to study is one which contains a large number of galaxies all at the same distance: a rich cluster. Unfortunately, this is also a regime where we might expect environmental processes to have their greatest effect, evidence for which may already exist in the observed morphology-density relationship (Dressler 1980). Nevertheless, it is in studies of rich clusters where most of the recent work has concentrated (Thompson & Gregory 1993; Driver et al. 1994; Bernstein et al. 1996; Biviano et al. 1995). Of these papers it is that of Driver et al. (1994)[DPDMD] which provides the strongest evidence for a steep slope to the luminosity function in the range $M^* + 2$ to $M^* + 6$.[1]

Driver et al. (1994) obtained a total integration time of 2.4 ksec in B and R of a 6 × 4 arcmin region in the distant cluster A963, $z = 0.206$, using the Hitchhiker

---

[1] We adopt $q_o = 0.5$ and $H_o = 50$ km sec^{-1} Mpc^{-1}. With these parameters 1 arcsec is equivalent to 3.91 kpc at $z = 0.18$.

parallel camera on the 4.2-m WHT. They used the data to investigate the number counts in this region and by statistically correcting for the field contamination from counts obtained with the same instrument in a number of blank fields they attempted to measure the cluster galaxy luminosity function down to $R \sim 24$ (equivalent to $M^* + 6$). They found a steeply rising faint end slope, with $\alpha \sim -1.8$ in the standard Schechter parametrisation. Worryingly, this corresponds to an equivalent count slope of $\log_{10}(dN/dm) \sim 0.3$, very close to the observed slope of the field counts. Thus their result could be reproduced by a simple zero-point shift between the magnitude scales of their field and cluster images, albeit of rather large amplitude $\delta m \sim 0.2$. Unfortunately, owing to its operational role the Hitchhiker system was only calibrated once a year and thus it is difficult to gauge the likelihood of such an error, although they quote an rms scatter on the zero point of ± 0.1 mag. To address this issue DPDMD compared their photometry with data from a shallow photographic survey and claim that they can rule out such an offset for their A963 exposure. Nevertheless, without corroborating evidence, either in this cluster or in others, it would appear prudent to suspend judgement on the reality of the claimed high value of α obtained.

To provide an independent check of the result reported by Driver et al. we have analysed deep two color photometry of two distant $z = 0.18$ clusters to measure the cluster galaxy luminosity function. Our cluster dataset is similar in quality and depth to Driver et al.'s, although it covers a larger region in the clusters than that of DPDMD. To provide field counts with the same selection criteria and conditions as our cluster images, rather than relying on published counts from the literature, we have analysed a wide-field V and I imaging survey of blank fields. In addition we have taken great care to ensure the homogeneity of the photometric systems used for both the cluster and comparison blank fields. We discuss our observational dataset in Section 4.2, present our analysis in Section 4.3, and give our main conclusions in Section 4.4.

4.2 Observations and Reduction

4.2.1 A1689 and A665

The two clusters analysed in this study were A1689 and A665. These clusters both lie at approximately $z = 0.18$ (A1689 at $z = 0.181$ and A665 at $z = 0.182$). They are both optically rich with Abell richnesses of 4 and 5 respectively. They have somewhat different morphologies, with A1689 containing a very dense central group of galaxies and A665 having a single central cD galaxy (See Figures 4.1 and 4.2). Both clusters have high velocity dispersion: $\sigma_{cl} = 1800$ km sec^{-1} for A1689 (Gudehus 1989) and $\sigma_{cl} = 1200$ km sec^{-1} for A665 (Oegerle et al. 1991). In addition both are strong X-ray sources with luminosities in the 2–10 keV band [A1689, $L_X = 2.0 \times 10^{45}$ ergs sec^{-1}; A665, $L_X = 1.2 \times 10^{45}$ ergs sec^{-1} (Soltan & Henry 1983)] A665 also has a measurable Sunyaev-Zeldovich decrement (Birkinshaw et al. 1991). Finally, both

clusters show evidence of strongly lensed features in their core regions.

The characteristics of these clusters are very similar to the cD-dominated cluster A963 studied by Driver et al. (1994). A963 is a richness class 3 cluster at $z = 0.206$ which is a strong X-ray source ($L_X = 0.95 \times 10^{45}$ ergs sec^{-1}, Soltan & Henry 1983) and also contains two giant arcs (Lavery & Henry 1988; Ellis et al. 1991).

4.2.2   Data Acquisition

The I and V imaging of the two clusters used in our analysis was collected with the Prime Focus imager on the 2.5-m Isaac Newton Telescope (INT), La Palma. The comparison I and V observations of blank fields needed to correct for field contamination come from deep imaging with the f/1 camera on the 3.9-m Anglo-Australian Telescope (AAT), Siding Springs.

4.2.3   INT PF Imaging of A1689 and A665

The imaging data on the two clusters, A1689 and A665, was collected using both the 2k^2 "Pennypacker" thick Ford and the 1k^2 EEV CCDs on the nights of 22–28 February 1993. The seeing during this run varied between 1.4–2.3 arcsec, far in excess of the limit required for the intended programme of lensing observations. Instead the back-up programme of deep imaging of the clusters was undertaken. This involved imaging in I and V of the two clusters, at $z \sim 0.18$. These passbands roughly translate to rest frame B and R respectively. Our observing technique was to take multiple exposures (each of 1000s) of the cluster, dithering the telescope by ~ 15 arcseconds between exposures. This allowed us to create a master flatfield as explained in the next section.

4.2.4   Data Reduction

The reduction of the images was complex. The fields were very crowded, as can be seen from Figures 4.1 and 4.2. Our aim was to detect the faintest objects possible. It was therefore extremely important to flatfield the frames carefully to ensure that the signal-to-noise ratio was maximised. To this end we flatfielded the frames not once but twice. Firstly we flatfielded each frame using twilight flats as is standard practice. Secondly, because we had offset the telescope between exposures, we could use the twilight flatfielded data frames themselves to create an even better master flatfield for each passband. We did this by detecting objects using the Faint Object Classification and Analysis System, FOCAS (See Valdes et al. 1983 and Chapter 2). We then cleaned the bright objects off the data frames, replacing them with sky values drawn from regions around the objects. Because of our strategy of displacing the telescope between exposures, bright objects were in different places on the

different frames and certain pixels were not always saturated. The cleaned frames were then aligned and median stacked to produce the master flatfield.

The reduction procedure in detail was

- The frames were bias subtracted and trimmed. The median bias level was obtained from the overscan region of the chip and subtracted off. The images were then trimmed to remove the overscan strips.

- Initial flatfielding using twilight flats.

- FOCAS (Valdes et al. 1983) used to detect bright objects in the frames. These were then removed and replaced by sky values drawn from regions around the objects.

- The cleaned frames were aligned and median combined.

- The initially flatfielded frames were flatfielded using the masterflat.

- The images were geometrically re-mapped to a single basis frame (centred on the cluster) and then stacked using standard IRAF routines.

The characteristics of the final datasets are summarised in Tables 4.1 and 4.3. The nights of 22 and 28 February were deemed to be photometric and calibration of all passbands was made using these nights.

Extinction Some fraction of the light travelling to us from distant galaxies is scattered by dust particles in the upper atmosphere and never reaches the telescope. This scattering of the light is wavelength dependent, being more important in the blue than the red, and also proportional to the total distance the light travels through the atmosphere i.e. the airmass. Standard stars from Landolt (1992) were observed across a large range of airmass to provide extinctions and zero points for the various clusters and passbands.

Absorption Some light is also lost by dust extinction as it travels through our galaxy . An absorption or reddening correction which is dependent on the path taken must also therefore be made. We corrected our magnitudes using Burstein & Heiles (1984).

K-correction In converting from apparent to absolute magnitude account must be taken of the fact that each galaxy's spectrum has been redshifted and stretched. K-corrections, the redshift dependent terms introduced to correct for this effect, are specific to the observed bandpass and morphological type. We used

$$M = m - 5\log_{10} D - 25 - (K - \text{correction}) \qquad (4.4)$$

where D is the luminosity distance to the cluster, and the K-correction is $1.36z$ for I and $3.13z + 0.24z^2$ for V.

The final zero point errors were $\Delta I = 0.04$ and $\Delta V = 0.03$, obtained from a combination of extinction, zero point and frame-to-frame errors.

4.2.5 Cluster Galaxy Catalogues

Having acquired and reduced our images we next needed to analyse them to provide catalogues of object positions, magnitudes and colours. To achieve this we used the SExtractor analysis package (Bertin 1994). We use this package in preference to FOCAS for two reasons — firstly because it is faster and secondly because it is better at separating very close objects. Like FOCAS, the SExtractor package requires the user to specify certain parameters, most importantly a minimum area and a maximum intensity relative to background levels, before "detecting" an object. SExtractor then deblends the objects and produces a catalogue of their properties. The object catalogue created includes information on the object positions, shapes, profiles and magnitudes (isophotal, aperture and Kron).

Tests were run on small sections of both the I and V images of the final cluster frames to find the best detection parameters for SExtractor. The final values we adopted are shown in Table 4.8.

We took aperture magnitudes within 6 arcsec diameter apertures. We show the differential number counts in I and V in our two clusters in Figures 4.10 to 4.13.

4.2.6 Removal of Stars

We corrected the data for stellar contamination by plotting isophotal radius versus magnitude for each object. As can be seen from Figure 4.3, two distinct populations are evident at bright magnitudes. The more compact objects at each magnitude are the stars. For each frame a line separating the populations was determined visually and the objects below the line were removed from the counts.

At faint magnitudes ($I \geq 18$) it is more difficult to remove the stars and it seems likely that some contamination will remain. However, the fraction of stellar interlopers is likely to be small and to be similar for the cluster and field data. We are primarily interested in the faint end of the luminosity function and the severity of the problem of star removal becomes reduced as the magnitude increases.

4.2.7 AAT f/1 Imaging of Blank Fields

These data come from a wide-field CCD survey of the equatorial LDSS fields at 10^{hrs} and 13^{hrs}. The detector is a $1k^2$ Thomson CCD with 0.98 arcsec/pixel sampling, providing a large field of view ($\sim 17'$ square). The data were all taken in photometric conditions, although in only modest seeing. Nevertheless, the depth and seeing of
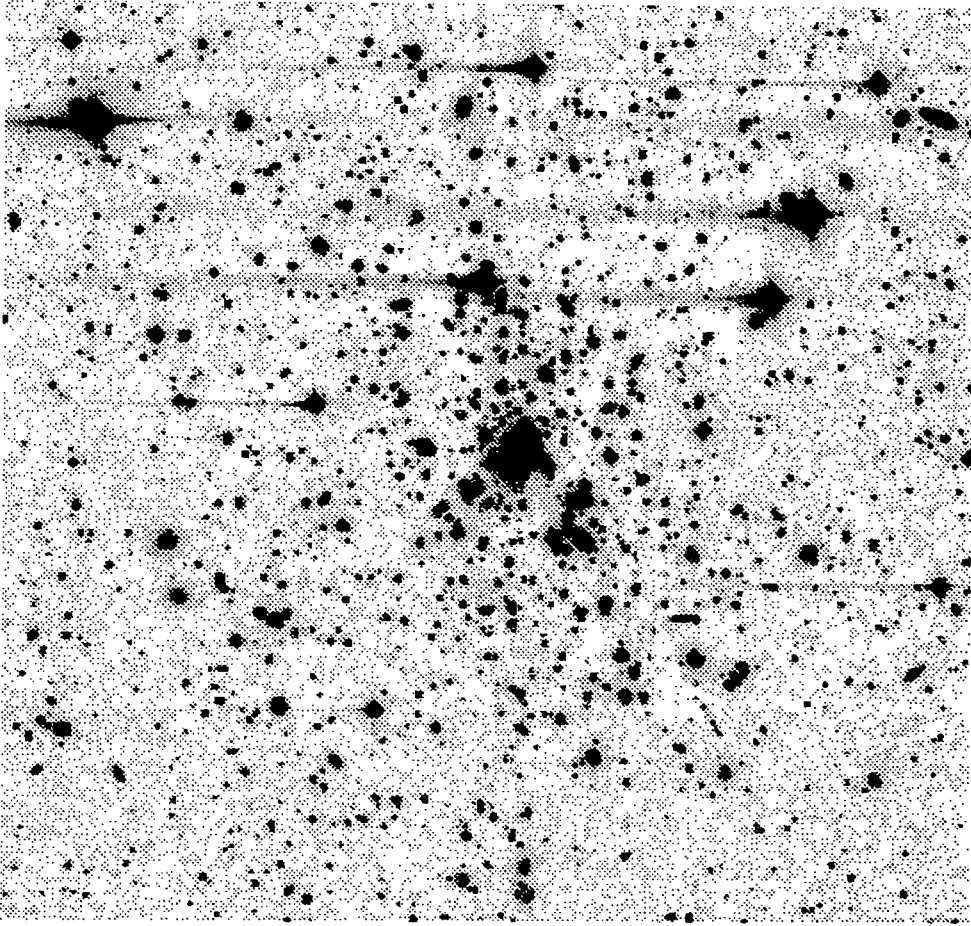
Figure 4.1: A1689 I image. The field of view is 11.29 arcminutes × 10.61 arcminutes (2.65 × 2.49 Mpc)
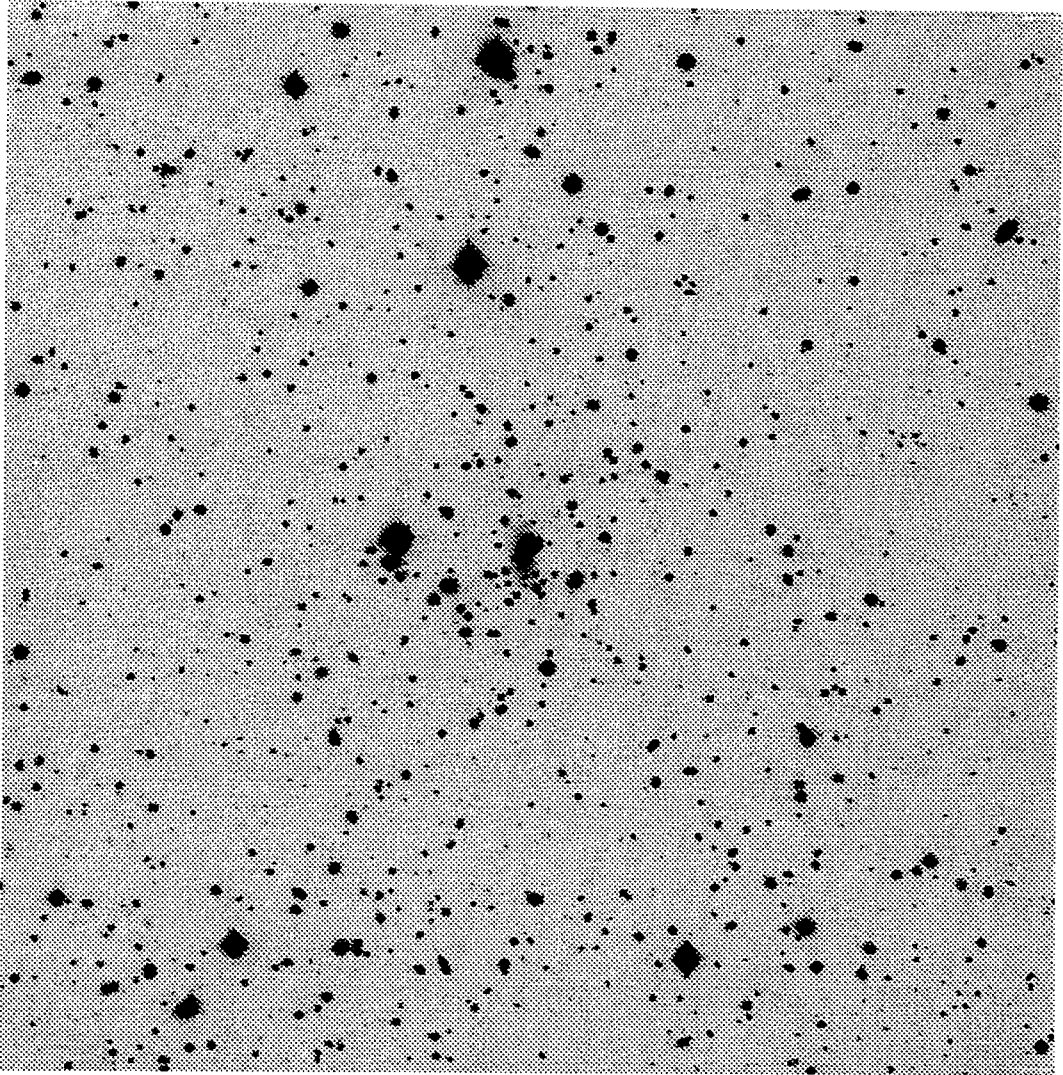
Figure 4.2: A665 I image. The field of view is 12.34 arcminutes × 12.3 arcminutes (2.90 × 2.88 Mpc)
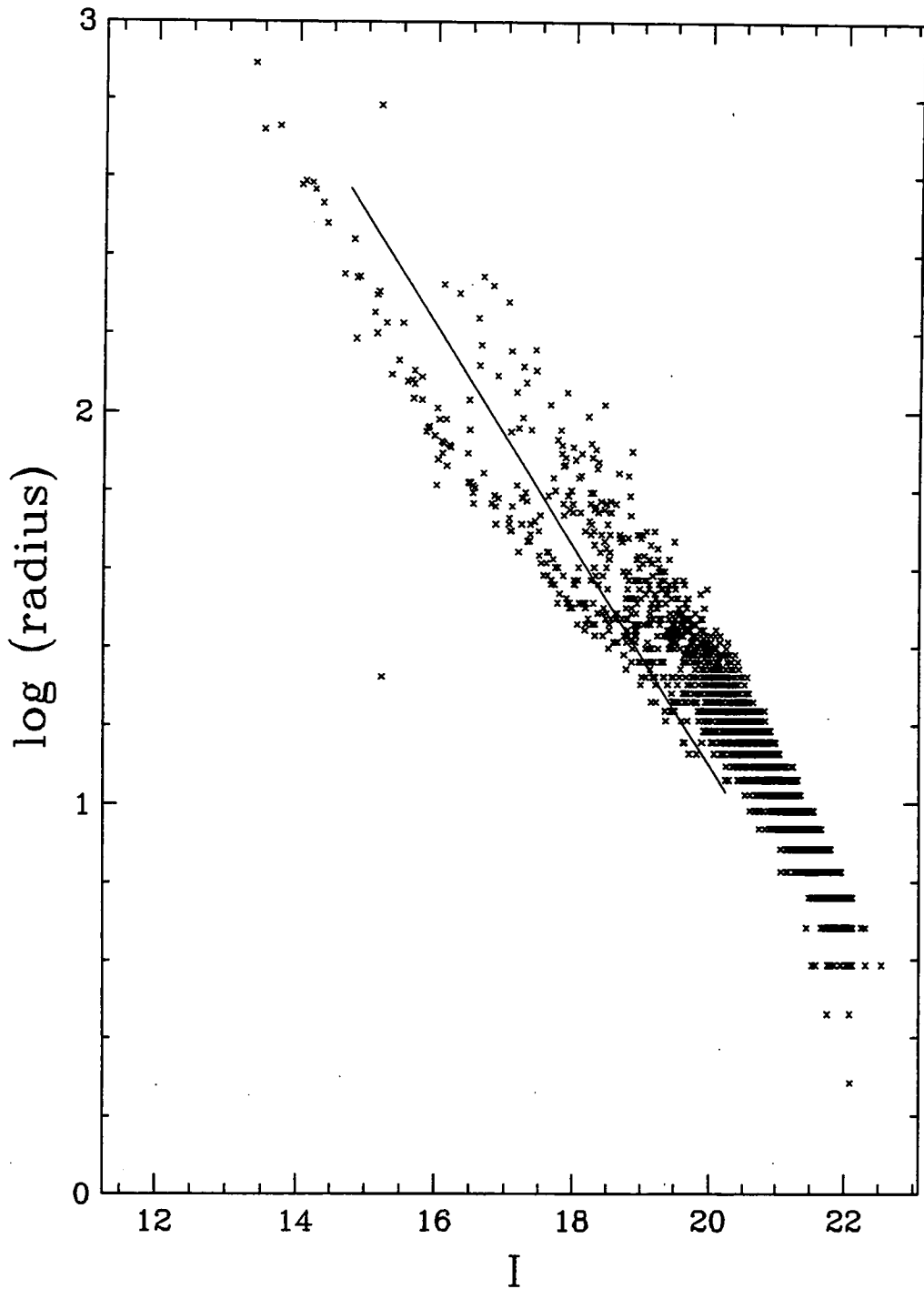
Figure 4.3: The figure shows each object detected (from an I field frame). The isophotal radius has been plotted against the magnitude. Two distinct populations are evident at bright magnitudes. The more compact objects at each magnitude i.e. those lying below the line, are the stars.

A1689
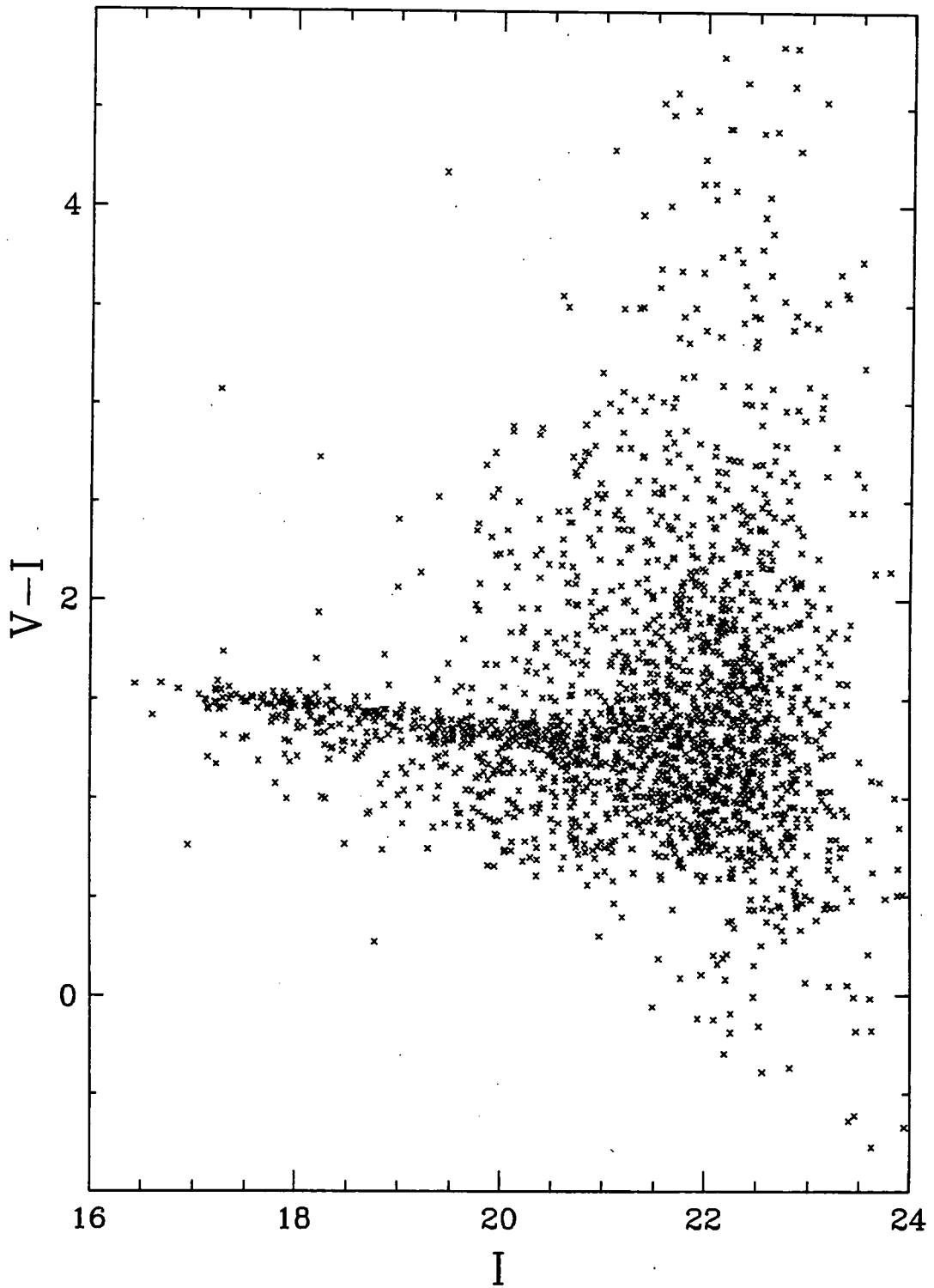
Figure 4.4: $(V - I)$-I colour-magnitude diagram for the A1689 field. Note the strong linear feature associated with the dominant red cluster population.

A665
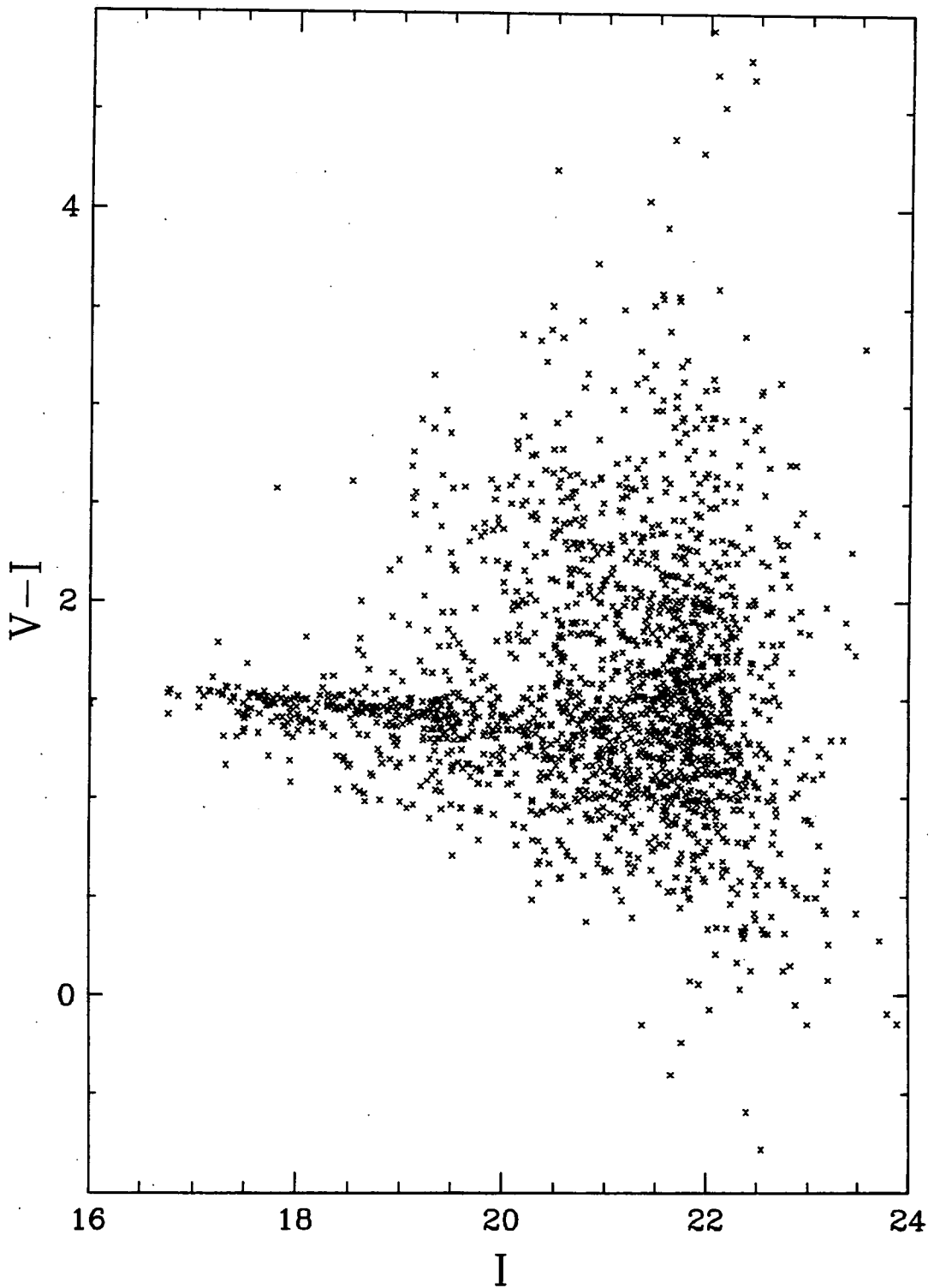

Figure 4.5: $(V-I)$ - I colour-magnitude diagram for the A665 field. Note the good agreement between the colours of the loci in this cluster and in figure 4.4.

I Field Frames

Figure 4.6: Field number counts for 9 I-band AAT frames. The error bars for one frame are shown. Also shown is the best fit line to the counts with slope of 0.345. For errors to this line see Figure 4.7.

Figure 4.7: The error contour for the I field counts fit. The contour is $\chi^2_{min} + 2.3$ which corresponds to a 68% confidence ellipse for normally-distributed errors. To minimise errors the origin was moved to (20,0) i.e. x becomes $x - 20$. The minimum χ^2 occurred at [2.2323,0.345]. The recovered line $y = mx_{new} + c$ when reconverted yields $y = mx_{old} + (c - 20m)$ ie $y = 0.345x - 4.665$ as stated in the text.
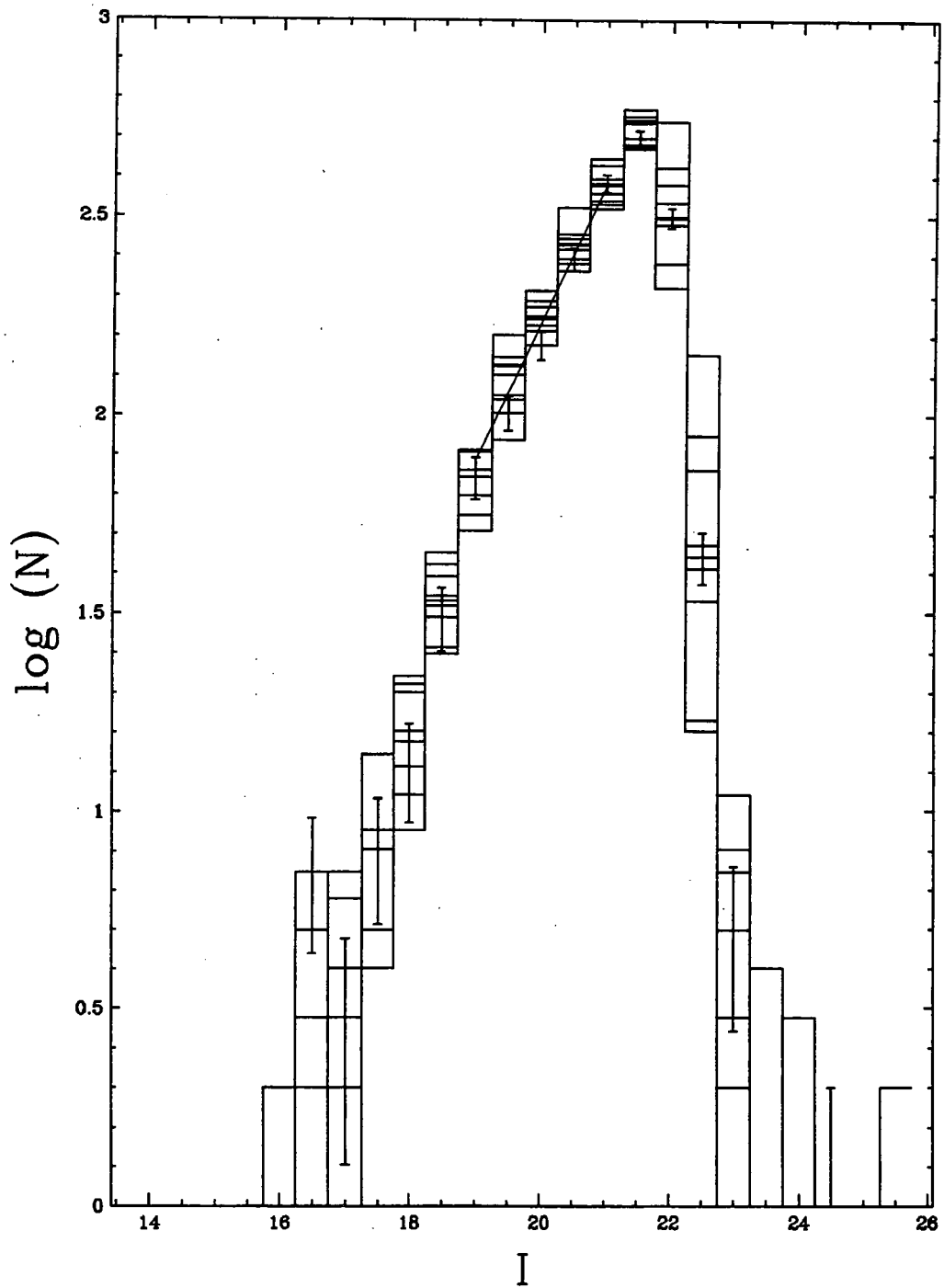
V Field Frames
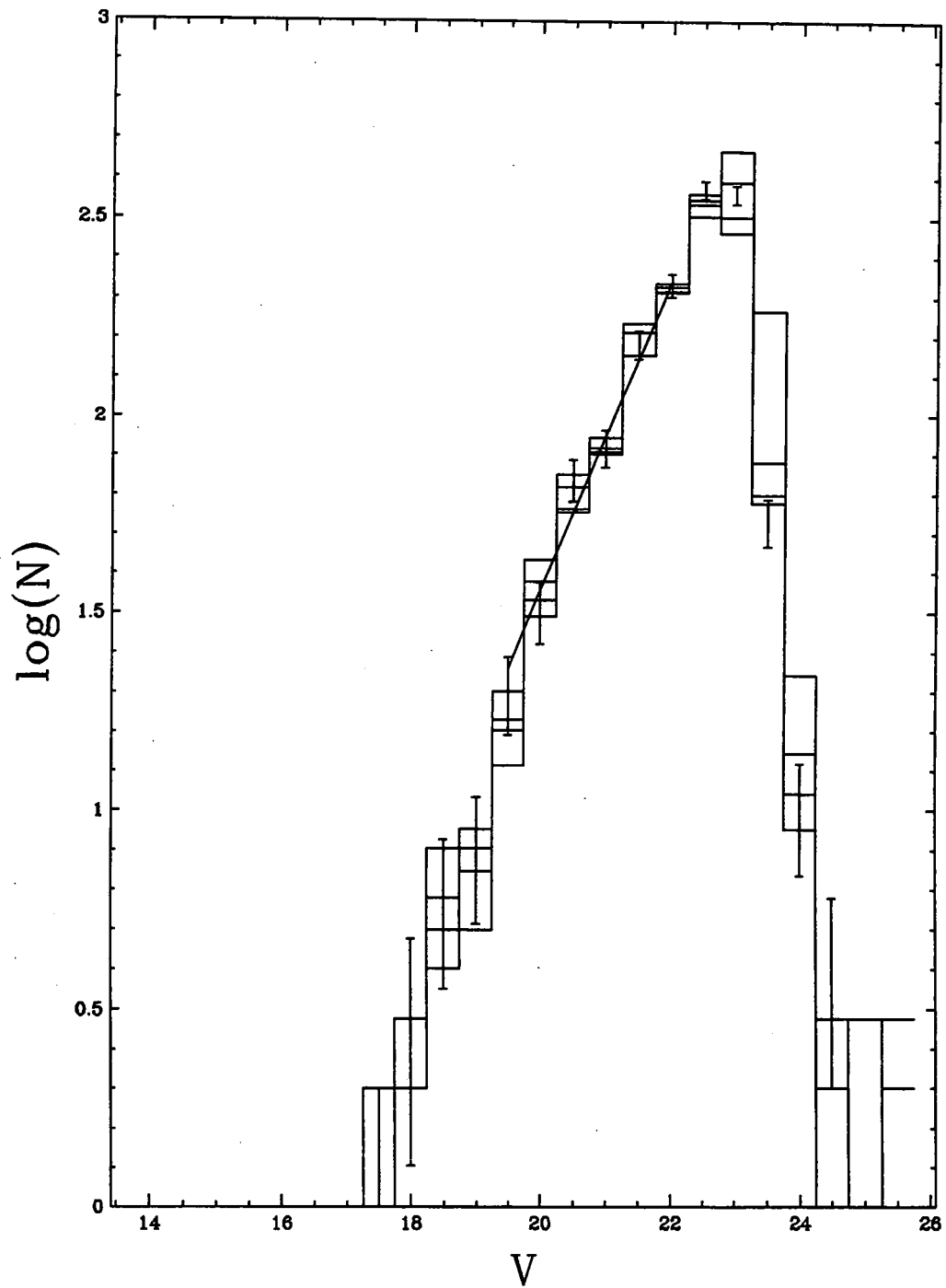
Figure 4.8: Field number counts for 4 V-band AAT frames. The error bars for one frame are shown. Also shown is the best fit line to the counts with slope of 0.392. For errors to this line see Figure 4.9.
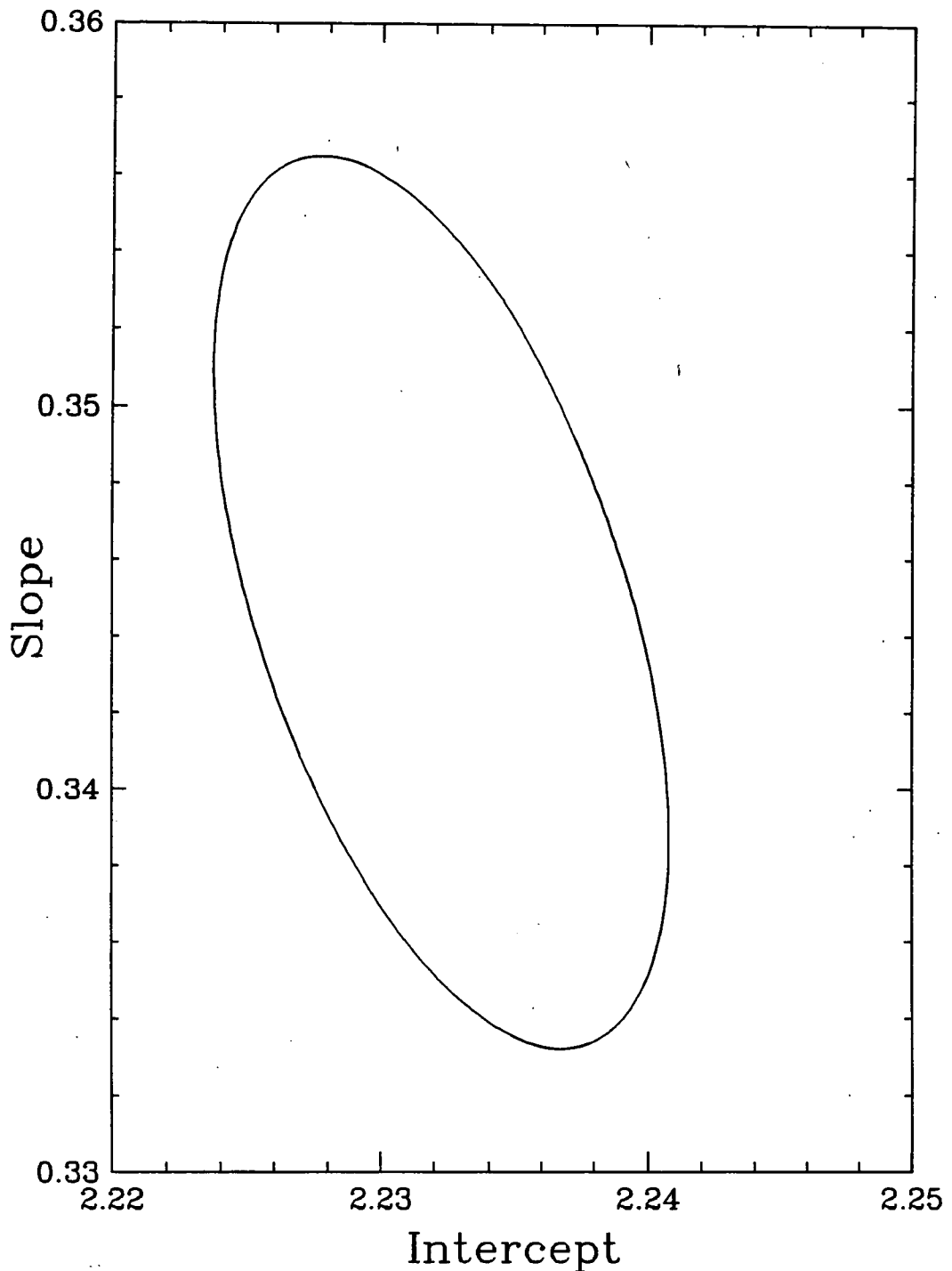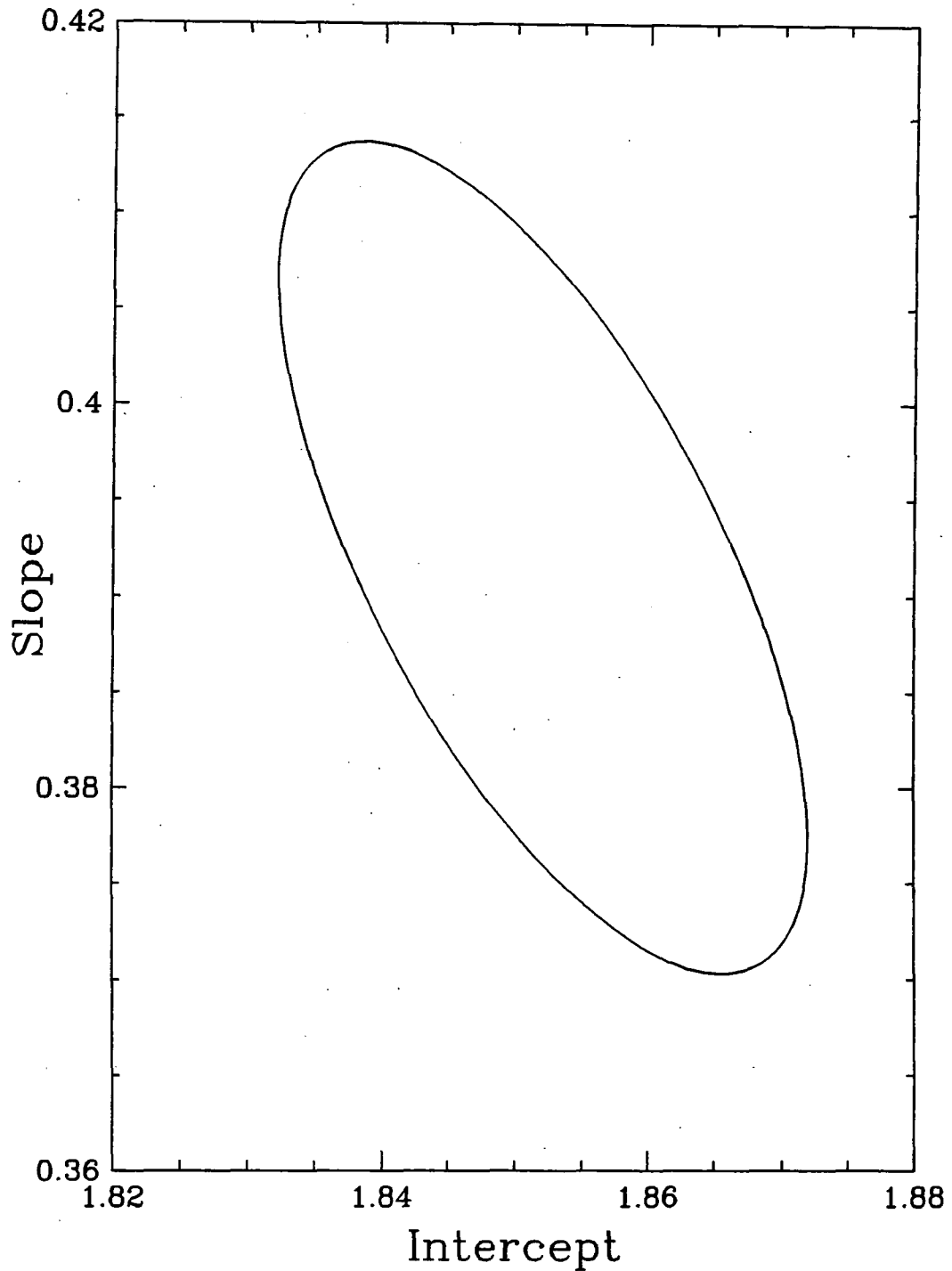
Figure 4.9: The error contour for the V field counts fit. The contour is $\chi^2_{\min} + 2.3$ which corresponds to a 68% confidence ellipse for normally-distributed errors. To minimise errors the origin was moved to (20.75,0) i.e. x becomes $x - 20.75$. The minimum χ^2 occurred at [1.852,0.392]. The recovered line $y = mx_{\text{new}} + c$ when reconverted yields $y = mx_{\text{old}} + (c - 20.75m)$ ie $y = 0.392x - 6.282$ as stated in the text.
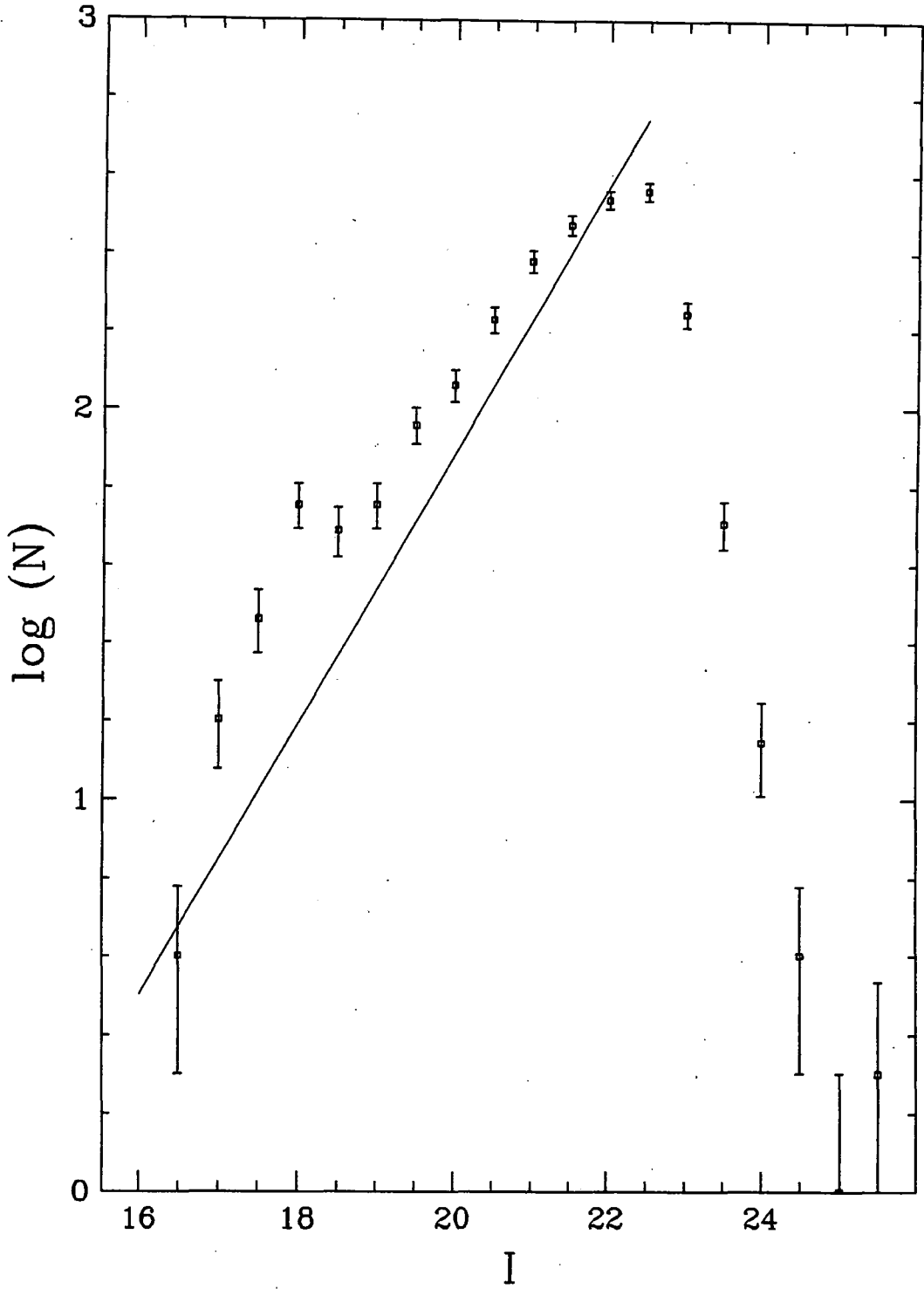
Figure 4.10: Number counts for the A1689 I exposure. The counts are per field of view area for the cluster (Table 4.1) and per 0.5 magnitude bin. The equivalent field counts from the AAT telescope are overlaid. Note the bump in the cluster counts at $I \sim 17$ associated with the onset of the bright cluster population. Stars have been removed from all the counts.
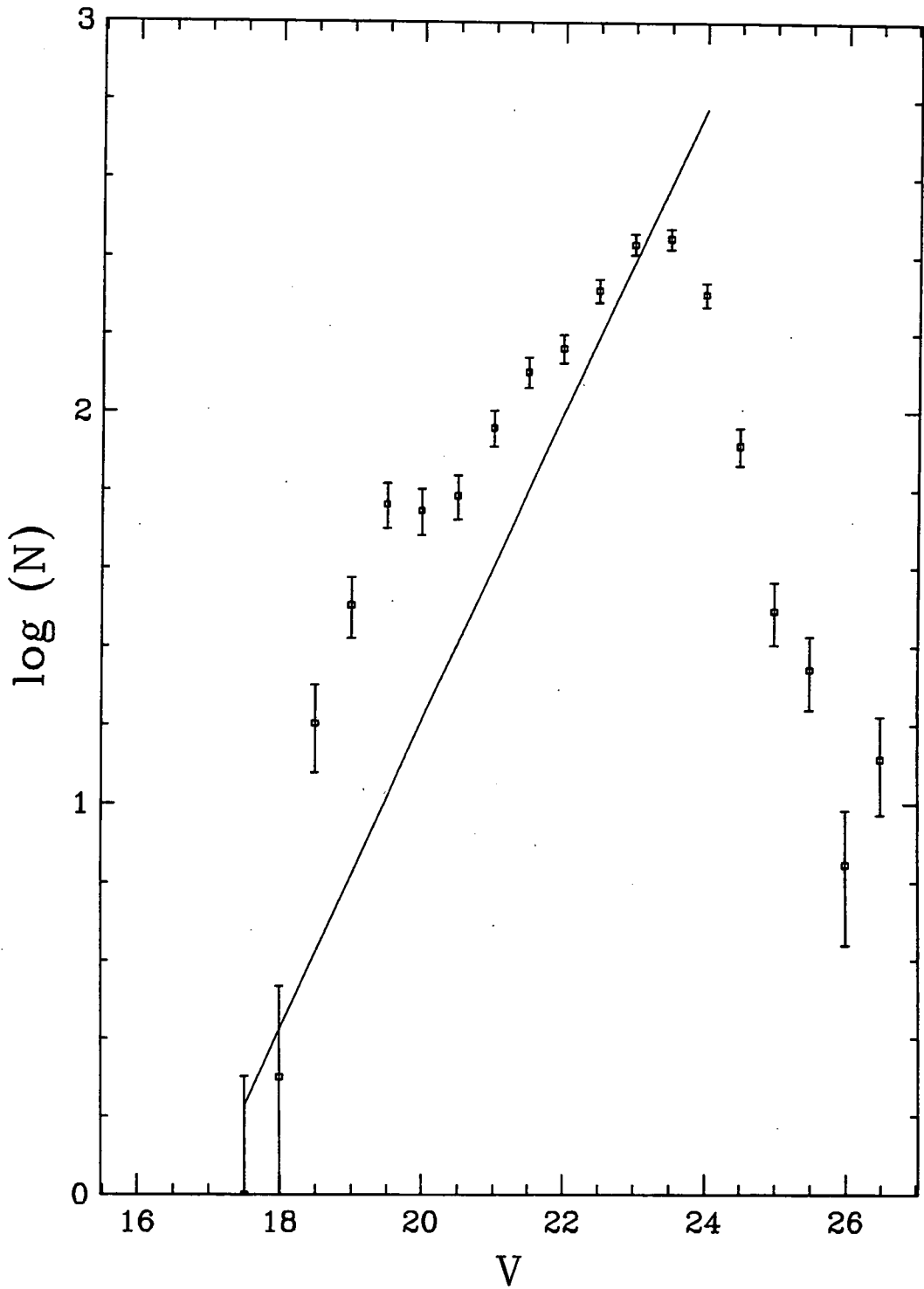
Figure 4.11: Same as Figure 4.10 but for A1689 V. Note the bump due to the cluster galaxies from $V \sim 18.5$.

A665 I
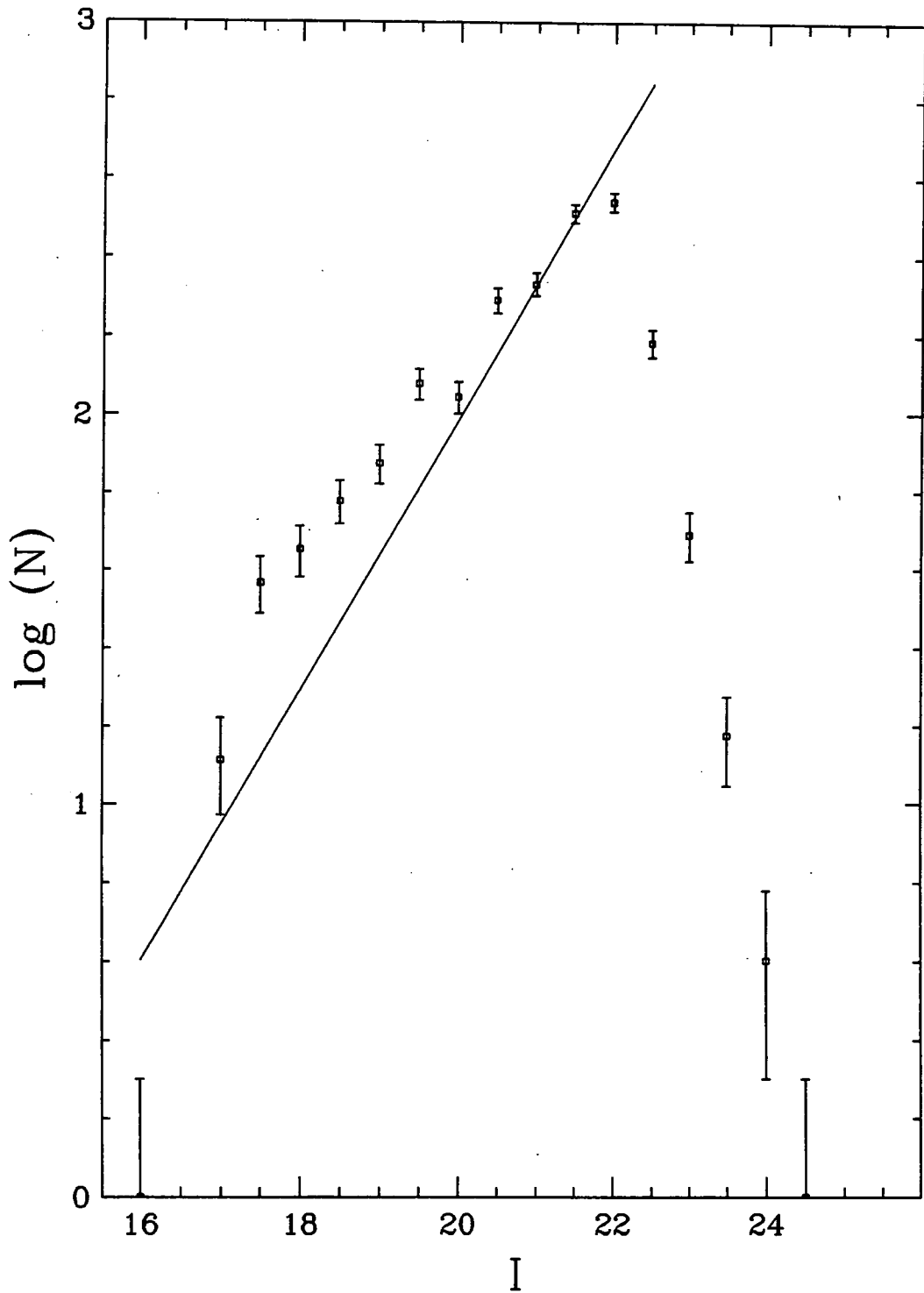
Figure 4.12: Same as Figure 4.10 but for A665 I.

A665 V
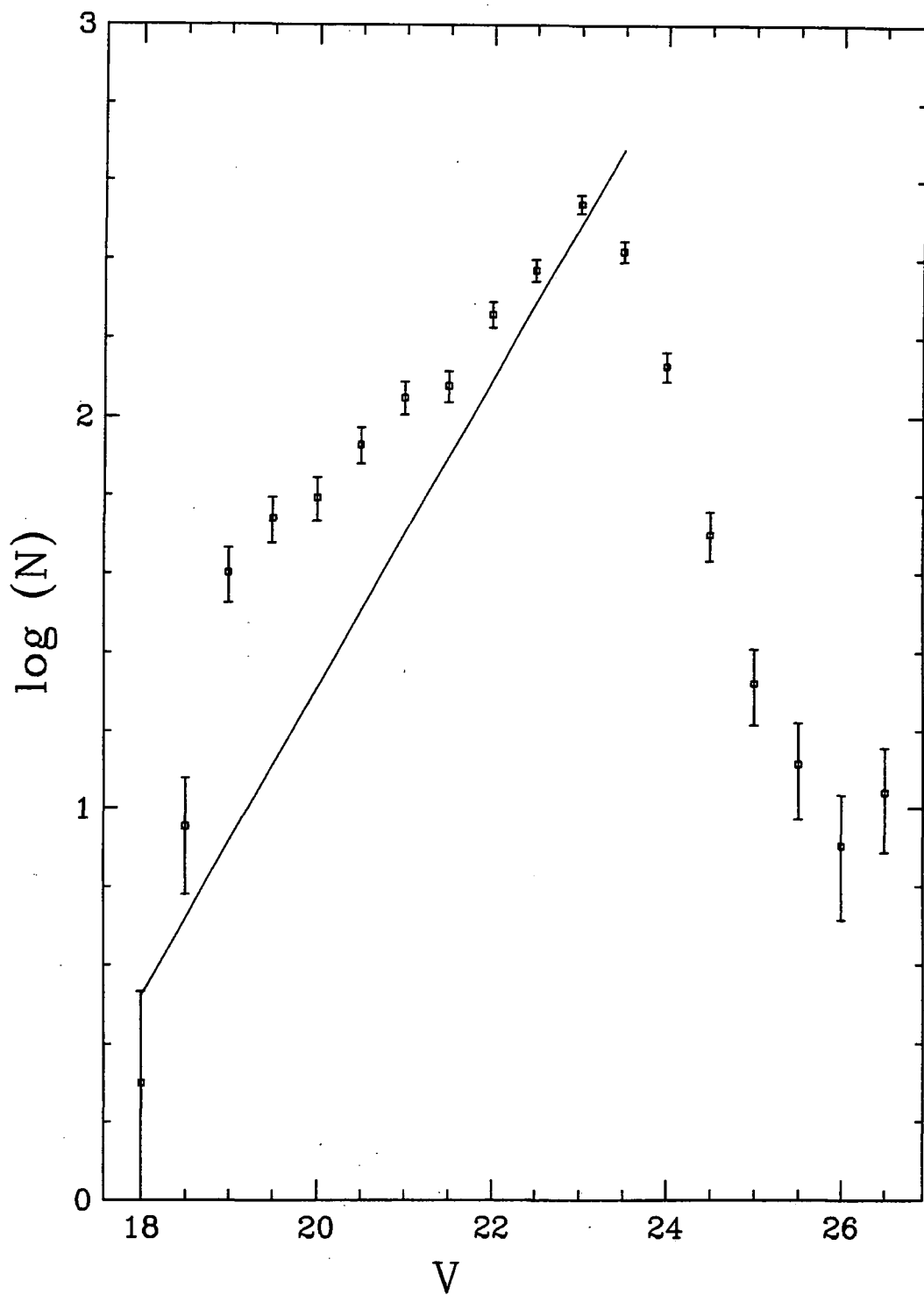
Figure 4.13: Same as Figure 4.10 but for A665 V.

A1689 I
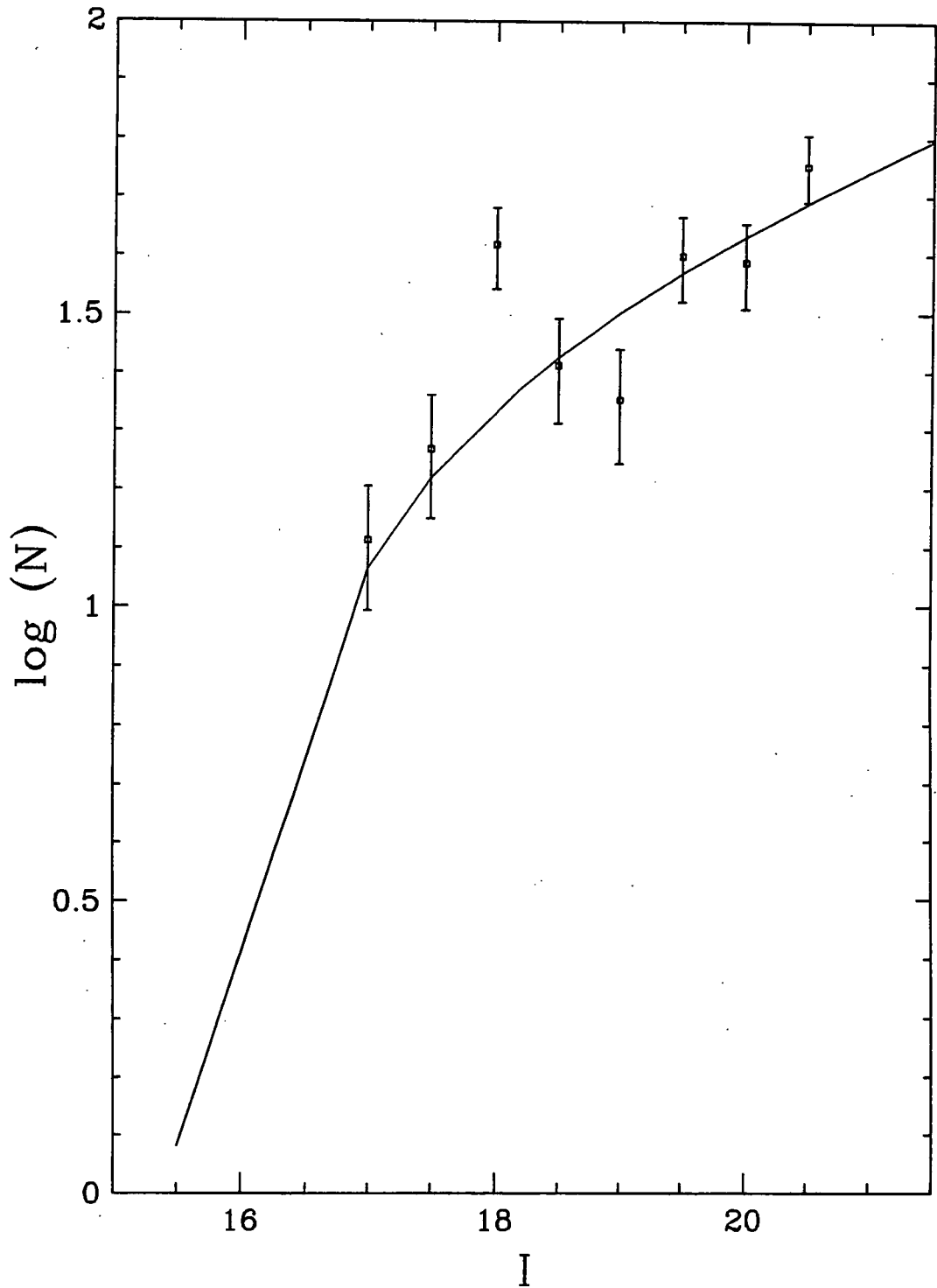
Figure 4.14: Field corrected number counts for the I observations of A1689. Overlayed is the best fit Schechter function. The parameters are given in Table 4.9.

A1689 V
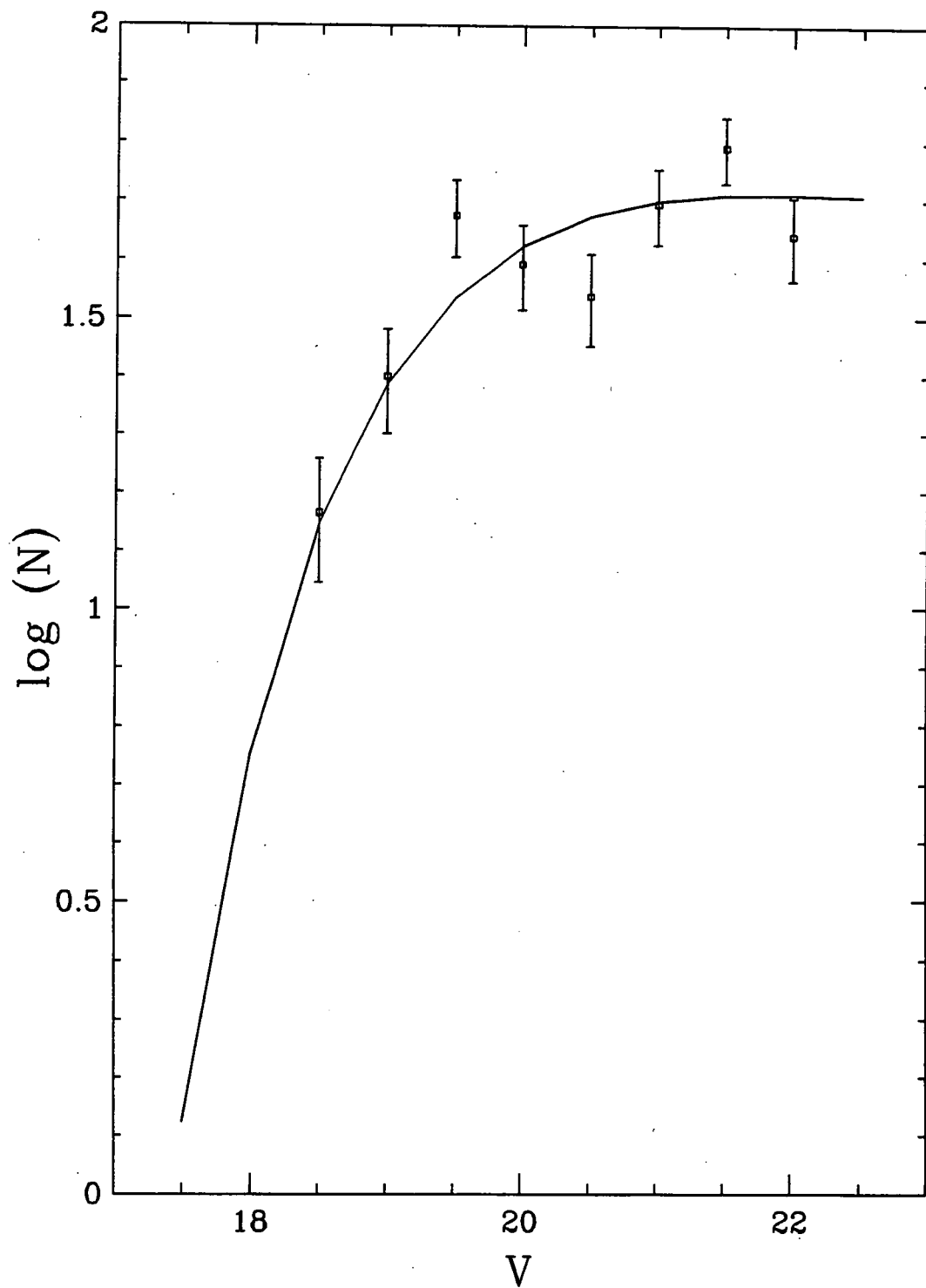
Figure 4.15: Field corrected number counts for the V observations of A1689. Over-layed is the best fit Schechter function. The parameters are given in Table 4.9.
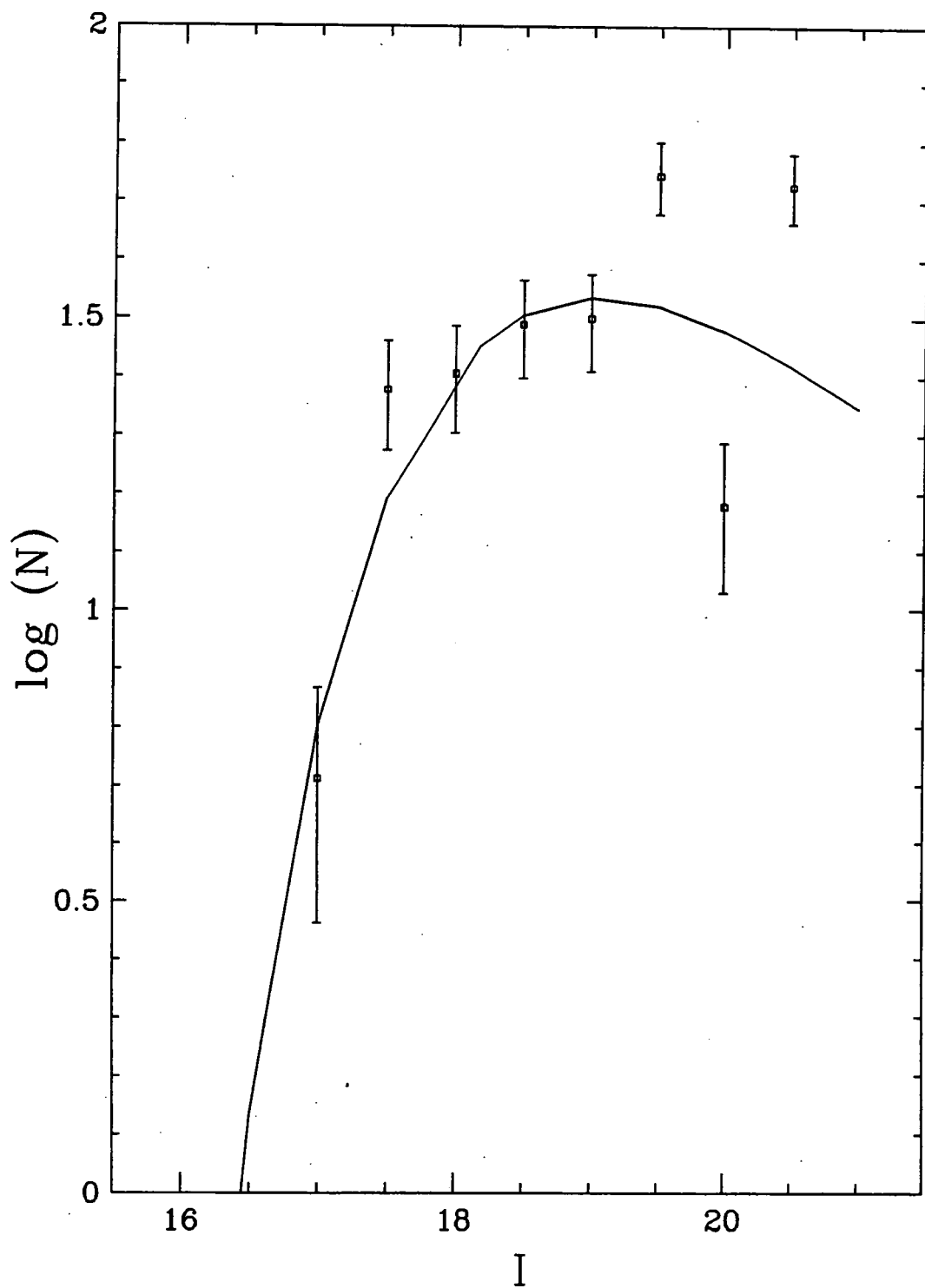
Figure 4.16: Field corrected number counts for the I observations of A665. Overlayed is the best fit Schechter function. The parameters are given in Table 4.9.

A665 V
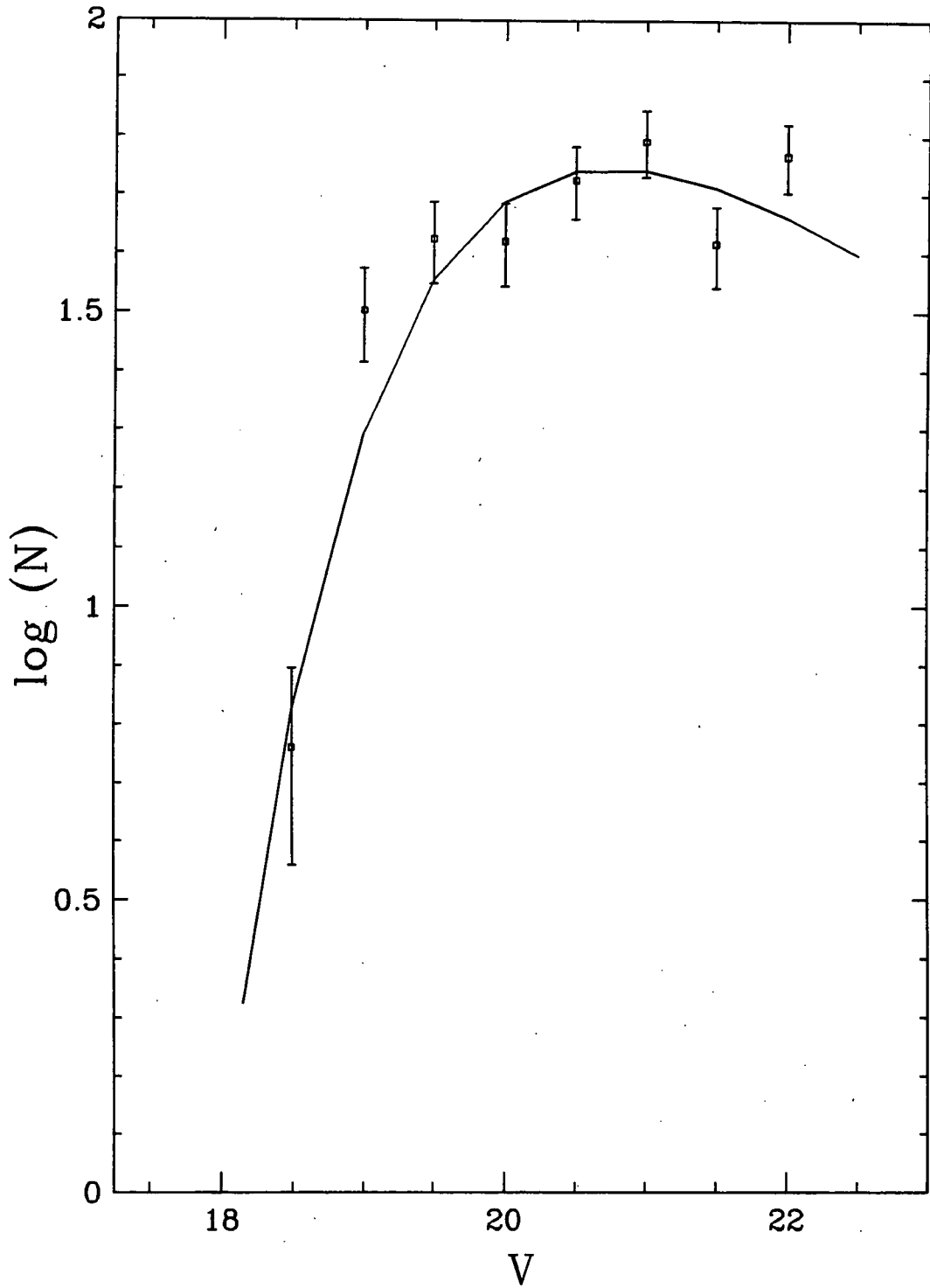
Figure 4.17: Field corrected number counts for the V observations of A665. Overlayed is the best fit Schechter function. The parameters are given in Table 4.9.

this dataset are reasonably matched to those of the primary cluster images. These data were kindly reduced and calibrated by Dr. Lidman who also provided estimates of the zero point errors of $\Delta I = 0.01$ and $\Delta V = 0.01$. We detail the observations in Table 4.2.

4.3 Analysis and Results

4.3.1 Cluster Colour-Magnitude Diagrams

To provide colour information on the detected objects in the cluster we first matched the seeing on the I and V images of each cluster, by degrading the better seeing I image to the V resolution using a Gaussian filter. We then performed standard aperture photometry within 6.0 arcsec diameter apertures using the I catalogue as a coordinate list. The resulting colour-magnitude diagrams for the two clusters are illustrated in Figures 4.4 and 4.5. A strong linear feature is visible in each diagram – this marks the colours of the dominant red cluster spheroid population.

Our cluster data thus covers a region of approximately $12' \times 12'$ or 2.8×2.8 Mpc in each cluster to a depth of $I \sim 22.5$ and $V \sim 24$. These are equivalent to $M^* + 4$ and $M^* + 5$ at the cluster redshift.

Although it would be possible to use these colour-magnitude diagrams to identify cluster galaxies by colour at the bright end, this is not possible at the faint end. Instead we remove the foreground field galaxies statistically.

4.3.2 Are Faint Galaxies Being Missed?

To test the sensitivity of our object detection algorithm to the surface brightness limit we also catalogued our cluster frames using a procedure similar to that adopted by DPDMD in their analysis of A963. We selected a low surface brightness limit, 1.0σ of the sky noise, with the understanding that the ensuing sample would be strongly contaminated by noise objects. This procedure detected 275 objects in the A665 I frame and 168 in the A1689 I exposure brighter than our adopted limit of $I = 22.5$ (these catalogues are termed 'low-sb'). Real objects should appear in both catalogues and have colours expected of the galaxy population $(V - I < 1.5)$.

To determine the excess number of real objects not detected with our standard procedure we first removed all those objects from the low-sb I catalogues which occurred in the standard versions of the catalogues. Since we were attempting to find previously undetected objects in our clusters, we then performed aperture photometry of the remaining objects in the V exposures. The reddest galaxies expected at $z = 0.18$ will correspond to the spheroidal populations of the clusters. These place a limit of $(V - I) < 1.5$ on the colours of the galaxy populations at

$z = 0.18$. With our limiting magnitude of $I = 22.5$ this means that cluster galaxies should have V colours ≤ 24. That is to say all the 'real' low surface brightness cluster members in the filtered low-sb catalogues should be detected brighter than $V = 24$ using aperture photometry on the V images. The number of objects from the low-sb catalogues which are brighter than $I = 22.5$, are undetected using the standard algorithm and yet have V magnitudes brighter than $V = 24$ is 48 in A665 (2.7% of the population) and 128 in A1689 (7% of the population). These proportions are negligible and so we conclude that our standard object algorithm is not significantly biasing the object catalogue against low surface brightness cluster members, in so far as our data can detect them.

4.3.3 Field Catalogues

We analysed the AAT imaging data as in Section 4.2.5, with equivalent selection criteria, We produced the catalogues detailed in Table 4.4. This field survey provides adequate statistics for number counts as faint as $I \sim 22$ and $V \sim 23$, close to the limiting magnitudes of our cluster datasets. Again, we remove the stars by plotting isophotal radius versus magnitude. In the analysis which follows we have chosen to fit a straight line to the observed field counts, and use these fits to correct the cluster data for field contamination, extrapolating slightly where needed. We used a maximum-likelihood method to determine the slope and intercept of the straight line. We employed the generalised chi-squared statistic,

$$\chi^2 = \sum_i \left(\frac{\log_{10} N_O(i) - \log_{10} N_E(i)}{\sigma(i)} \right)^2, \tag{4.5}$$

where $N_E(i)$ is the expected number of galaxies in the i'th bin, $N_O(i)$ is the observed number. $\sigma(i)$ is the Poissonian-based error for each bin, namely,

$$\sigma(i) = \log_{10} N - \log_{10}(N - \sqrt{N}) \tag{4.6}$$
$$= |\log_{10}(1 - \frac{1}{\sqrt{N}})| \tag{4.7}$$

We obtained the following fits (per field frame area ie 270 arcmin^2 per 0.5 magnitude):

$$\log_{10} dN = 0.345I - 4.665, \quad I \in [19.0, 21.0] \; (\chi^2_{\min} = 122.6 \,, \; 45 \, \text{points})$$
$$\log_{10} dN = 0.392V - 6.282, \quad V \in [19.5, 22] \; (\chi^2_{\min} = 33.2 \,, \; 24 \, \text{points})$$

Then the differential counts per degree^2 per 0.5 magnitude are:

$$\log_{10} dN = 0.345I - 3.540, \ I \in [19.0, 21.0] \ (\chi^2_{\min} = 122.6 \,, \ 45 \,\text{points})$$
$$\log_{10} dN = 0.392V - 5.158, \ V \in [19.5, 22] \ (\chi^2_{\min} = 33.2 \,, \ 24 \,\text{points})$$

We list the counts as a function of magnitude in Tables 4.5 and 4.6. The differential count slopes are in reasonable agreement with those published by previous workers (Driver et al. 1994; Smail et al. 1995) and shown in Table 4.7.

We show in Figure 4.6 and 4.8 the field counts and best-fit line. The 68% confidence error contours are shown in Figures 4.7 and 4.9. The plots have been created by calculating χ^2 for points on a slope-intercept grid. The value of χ^2 for points within the contour exceeds the minimum value of χ^2 by less than 2.3.

In Figures 4.10 to 4.13 we show our adopted field counts (the straight line) overlayed on the observed counts in the cluster fields. A large excess of galaxies at bright magnitudes is apparent in both clusters, although as we reach fainter this excess apparently diminishes until by $I \sim 21$ it is not readily discernible.

4.3.4 Measuring the Luminosity Functions

Having the differential number counts in V and I in both our cluster and comparison fields, we then proceeded to study the luminosity functions in our two clusters. Using the differential galaxy counts from our cluster and field surveys we simply subtracted one from the other to provide the magnitude distribution for the galaxies in each cluster. We again used the maximum-likelihood method, based on chi-squared, to measure the α, $M^\star$ and $N^\star$ parameters in the Schechter function in equation (4.3). The generalised chi-squared statistic used was as in equation 4.5. As a simple conservative estimate of the errors, we take

$$\sigma(\text{i}) = [(\max[N_O^{\max}(\text{i}) - N_O(\text{i}), N_O(\text{i}) - N_O^{\min}(\text{i})])^2 + (\sqrt{N_O(\text{i})})^2]^{\frac{1}{2}} \qquad (4.8)$$

where $N_O(\text{i})$ is the observed number of cluster galaxies after field subtraction. The first term in the expression for $\sigma(\text{i})$ takes account of possible errors in $N_O(\text{i})$ arising from errors in the slope and intercept of the the field line. The second term is the Poissonian error in the cluster counts. Maximum and minimum values of $N_O(\text{i})$ were calculated using the 68% confidence limits (Figures 4.7 and 4.9).

The luminosity functions are plotted in Figures 4.14 to 4.17. The best fit values of the Schechter parameters are shown in Table 4.9. In an effort to avoid incompleteness effects in the counts causing us to underestimate the slope, the faintest bin used in the fit is at least one magnitude brighter than the count turnover value.

As the Schechter function involves three parameters, the confidence contours are three-dimensional shapes. Figures 4.18 to 4.21 show one slice through each 3-D

contour shape ($N^\star$ is held fixed at its most likely value). Ellipses corresponding to $\chi^2_{min}+1$, $+2$, $+3$ and $+4$ are marked. In spite of the rather large errors we conclude that there is no evidence for an upturn to the Schechter function fits at the faint end to the depth of magnitude that we have been able to probe.

In Figure 4.22 we again show our A1689 V data with Driver's A963 R data displaced and overlaid (the dotted points and errorbars). We employ a combined $V - R$ colour and distance modulus magnitude displacement of 0.4, and also an empirical normalisation correction. As can be seen from the figure, although our data does not show any indication of an upturn, it also does not probe the faint end of the luminosity function to the same depth as Driver et al. It would be necessary to extend the luminosity function of A665 and A1689 by at least one more magnitude before strong conclusions could be drawn.

4.3.5 Comparison Check

Finally, we determined a crude estimate of the cluster luminosity function which was entirely independent of the magnitude scales. Here we took advantage of the large field of view available in our clusters and the strongly peaked distribution expected for galaxies bound to the cluster potential. We split our cluster frames into two independent radial bins, each containing the same area of chip. For the various images this translated into radii of ~ 1 Mpc . We then simply subtracted the differential counts in the outer region from those in the inner one. This removed all galaxy populations which had a flat distribution across the image i.e. the field population, and left only the cluster galaxies. We show the results of this analysis in Figures 4.23 to 4.26. These show no evidence for a steeply rising faint end component. We reiterate that as a differential test this is not affected by a uniform zero-point magnitude error and is sensitive to any population of clustered galaxies centred on the cluster center. While we cannot totally reject the presence of a rising faint component to the cluster luminosity function it would have to a have a spatial distribution which is close to flat across the cluster.

4.4   Conclusions

• We have presented deep I and V photometry of A1689 and A665, two rich, X-ray luminous clusters at $z = 0.18$. This photometry reached a limiting apparent magnitude of $I = 22.5$, equivalent to an absolute magnitude of $I = -17.5$, or $M^\star+5$, at the cluster redshifts. We analysed the data to provide differential number counts of galaxies in the fields of these two clusters.

• We also presented equivalent I and V observations of blank sky regions from which we derived the galaxy number counts expected in our cluster fields in the absence of the clusters.

• We used the field survey to remove the field contamination from our cluster fields. The resulting magnitude distribution was due to the cluster galaxies. We also showed results of a similar crude test which was independent of the photometric zero points of our datasets.

• The cluster luminosity functions we derived showed no upturn in their slopes at the faint end. Thus we found no evidence in either of our clusters, to the magnitude depth we were able to probe, for a steeply increasing population of faint member galaxies.

Figure 4.18: Error contours for the A1689 I Schechter fit. The contours are $\chi^2_{min}+1$, +2, +3, +4.
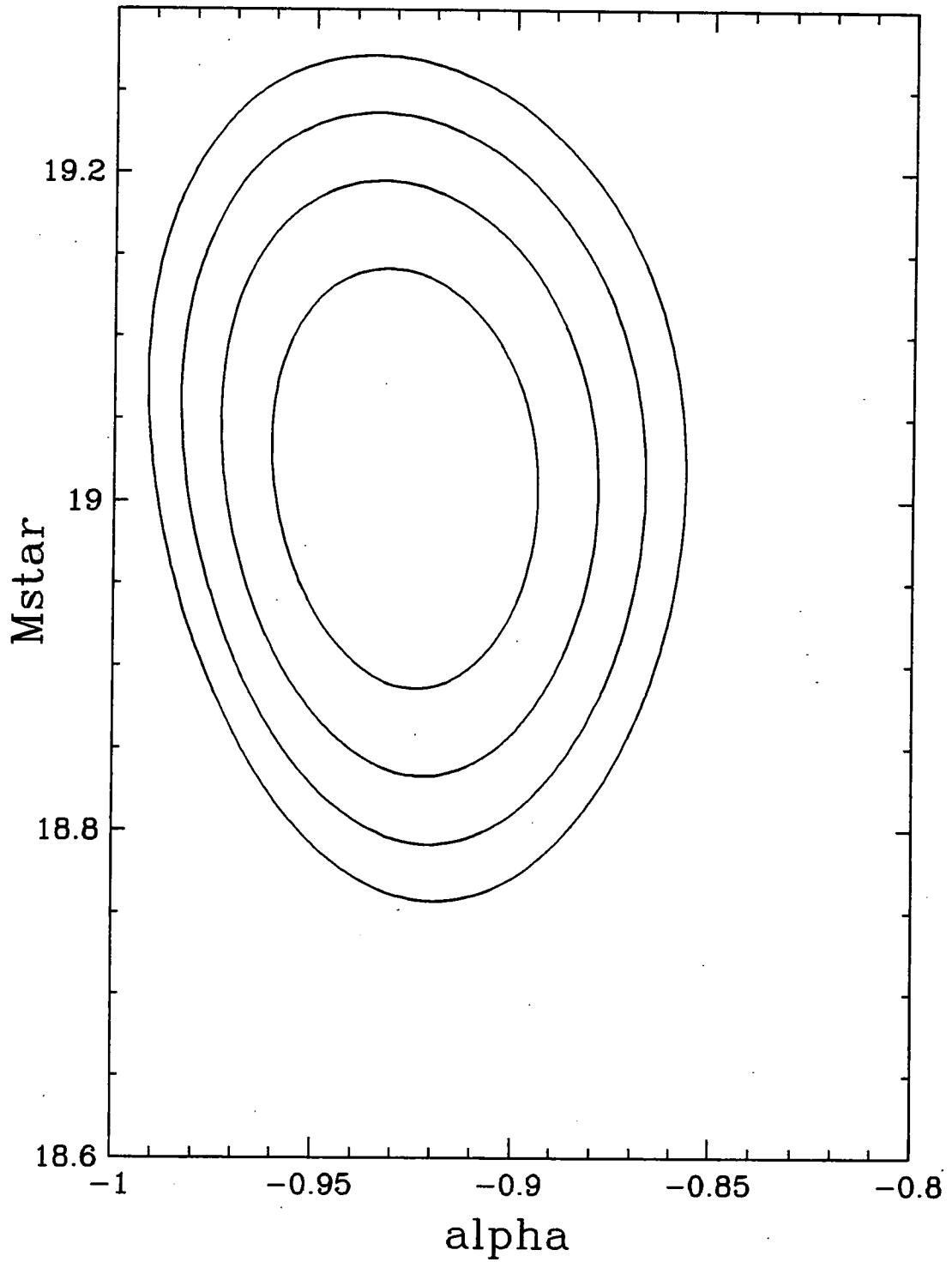
A1689 V

Figure 4.19: Error contours for the A1689 V Schechter fit. The contours are $\chi^2_{min}+1$, +2, +3, +4.
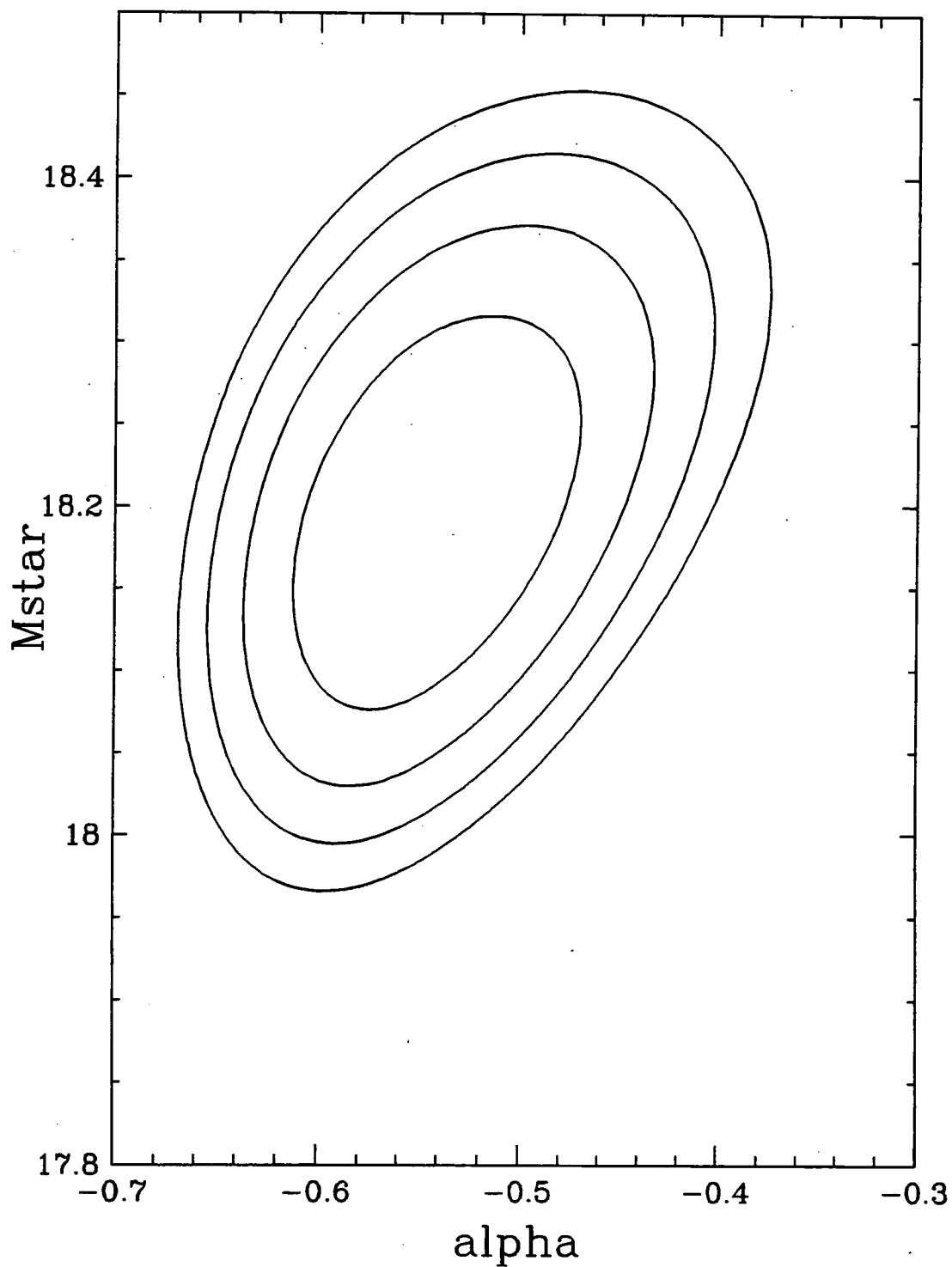
Figure 4.20: Error contours for the A665 I Schechter fit. The contours are $\chi^2_{min}+1$, +2, +3, +4.
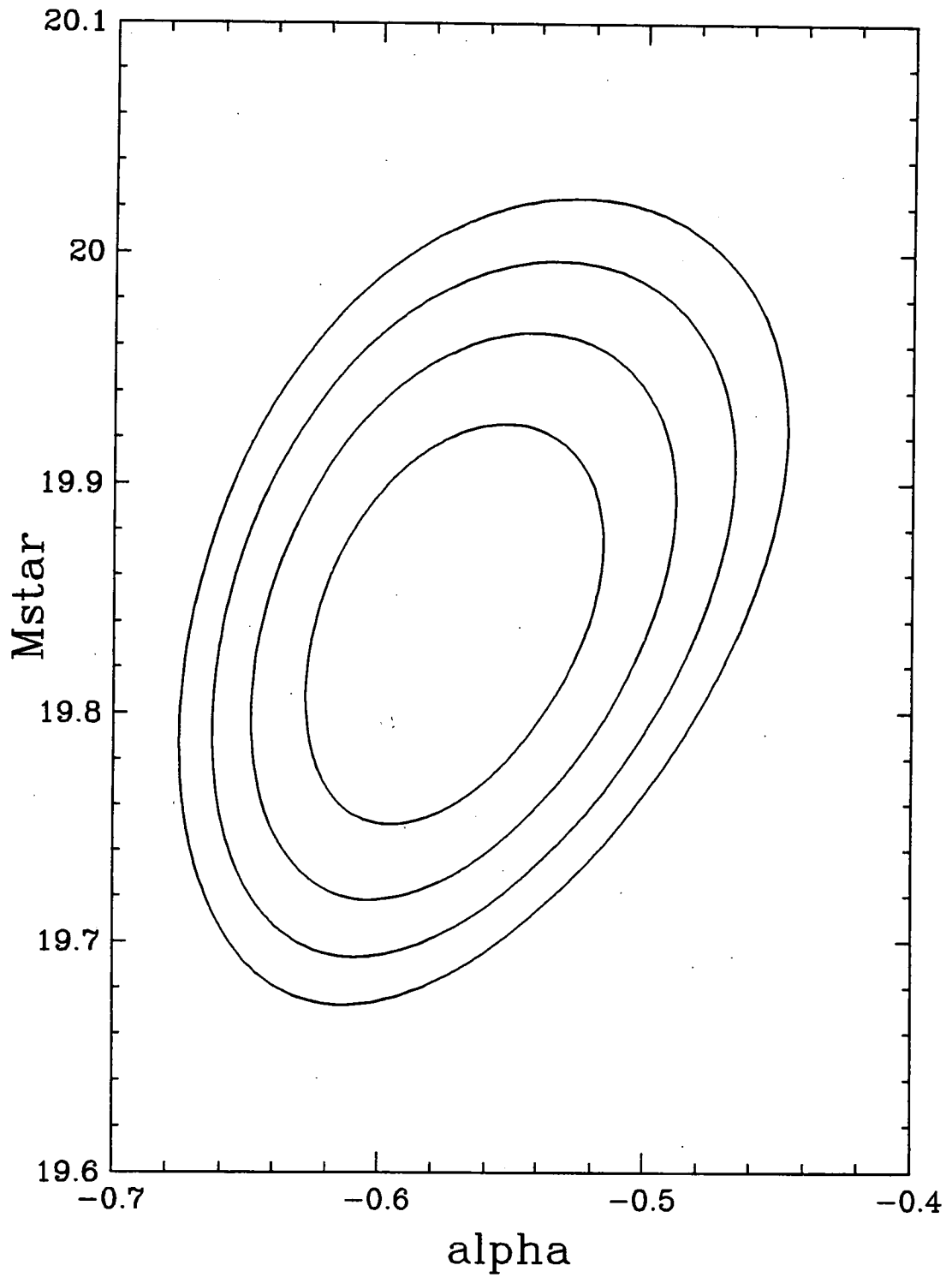
Figure 4.21: Error contours for the A665 V Schechter fit. The contours are $\chi^2_{\min}+1$, $+2$, $+3$, $+4$.
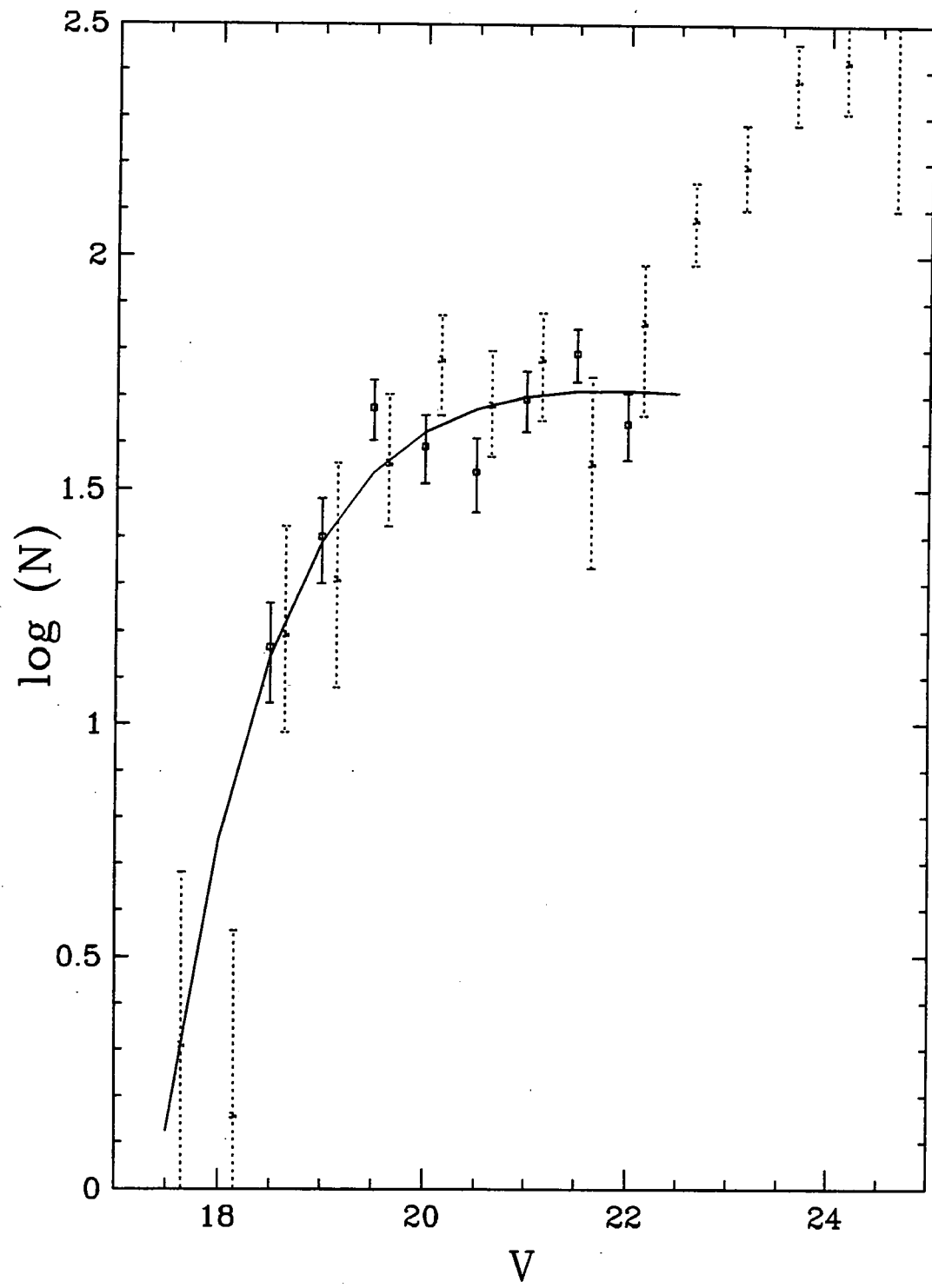
Figure 4.22: The solid line and points show our A1689 V data, as in Figure 4.15. The dotted points and error bars show data from Driver at al. (1994) for cluster A963. (The A963 data has been scaled as described in the text).

A1689 I
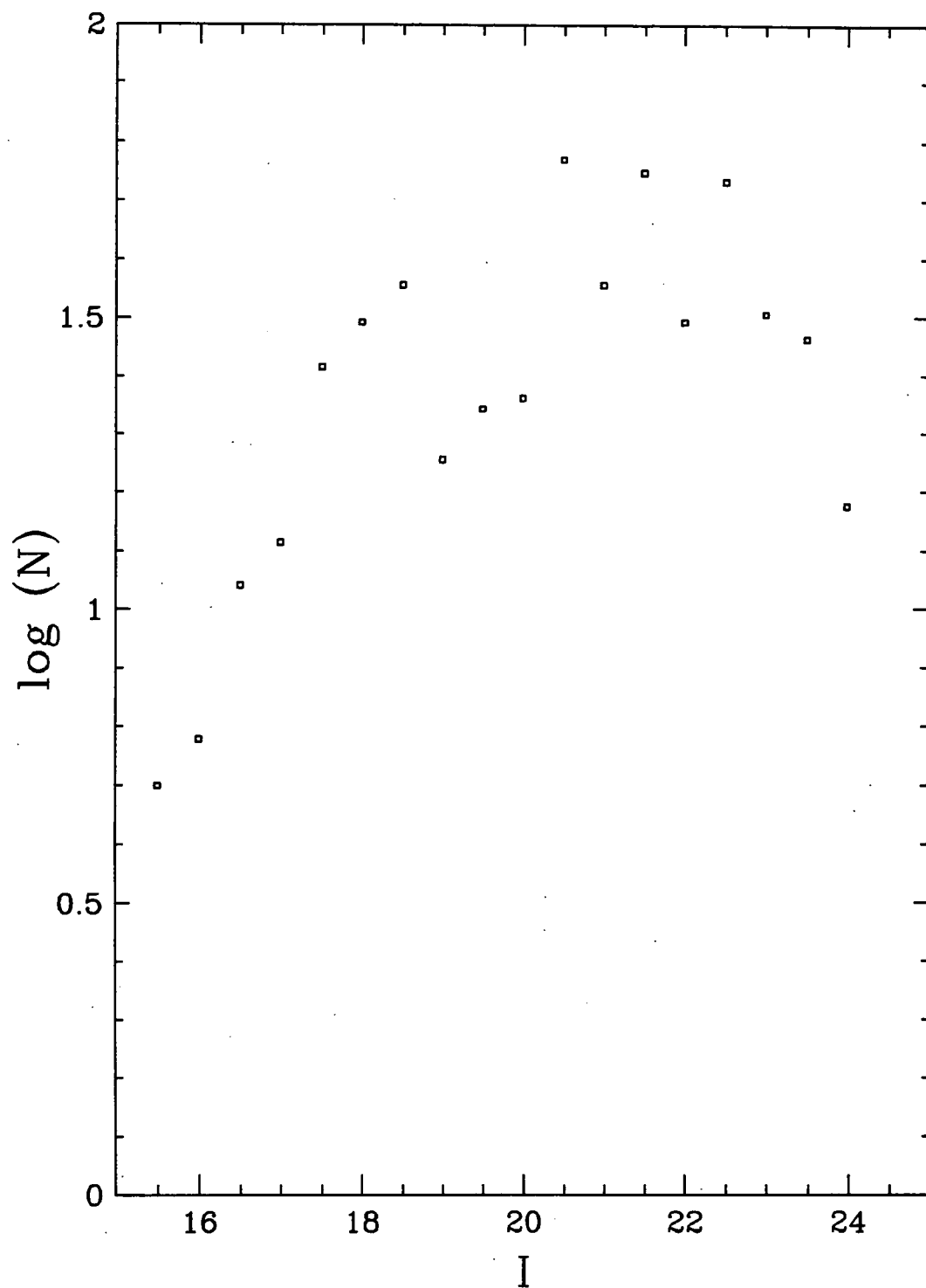
Figure 4.23: Differential counts in *I* between the central and outer regions in A1689. The boundary is at 4.32 arcmin (1.0 Mpc). The error bars are large and are not shown here.

A1689 V
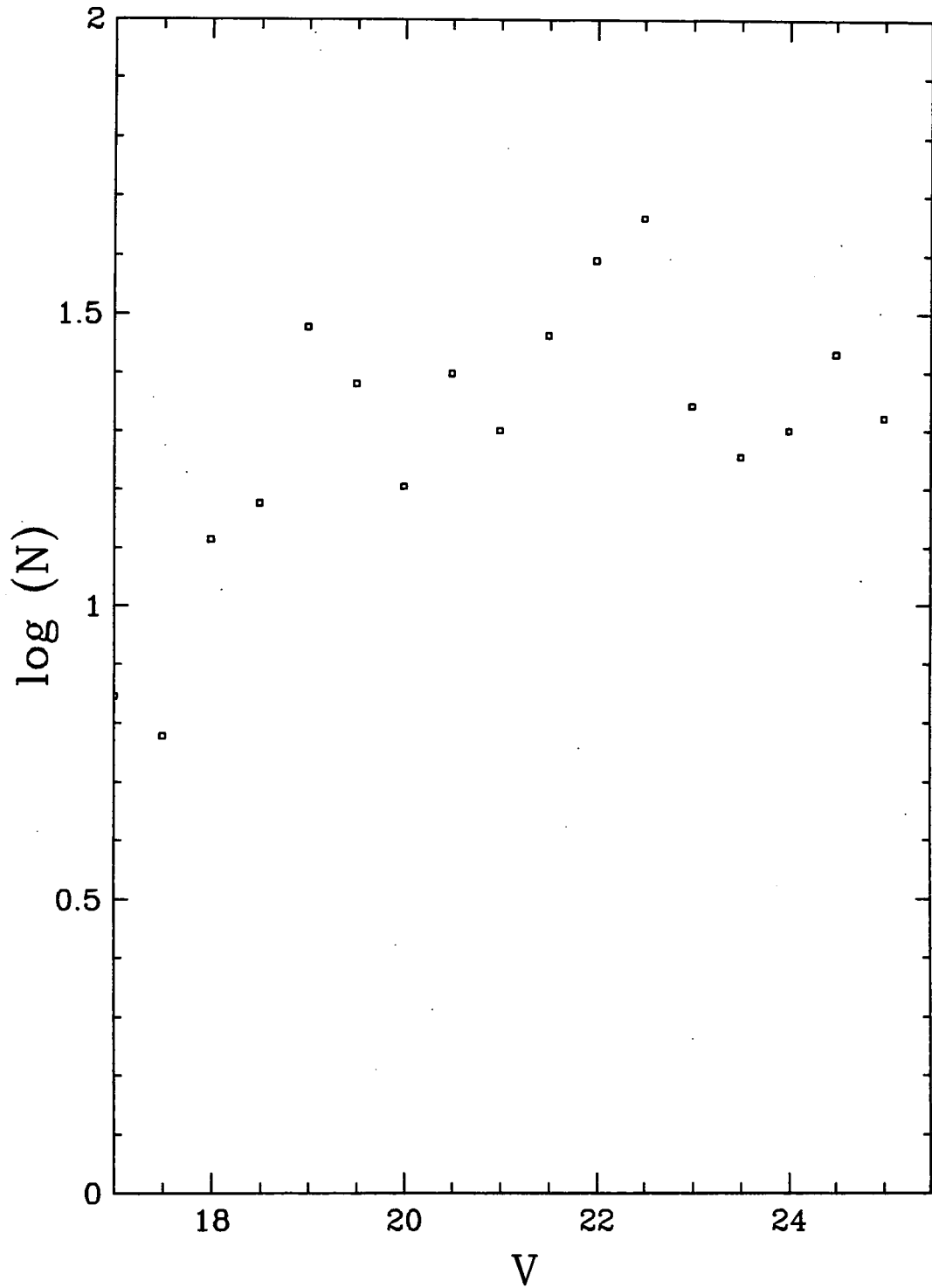
Figure 4.24: As for Figure 4.23 but for the V band.

A665 I
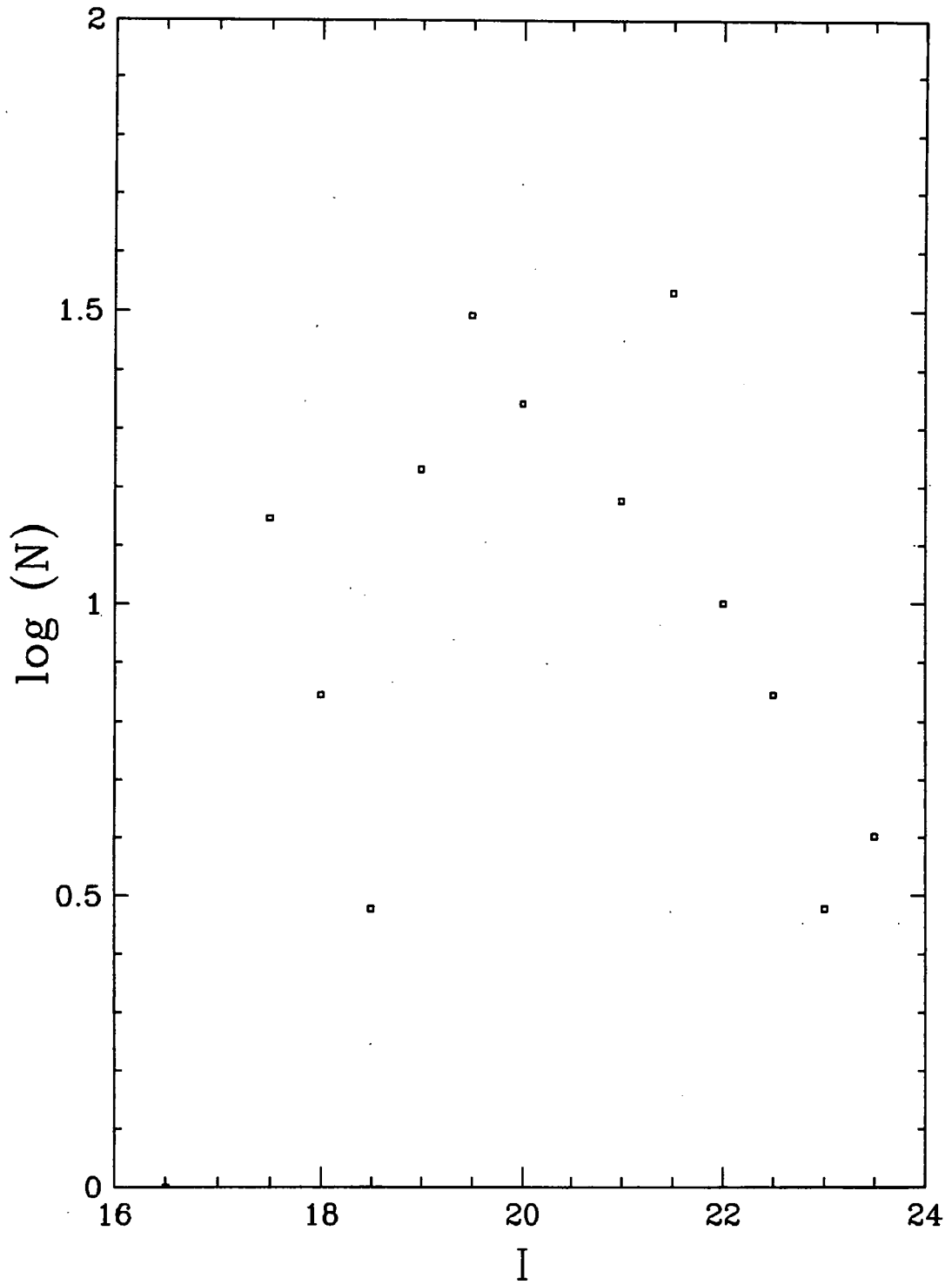
Figure 4.25: Differential counts in *I* between the central and outer regions in A665. The boundary is at 4.32 arcmin (1.0 Mpc).

A665 V
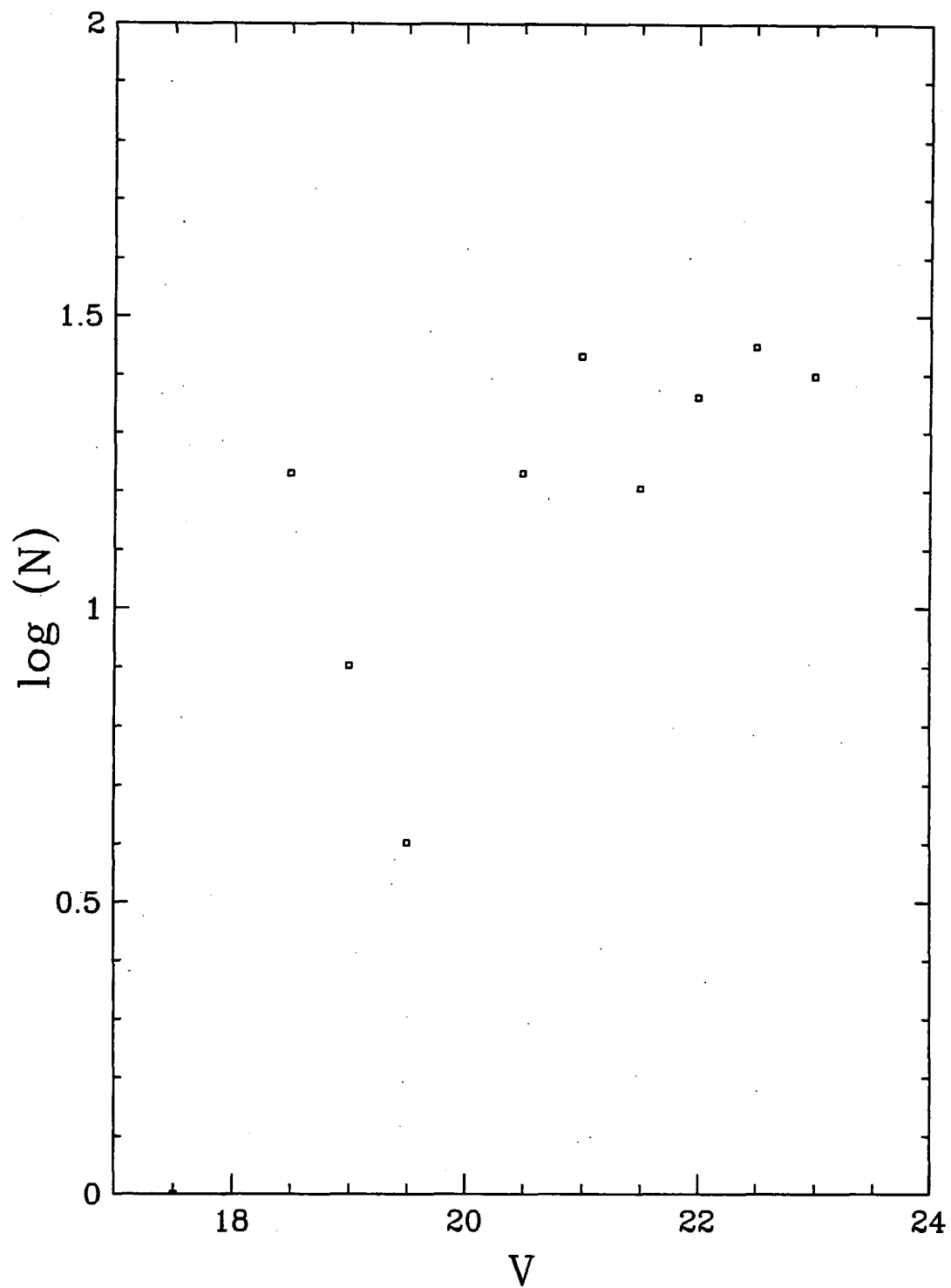
Figure 4.26: As for Figure 4.25 but for the V band.

Table 4.1: INT cluster catalogues

Target	Filter	Field	m_{lim}	N_{gal}
A1689	I	$11.29' \times 10.61'$	$\sim$21.5	2084
A665	I	$12.34' \times 12.30'$	$\sim$21.5	1769
A1689	V	$11.29' \times 10.61'$	$\sim$23.0	1703
A665	V	$12.34' \times 12.30'$	$\sim$23.0	1750

Table 4.2: AAT field catalogues

Target	Filter	Area	m_{lim}	N_{gal}
Field-I	I	$16.43' \times 16.43'$	$\sim$21.5	$\sim$2000
Field-V	V	$16.43' \times 16.43'$	$\sim$22.5	$\sim$1500

Table 4.3: INT cluster imaging data

Target	Field	Scale	Filter	T_{exp}	FWHM
A1689	$11.29' \times 10.61'$	0.37	I	9.8	1.78
A665	$12.34' \times 12.30'$	0.37	I	20.5	1.67
A1689	$11.29' \times 10.61'$	0.37	V	18.0	2.08
A665	$12.34' \times 12.30'$	0.37	V	17.0	1.97

Table 4.4: AAT field imaging data

Target	Field	Scale	Filter	T_{exp}	FWHM
1041$-$07	$16.43' \times 16.43'$	0.98	I	0.9	2.0
1041+06	"	0.98	I	0.9	2.0
1041+20	"	0.98	I	0.9	1.8
1042$-$08	"	0.98	I	0.9	1.9
1042+20	"	0.98	I	0.9	1.9
1044$-$03	"	0.98	I	0.9	2.0
1043$-$01	"	0.98	I	0.9	2.1
1342+09	"	0.98	I	0.9	1.9
1343+09	"	0.98	I	0.9	2.0
1041+06	$16.43' \times 16.43'$	0.98	V	1.1	2.4
1041+20	"	0.98	V	1.1	2.6
1042$-$08	"	0.98	V	1.1	2.2
1341$-$20	"	0.98	V	1.1	2.4

Table 4.5: AAT I field counts

Magnitude	Counts [deg^{-2} (0.5 mag)$^{-1}$]
20.0	2300
20.5	3400
21.0	5000
21.5	7500
22.0	11200
22.5	16700
23.0	24800
23.5	36900
24.0	55000

Table 4.6: AAT V field counts

Magnitude	Counts [deg^{-2} (0.5 mag)$^{-1}$]
20.0	480
20.5	760
21.0	1200
21.5	1900
22.0	2900
22.5	4600
23.0	7200
23.5	11300
24.0	17800

Table 4.7: Comparison of field slopes

Source	Filter	Slope	Error	Range
Driver	I	0.34	0.03	19.0-22.5
Smail	I	0.271	0.009	19.5-25.5
Lidman AAT	I	0.345	0.01	19.0-21.0
Driver	V	0.41	0.01	20.5-23.0
Smail	V	0.404	0.015	22.0-24.25
Lidman AAT	V	0.392	0.02	19.5-22.0

Table 4.8: SExtractor parameter fits

Cluster	Filter	Smooth?	Minimum Area	Threshold Above Background
A1689	I	Y	6	2.5
A665	I	Y	6	2.0
A1689	V	N	6	1.7
A665	V	Y	6	1.5

Table 4.9: Schechter function parameter fits

Cluster	Filter	α	$m^\star$	$M^\star$	$N^\star$	χ^2	Points
A1689	I	-1.25	16.52	-23.98	43	14.93	7
A665	I	-0.55	18.19	-22.31	168	36.9	7
A1689	V	-0.93	19.01	-21.81	145	10.6	7
A665	V	-0.58	19.83	-20.99	266	13.79	7

Chapter 5

Conclusions

In this thesis we have studied a number of aspects of rich clusters of galaxies. Our primary interest was in utilising the information contained in the shapes of background galaxies which had been distorted, however weakly, by these extremely massive systems. We performed a series of experiments to assess the reliability of the statistical technique proposed by Kaiser & Squires (1993) to reconstruct the surface mass overdensity in clusters. Firstly, we tested the KS method on a realistic cluster mass distribution, typical of those expected in an $\Omega_0 = 1$ universe. By simulating data from standard observing conditions, we investigated the effects of seeing and signal-to-noise ratio on the reconstructed dark matter maps and we explored how the results varied with different assumptions concerning the distributions of intrinsic galaxy shapes and redshifts.

- A careful analysis of simulations of data obtained in standard observing conditions showed that the KS method provides a remarkably faithful reconstruction of the morphology of a complex cluster, reproducing the richness of structure expected in an $\Omega_0 = 1$ universe.

- Our simulations showed that the weak lensing assumption on which the KS technique is based began to break down when the mass surface overdensity exceeded 10% of the critical surface density. However, even when it equals 30% of the critical value, the KS method underestimated the surface overdensity by only $\sim 25\%$. The noise in the reconstructed maps agreed surprisingly well with a simple estimate (equation 2.15) of the uncertainties due to Poisson noise and to the scatter in the intrinsic ellipticities of the lensed background galaxies.

- The simple calibration procedure for CCD images which we designed and tested, efficiently corrected for the effects of atmospheric seeing on the reconstructed mass surface overdensity maps. This procedure is straightforward to apply to CCD data and yields a multiplicative "compensation factor", f, which allows the true surface overdensity in each pixel (in units of the critical density) to be recovered from the reconstructed map. The *absolute* value of the lens mass cannot be derived by this method unless the critical density, which depends on the redshift distribution of the

120

lensed galaxies, is known. However, the dependence on redshift is fairly weak.

• Our method for calculating the compensation factor was quite robust. We discovered that the value of f was primarily determined by the seeing, but the depth of the CCD image and the intrinsic properties of the lensed galaxies also affected it. Useful results can be obtained even with data acquired in seeing as large as 1.6 arcseconds, although the technique clearly works best with sub-arcsecond seeing. Our simulations indicated that it should work well when applied to data obtained in a wide range of observing conditions, allowing useful mass reconstructions to be made even when the correction factor is as large as $f = 2$.

Having modelled extensively observational effects and the properties of the lensed background galaxies and satisfied ourselves that KS worked extremely well under reasonable assumptions, we then turned our attention to the lenses themselves. Evrard et al. (1994) had suggested from their simulations of cluster formation, that cluster morphologies could be used as constraints on the cosmological "constants", Ω_0 and λ_0. Evrard et al. simulated cluster formation in three cosmologies:-

1. A biased Einstein-de Sitter model ($\Omega_0 = 1$, $\lambda_0 = 0$)

2. An unbiased open model with $\Omega_0 = 0.2$ and $\lambda_0 = 0$

3. An unbiased model with $\Omega_0 = 0.2$ and $\lambda_0 = 0.8$

In agreement with analytic predictions (Richstone et al. 1992; Lacey & Cole 1993), they demonstrated that cluster evolution was sensitive to the cosmological model. In low Ω_0 models, both with and without cosmological constants, clusters form earlier and appear more regular by the present day. We decided to simulate lensing using the clusters from their three cosmologies to determine if it were possible to distinguish between the cosmologies using observations of weak lensing.

• We examined 72 simulated clusters, 24 from each of the three cosmologies.

• We simulated the gravitational lensing of background galaxies by these clusters. We used the resulting galaxy distortions to reconstruct the mass surface overdensity for each cluster. We found that although the mass overdensity was always diminished relative to the original, the general shape of the reconstructed mass distribution was usually in excellent agreement with the original.

• To quantify our discussion we introduced new statistics, D and Q which essentially measured the cluster dipole and quadrupole. These were designed to minimise the influence of the systematic uncertainties inherent in the density field reconstructed from weak lensing observations. The intrinsic distributions of D and Q were very sensitive to Ω_0 but only weakly dependent on λ_0.

• The noise present in realistic constructions of these density fields from weak lensing data added to the measured D and Q, but the Q distribution for $\Omega_0 = 0.2$ and

$\Omega_0 = 1$ remained clearly distinguishable. Thus it would be necessary to model the observing conditions but it would still be possible to constrain Ω_0. We showed that, given a sufficiently large sample of clusters, it should be relatively easy to distinguish between a low Ω_0 universe and a critical Ω_0 universe using only weak lensing techniques.

Our intention was to test our theoretical simulations with real data and we planned to measure the lensing distortion caused by A1689 and A665. Poor seeing caused us to implement our back-up project of investigating the luminosity function of these clusters. Although unconnected with gravitational lensing this is also a very interesting problem. Theoretical models of galaxy formation in hierarchical clustering models (e.g. Cole et al. 1994) predict an excess of faint galaxies over the numbers observed. However, although our errors were large, our results did not support this prediction. In summary,

- We presented deep I and V photometry of A1689 and A665, two rich, X-ray luminous clusters at $z = 0.18$. This photometry reached a limiting apparent magnitude of $I = 22.5$, equivalent to an absolute magnitude of $I = -17.5$, or $M^* + 5$, at the cluster redshifts. We analysed the data to provide differential number counts of galaxies in the fields of these two clusters.

- We also presented equivalent I and V observations of blank sky regions from which we derived the galaxy number counts expected in our cluster fields in the absence of the clusters.

- We used the field survey to remove the field contamination from our cluster fields. The resulting magnitude distribution was due to the cluster galaxies. We also showed results of a similar crude test which was independent of the photometric zero points of our datasets.

- The cluster luminosity functions we derived showed no upturn in their slopes at the faint end. Thus we found no evidence in either of our clusters, to the magnitude depth we were able to probe, for a steeply increasing population of faint member galaxies.

In the not-too-distant future, as a result of large-format CCD's becoming increasingly widespread, we can expect detailed maps of the dark matter in many clusters. Advances in detector technology mean that it is now becoming possible not only to measure the mass distribution on cluster scales but also on vastly different scales. On small scales, the distribution of dark matter in galaxy halos is being researched. Even more excitingly, on much larger scales, investigations using weak lensing are ongoing into the distribution of dark matter over many tens of Mpc's. It is apparent that weak gravitational lensing is an extremely powerful technique with a huge future. Its use offers great hope of finding clues or even answers to cosmologists' perennial questions about the origin and evolution of the Universe.

Appendix A -

Formualae for Shapes of Lensed Galaxies

From equation (2.2) in section (2.2.1),

$$\begin{pmatrix} \theta_{sx} \\ \theta_{sy} \end{pmatrix} = \begin{pmatrix} \theta_{ix} \\ \theta_{iy} \end{pmatrix} - \begin{pmatrix} \beta_x(\theta_{ix}, \theta_{iy}) \\ \beta_y(\theta_{ix}, \theta_{iy}) \end{pmatrix}$$

Hence

$$\Delta\theta_{sx} = \Delta\theta_{ix} - \frac{\partial\beta_x}{\partial\theta_{ix}}\Delta\theta_{ix} - \frac{\partial\beta_x}{\partial\theta_{iy}}\Delta\theta_{iy}$$

and

$$\Delta\theta_{sy} = \Delta\theta_{iy} - \frac{\partial\beta_y}{\partial\theta_{ix}}\Delta\theta_{ix} - \frac{\partial\beta_y}{\partial\theta_{iy}}\Delta\theta_{iy}$$

where Δ denotes incremental change.

$$\begin{pmatrix} \Delta\theta_{sx} \\ \Delta\theta_{sy} \end{pmatrix} = \begin{pmatrix} 1 - \frac{\partial\beta_x}{\partial\theta_{ix}} & -\frac{\partial\beta_x}{\partial\theta_{iy}} \\ -\frac{\partial\beta_y}{\partial\theta_{ix}} & 1 - \frac{\partial\beta_y}{\partial\theta_{iy}} \end{pmatrix} \begin{pmatrix} \Delta\theta_{ix} \\ \Delta\theta_{iy} \end{pmatrix}$$

This expresses small changes in source in terms of small changes in image. However, we shall require to invert the equations in order to relate small changes in image in terms of small changes in source.

$$\begin{pmatrix} \Delta\theta_{ix} \\ \Delta\theta_{iy} \end{pmatrix} = \frac{1}{\det} \begin{pmatrix} 1 - \frac{\partial\beta_y}{\partial\theta_{iy}} & \frac{\partial\beta_x}{\partial\theta_{iy}} \\ \frac{\partial\beta_y}{\partial\theta_{ix}} & 1 - \frac{\partial\beta_x}{\partial\theta_{ix}} \end{pmatrix} \begin{pmatrix} \Delta\theta_{sx} \\ \Delta\theta_{sy} \end{pmatrix}$$

where

$$\det = \left(1 - \frac{\partial\beta_x}{\partial\theta_{ix}}\right)\left(1 - \frac{\partial\beta_y}{\partial\theta_{iy}}\right) - \frac{\partial\beta_x}{\partial\theta_{iy}}\frac{\partial\beta_y}{\partial\theta_{ix}}$$

$$\Rightarrow \det = 1 - \frac{\partial\beta_x}{\partial\theta_{ix}} - \frac{\partial\beta_y}{\partial\theta_{iy}} + \text{h.o.t.}$$

$$\Rightarrow \frac{1}{\det} = 1 + \frac{\partial\beta_x}{\partial\theta_{ix}} + \frac{\partial\beta_y}{\partial\theta_{iy}} + \text{h.o.t.}$$

$$\begin{pmatrix} \Delta\theta_{ix} \\ \Delta\theta_{iy} \end{pmatrix} = \begin{pmatrix} 1 + \frac{\partial\beta_x}{\partial\theta_{ix}} & \frac{\partial\beta_x}{\partial\theta_{iy}} \\ \frac{\partial\beta_y}{\partial\theta_{ix}} & 1 + \frac{\partial\beta_y}{\partial\theta_{iy}} \end{pmatrix} \begin{pmatrix} \Delta\theta_{sx} \\ \Delta\theta_{sy} \end{pmatrix}$$

So if we make the added assumption that all the source galaxies are circles i.e. with intensity weighted second moments as defined in equation (2.11),

$$\begin{pmatrix} I_{xx} & I_{xy} \\ I_{yx} & I_{yy} \end{pmatrix} = \text{const} \times \begin{pmatrix} 1 & 0 \\ 0 & 1 \end{pmatrix}$$

then their imaged intensity weighted moments will be,

$$\begin{pmatrix} I_{xx} & I_{xy} \\ I_{yx} & I_{yy} \end{pmatrix} = \text{const} \times \begin{pmatrix} 1 + \frac{\partial \beta_x}{\partial \theta_{ix}} & \frac{\partial \beta_x}{\partial \theta_{iy}} \\ \frac{\partial \beta_y}{\partial \theta_{ix}} & 1 + \frac{\partial \beta_y}{\partial \theta_{iy}} \end{pmatrix} \begin{pmatrix} 1 & 0 \\ 0 & 1 \end{pmatrix} \begin{pmatrix} 1 + \frac{\partial \beta_x}{\partial \theta_{ix}} & \frac{\partial \beta_x}{\partial \theta_{iy}} \\ \frac{\partial \beta_y}{\partial \theta_{ix}} & 1 + \frac{\partial \beta_y}{\partial \theta_{iy}} \end{pmatrix}$$

$$\begin{pmatrix} I_{xx} & I_{xy} \\ I_{yx} & I_{yy} \end{pmatrix} \propto \begin{pmatrix} 1 + 2\frac{\partial \beta_x}{\partial \theta_{ix}} & 2\frac{\partial \beta_x}{\partial \theta_{iy}} \\ 2\frac{\partial \beta_y}{\partial \theta_{ix}} & 1 + 2\frac{\partial \beta_y}{\partial \theta_{iy}} \end{pmatrix}$$

124

Appendix B -

Shearing The CCD Frame

As described in Section (2.5.2), in some of our simulations we shear our CCD frames by a small amount, ϵ, in the x-direction. In this section we derive the intensity-weighted second moments of galaxies after they have undergone this shearing, and hence calculate the expected mean values of the quantities e_1 and e_2 defined in Section (2.2.2)

Let us assume that the pre-shear x-coordinate, X, becomes x, after shearing.

$$x = (1 + \epsilon)X$$
$$\Rightarrow dx = (1 + \epsilon)\,dX$$

The new value of I'_{xx} is given by,

$$
\begin{aligned}
I'_{xx} &= \int I x^2 \, dx \, dy \\
&= \int I(1 + \epsilon)^2 X^2 (1 + \epsilon) \, dX \, dY \\
&= (1 + \epsilon)^3 I_{xx}
\end{aligned}
$$

Since there is no shear in the y-direction, y=Y, and

$$
\begin{aligned}
I'_{yy} &= \int I y^2 \, dx \, dy \\
&= \int I(1 + \epsilon) y^2 \, dX \, dY \\
&= (1 + \epsilon) I_{yy} \\
I'_{xy} &= \int I x y \, dx \, dy \\
&= \int I(1 + \epsilon)^2 XY \, dX \, dY \\
&= (1 + \epsilon)^2 I_{xy}
\end{aligned}
$$

Then

$$
\begin{aligned}
e_1 &= \frac{I_{xx} - I_{yy}}{I_{xx} + I_{yy}} \\
e'_1 &= \frac{(1 + \epsilon)^3 I_{xx} - (1 + \epsilon) I_{yy}}{(1 + \epsilon)^3 I_{xx} + (1 + \epsilon) I_{yy}}
\end{aligned}
$$

For circular galaxies, $I_{xx} = I_{yy}$, so

$$\begin{aligned}
e_1' &= \frac{(1+\epsilon)^3 - (1+\epsilon)}{(1+\epsilon)^3 + (1+\epsilon)} \\
&= \frac{(1+\epsilon)^2 - 1}{(1+\epsilon)^2 + 1} \\
&= \frac{2\epsilon + \epsilon^2}{2 + 2\epsilon + \epsilon^2} \\
&= \frac{\epsilon}{2}(2+\epsilon)[1 + \epsilon(1 + \frac{\epsilon}{2})]^{-1} \\
&= \frac{\epsilon}{2}(2+\epsilon)[1 - \epsilon(1 + \frac{\epsilon}{2}) + \epsilon^2(1 + \frac{\epsilon}{2})^2 + \text{h.o.t.}] \\
&= \frac{\epsilon}{2}(2+\epsilon)[1 - \epsilon + \frac{\epsilon^2}{2} + \text{h.o.t.}] \\
&= \frac{\epsilon}{2}[2 - \epsilon + \text{h.o.t.}] \\
&= \epsilon - \frac{\epsilon^2}{2} + \text{h.o.t.} \\
&\simeq \epsilon
\end{aligned}$$

If we perform a similar analysis for elliptical galaxies, we obtain

$$e_1' = e_1 + \frac{4\epsilon I_{xx} I_{yy}}{(I_{xx} + I_{yy})^2} + \text{h.o.t.}$$

which reduces to ϵ as before, for the circular case.

Now for e_2,

$$\begin{aligned}
e_2' &= \frac{2I_{xy}'}{I_{xx}' + I_{yy}'} \\
&= \frac{2(1+\epsilon)^2 I_{xy}}{(1+\epsilon)^3 I_{xx} + (1+\epsilon) I_{yy}} \\
&= \frac{2(1+\epsilon) I_{xy}}{(1+\epsilon)^2 I_{xx} + I_{yy}}
\end{aligned}$$

For circular galaxies, $I_{xy} = 0$

$$\Rightarrow e_2' = 0$$

Bibliography

Arnaud M., 1994, in Seitter W. C., ed, Cosmological Aspects of X-ray Clusters of Galaxies. Kluwer Academic Publishers, p. 197

Babul A., Ferguson H. C., 1996, Ap. J., 458, 100

Bartelmann M., 1995, A.&A., 299, 11

Bartelmann M., Narayan R., 1995, Ap.J., 451, 60

Bartelmann M., Weiss A., 1994, A.&A., 287, 1

Bernstein G., Nichol R. C., Tyson J. A., Ulmer M. P., Wittmann D., 1996, A. J., 110, 1507

Bertin E., 1994, IAP Paris

Bertschinger E., 1987, Ap.J., 323, L103

Binggeli B., Sandage A., Tammann G. A., 1985, A.J., 90, 1681

Birkinshaw M., Hughes J. P., Arnaud K. A., 1991, Ap.J., 379, 466

Biviano A., Durret F., Gerbal D., Fevre O. L., Lobo C., Mazure A., Slezak E., 1995, A.&A., 297, 610

Blandford R. D., Kochanek C. S., 1987, in Bahcall J., Piran T., Weinberg S., ed, Proc. 13th Jerusalem Winter School, Dark Matter in the Universe. World Scientific, p. 134

Bonnet H., Mellier Y., Fort B., 1994, Ap.J., 427, L83

Brainerd T. G., Blandford R. D., Smail I., 1996, preprint

Broadhurst T. G., Taylor A. N., Peacock J. A., 1995, Ap.J., 483, 49

Broadhurst T. J., Ellis R. S., Glazebrook K., 1991, Nature, 355, 55

Broadhurst T. J., Ellis R. S., Shanks T., 1988, M.N.R.A.S, 235, 827

Burstein D., Heiles C., 1984, Ap.J.S., 54, 33

Carlberg R. G., Yee H. K. C., Ellingson E., 1994, Ap.J., 437, 63

Cole S., Aragon-Salamanca A., Frenk C. S., Navarro J. F., Zepf S. E., 1994, M.N.R.A.S., 271, 781

Colless M. M., 1987, Ph.D. thesis, University of Cambridge

Davies J. I., Disney M. J., Phillipps S., Boyle B. J., Couch W. J., 1994, M.N.R.A.S., 269, 349

Davis M., Efstathiou G., Frenk C. S., White S. D. M., 1985, Ap.J., 292, 371

Dressler A., 1980, Ap.J., 236, 351

Dressler A., Schectman S., 1988, A.J., 95, 284

Driver S. P., Phillips S., Davies J. I., Morgan I., Disney M. J., 1994, M.N.R.A.S., 268, 393 (DPDMD)

Efstathiou G., Ellis R. S., Peterson B. A., 1988, M.N.R.A.S., 232, 431

Ellis R. S., Allington-Smith J. R., Smail I., 1991, M.N.R.A.S., 249, 184

Evrard A. E., 1988, M.N.R.A.S., 235, 911

Evrard A. E., Mohr J. J., Fabricant D. G., Geller M. J., 1994, Ap.J., 419, L9

Fabian A. C., 1988, in Pallaviani R., ed, Hot Thin Plasmas in Astrophysics. Kluwer Academic Publishers, p. 293

Fahlman G., Kaiser N., Squires G., Woods D., 1994, Ap.J., 437, 56

Forman W. F., Jones C. J., 1990, in Oegerle W. R., Fitchett M. J., Danly L., ed, Clusters of Galaxies. Cambridge University Press, p. 257

Fort B., Mellier Y., 1994, A.&A.R., 5, 239

Frenk C. S., White S. D. M., Efstathiou G., Davis M., 1990, Ap.J., 351, 10

Frenk C. S., White S. D. M., Efstathiou G., Summers F. J., 1996, preprint

Geller M. J., Beers T. C., 1982, P.A.S.P., 94, 421

Gudehus D. H., 1989, Ap.J., 340, 661

Guiderdoni B., Rocca-Volmerange B., 1990, A.&A., 227, 362

Hughes J. P., 1989, Ap.J., 337, 21

Impey C., Bothun G., Malin D., 1988, Ap.J., 330, 634

Jarvis J. F., Tyson J. A., 1981, A.J., 86, 476

Kaiser N., 1995, Ap.J., 439, L1

Kaiser N., Squires G., 1993, Ap.J., 404, 441

Kaiser N., Squires G., Fahlman G., Woods D., 1994a, in Durret F., ed, Proc. Meribel conference, Clusters of Galaxies. Edition Frontiers

Kaiser N., Squires G., Fahlman G., Woods D., Broadhurst T. G., 1994b, in Maddox S. J., Aragon-Salamanca A., ed, Proc. 35th Herstmonceux conference, Wide Field Spectroscopy and The Distant Universe. Kluwer Academic Publishers, p. 246

Kochanek C. S., 1990, M.N.R.A.S., 247, 135

Lacey C., Cole S., 1993, M.N.R.A.S., 262, 627

Landolt A. U., 1992, A.J., 104, L340

Lavery R., Henry J. P., 1988, Ap.J., 329, L21

Loveday J., Peterson B. A., Efstathiou G., Maddox S. J., 1992, Ap.J., 390, 338

Lynds R., Petrosian V., 1986, Bull. Am. Astron. Soc., 18, 1014

Marzke R. O., Huchra J. P., Geller M. J., 1994, Ap.J., 428, 43

McGaugh S. S., 1994, Nature, 367, 538

McGaugh S. S., Schombert J. M., Bothun G. D., 1995, A.J., 109, 1019

Metcalfe N., Shanks T., Fong R., Roche N., 1995, M.N.R.A.S., 273, 257

Miralda-Escude J., 1991, Ap.J., 370, 1

Mohr J. J., Evrard A. E., Fabricant D. G., Geller M. J., 1995, Ap.J., 447, 8

Oegerle W. R., Fitchett M. J., Hill J. M., Hintzen P., 1991, Ap.J., 376, 46

Peebles P. J. E., 1980, The Large-Scale Structure of the Universe. Princeton University Press

Peterson B. A., Ellis R. S., Efstathiou G., Shanks T., Bean A. J., Fong R., Zen-Long Z., 1986, M.N.R.A.S., 221, 233

Phillipps S., Driver S., 1995, M.N.R.A.S., 274, 832

Press W. H., Schechter P. L., 1974, A.J., 187, 425

Richstone D., Loeb A., Turner E. L., 1992, Ap.J., 393, 477

Schechter P. L., 1976, A.J., 203, 297

Schneider P., 1995, A.&A., 302, 639

Schneider P., Ehlers J., Falco E. E., 1992, Gravitational Lenses. Heidelberg:Springer

Seitz C., Schneider P., 1995a, A.&A., 297, 287

Seitz S., Schneider P., 1995b, A.&A., 305, 383

Smail I., 1993, Ph.D. thesis, University of Durham

Smail I., Ellis R. S., Fitchett M., Edge A., 1994, M.N.R.A.S., 273, 277

Smail I., Hogg D. W., Yan L., Cohen J. G., 1995, Ap.J., 449, L105

Soltan A., Henry J. P., 1983, Ap.J., 271, 442

Soucail G., Fort B., Mellier Y., Picat J. P., 1987, A.&A., 172, L14

Squires G., 1994, private communication

Squires G., Kaiser N., Babul A., Fahlman G., Woods D., Neumann D. M., Bohringer H., 1996, preprint

Thompson L. A., Gregory S. A., 1993, A.J., 106, 2197

Tyson J. A., 1988, A.J., 96, 1

Tyson J. A., 1996, in Schaeffer R., Silk J., Spiro M., Zinn-Justin J., ed, Proc. Les Houches Summer School, Cosmology and Large Scale Structure. Elsevier Scientific Publishers

Tyson J. A., Fischer P., 1995, Ap.J., 446, L55

Tyson J. A., Valdes F., Wenk R., 1990, Ap.J., 349, L1

Valdes F., Tyson J. A., Jarvis J. F., 1983, Ap.J., 271, 431

West M. J., Bothun G. D., 1990, Ap.J., 350, 36

West M. J., Jones C., Forman W., 1995, Ap.J., 451, L5

Wilson G., Smail I., Frenk C. S., Ellis R. S., Couch W. J., 1996, M.N.R.A.S., in preparation